Characterizing the Impact of Specific Genetic Mutations on Chemotherapy Resistance and the Efficacy of Oncolytic Viruses for the Treatment of Ovarian Cancer

Submitted by Alison Cudmore

A thesis submitted to the in partial fulfillment of the requirements for the degree of

Master of Science, Specialization in Microbiology & Immunology

Department of Biochemistry, Microbiology & Immunology

Faculty of Medicine

University of Ottawa

Supervised by Dr. Barbara Vanderhyden & Dr. Jean-Simon Diallo

Abstract

Epithelial ovarian cancer (EOC) is the most lethal gynecologic cancer and urgently requires new therapies. Oncolytic viruses (OV) are a strong contender. OVs interact with immune components of the TME, which can be altered due to specific genetic mutations. The present study evaluates the impact of specific tumour mutations on the response to carboplatin, the current standard of care, and VSVΔM51, a promising OV candidate. After a study of genetically diverse models, constitutive *KRas* activation enhanced VSVΔM51 replication *in-vitro* and sensitivity in syngeneic *in-vivo* models. VSVΔM51 prolonged survival in syngeneic tumour-bearing mice with *KRas, Trp53* and *Pten* mutations, including one tumour model that did not respond to carboplatin. Response to VSVΔM51 *in-vivo* was associated with activation of CD4+ and CD8+ T lymphocytes in the peritoneal TME. In summary, VSVΔM51-based immunotherapy has shown promise in diverse murine models of EOC bearing clinically relevant mutations.

Acknowledgements

There are many individuals without whom this project would not have been possible. I would first like to thank my primary supervisor, Dr. Barbara Vanderhyden, for her critical guidance and mentorship. Her constant support has pushed my development as a researcher since I joined her lab in 2018, and she has continued to foster my success as I took on the challenges of graduate studies in her lab. I am also very thankful for the guidance and expertise of my co-supervisor, Dr. Jean-Simon Diallo. His mentorship in navigating the complex nature of oncolytic virus work has been a key support for completing this research project.

The guidance of my two TAC members, Dr. Michele Ardolino and Dr. Carolina Ilkow, have provided important scientific perspectives and direction. The completion of this project was also greatly supported by Dr. Galaxia Rodriguez, whose shared expertise is evident in many of the experiments completed.

It has been a joy to work on this project as a member of two collaborative and resourceful labs; these groups have been actively engaged in this project over the course of many bench-side scientific debates, lab meetings and "all-hands-on-deck" experiment days. In particular, the mouse experiments completed within this project have been a significant team effort achieved by the collaboration of Elizabeth Macdonald, Humaira Murshed, and Galaxia Rodriguez.

Finally, I would like to acknowledge the work of all staff at the Animal Care and Veterinary Services facilities at the University of Ottawa, who oversaw the wellbeing of all mice used for this project, and the Flow Cytometry Core at the University of Ottawa.

It takes a village to support a graduate student, and I am eternally grateful for mine.

Table of Contents

Abbreviation List

APC..... Antigen-presenting cells
AVCS.... Animal care and veterinary services
BRCA..... Breast cancer gene
CA125..... Cancer antigen 125
CM..... Complete media
DAMP.Damage associated molecular pattern
DMEM-Ø..... Serum-free DMEM media
dsDNA..... Double-stranded DNA
EOC..... Epithelial ovarian cancer
FBS..... Fetal Bovine Serum
FLuc..... Firefly luciferase
FTE..... Fallopian tube epithelium
GFP.....Green fluorescent protein
HGSC..... High-grade serous carcinoma
HSV-1..... Herpes simplex virus type-1
ICD.....Immunogenic cell death
IFN..... Interferon
IL.....Interleukin
IP.....Intraperitoneal
KRas.....Kirsten rat sarcoma oncogene
M51... Matrix protein methionine position 51
MHC.....Major histocompatibility complex
mLN.....Mesenteric lymph node
MOE.....Murine oviductal epithelium
MOI.....Multiplicity of infection
NF1..... Neurofibromatosis factor 1
NK..... Natural killer cell
OC..... Ovarian cancer
OSE.....Ovarian surface epithelium
OV.....Oncolytic virus
PAMPPathogen associated molecular pattern
PARP.....Poly-ADP ribose polymerase
PARPi.....PARP inhibitor
PBS..... Phosphate buffered saline
PD-1..... Programmed death receptor 1
PD-L1..... Programmed death ligand 1
PFU.....Particle forming units
PTEN..... Phosphatase and tensin homolog
qPCRQuantitative polymerase chain reaction
STIC..Serous tubal intraepithelial carcinoma
TAA.....Tumour-associated antigens
TAM..... Tumour-associated macrophage
TIL.....Tumour infiltrating lymphocyte
TK.....Thymidine kinase
TME..... Tumour microenvironment
TP53/Trp53.....Tumour repressor protein 53
Treg.....Regulatory CD4+ T lymphocyte
VGF.....Vaccinia growth factor
VSV.....Vesicular stomatitis virus
VV..... Vaccinia virus
VVDD...Vaccinia virus double-deleted strain
WT.....Wild type

List of Figures

List of Tables

Chapter 1: Introduction

1.1 Ovarian Cancer at Present

1.1.1 The Ovary

The ovaries are the female gonads required for reproduction. Two ovaries sit in the lower abdominal cavity on opposite sides of the uterus, to which they are connected by the fallopian tubes. The primary responsibility for the ovaries is the development of mature oocytes, which may be released into the fallopian tubes via ovulation once per menstrual cycle[1]. During this process, known as oogenesis, the ovaries produce varying amounts of estrogen and progesterone to coordinate the menstrual cycle[1]. The structure of the ovary and the stages of the follicle life cycle are shown in **Figure 1**.

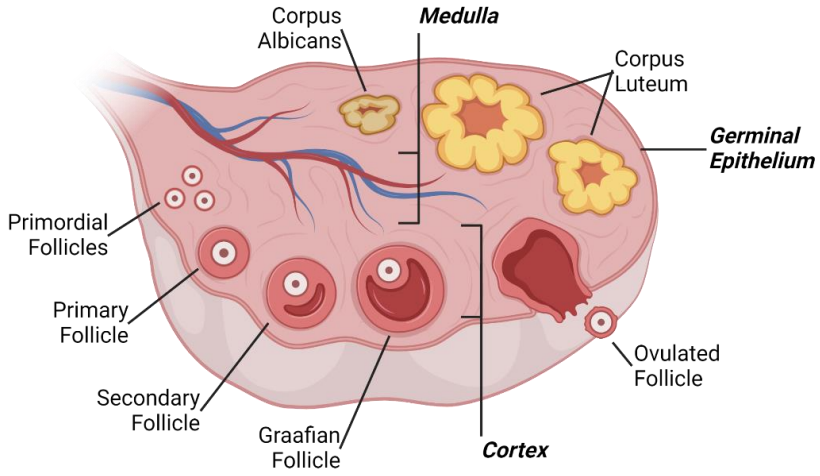

Figure 1: The ovarian structure and follicle life cycle. *The germinal epithelium (also known as the ovarian surface epithelium), medulla, and cortex are the three primary layers of the ovary (bold and italicized). Oogenesis resumes in the primordial follicles upon stimulation and continues beyond ovulation. Created in BioRender.*

The ovary structure can be divided into three distinct layers (**Figure 1**). The ovarian surface epithelium (OSE), also called the germinal epithelium, is the outermost layer of cells encasing the human ovary[1,2]. It is ruptured during ovulation to release an oocyte and must be

continually repaired as a result of this recurring damage. The cortical layer accounts for most of the internal ovary and primarily consists of connective tissue[1,2]. All follicles are housed and develop within the cortex. The innermost layer of the ovary is the medulla, which is highly vascularized to support ovarian functions[1,2].

1.1.2 OC Subtype Classification and Staging

Ovarian cancer (OC) is the group of malignancies that form primary tumours within the ovarian tissue. OC is the most lethal gynecologic malignancy and is diagnosed in 3000 Canadian women each year[3,4]. Upon diagnosis, patients face a dismal 45% five-year survival rate[4]. OC makes up 2.7% of all new cancer cases in Canadian women yearly, yet it is disproportionately responsible for 4.9% of all female deaths by cancer per year[4].

Multiple cellular origins of OC give rise to unique subtypes of disease (**Figure 2**): epithelial (90%), germ cell (5%) and sex-chord-stromal (5%)[5]. Epithelial OC (EOC) contains many subtypes, which are primarily defined by tumour histopathology. High-grade serous carcinomas (HGSC) are the most abundant subtype of EOC, making up 80% of all advanced-stage EOCs and 50% of all OC-related deaths[6,7]. Therefore, HGSC has become the dominant and most relevant target for developing novel cancer therapies.

All EOCs can be divided into Type I and Type II tumours for a more simplistic classification. Type I EOCs are slow-growing, indolent neoplasms with well-defined malignancy origins[5,6,8]. This group includes endometrioid, clear cell, mucinous, and low-grade serous carcinomas. In contrast, Type II EOCs are fast-growing tumours with high genetic instability and universal *TP53* mutation; these malignancies are the most lethal[5,6,8]. HGSC is the primary subtype of Type II EOC[6,8].

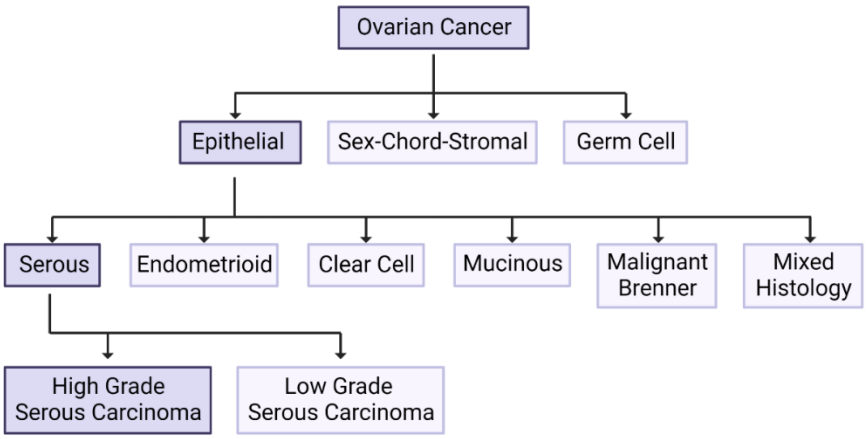

Figure 2: Classification of ovarian cancer subtypes. *The most common origin of OC is epithelial. High-Grade Serous Carcinoma is the most common and lethal epithelial OC subtype. Created in BioRender.*

The staging of EOC tumours from stage I to IV provides a classification of tumour dissemination, based on which prognosis and treatment plans can be determined. In general, the staging of all cancers is established using three factors: tumour size, spread to nearby lymph nodes, and the presence of distant metastasis. In the first stage of EOC, the tumour is contained within one (stage Ia) or both (Ib) ovaries[9]. As the tumour progresses, it begins to invade the uterus (IIa) and adjacent pelvic region (IIb). Slightly more distant sites may eventually be reached, such as the retroperitoneal lymph nodes or intestines (III)[9]. Finally, during the most advanced stage (IV), the tumour has metastasized to regions far beyond the ovary and commonly resides in organs such as the omentum, liver, lungs, or lymph nodes outside the abdomen[9]. A patient with advanced stage EOC will typically also present with fluid build-up in the abdomen, called ascites, which helps to carry these metastases throughout the peritoneal cavity[10]. Wide-spread metastasis around the body is a significant indicator of poor patient prognosis.

1.1.3 Cellular Origins & Pathogenesis of HGSC

It was once thought that HGSC arose solely from the OSE. The incessant ovulation model supports the mechanism whereby genetic alterations within the OSE drive local

tumorigenesis (**Figure 3**)[8]. Repeated ovulations and the resulting wound repair are understood to increase the risk of genetic mutations that cause this malignant transformation[8,11]. The primary evidence for this theory is the discovery that long-term prevention of ovulation due to oral contraception use or multiple pregnancies significantly lowers a woman's lifetime risk of developing OC[12]. Additionally, literature on *in-vitro* models of HGSC has shown that cultures of OSE cells can spontaneously transform into HGSC-like tumour cells[13,14].

Advancements in research have revealed another source of HGSC pathogenesis, whereby the malignant transformation occurs in the fallopian tube (**Figure 3**). In this case, serous tubal intraepithelial carcinoma (STIC) lesions begin development in the fallopian tube epithelium (FTE), migrate to the ovary, and implant on its surface[15,16]. The resulting HGSC tumours flourish within the ovarian microenvironment. Several *in-vitro* and *in-vivo* murine studies have now shown the ability of the oviductal epithelium (the murine equivalent of the FTE) to give rise to HGSC-like tumours; research is also beginning to identify genetic factors driving tumour transformation in the FTE[17–21]. In addition, removal of the fallopian tube via salpingectomy significantly reduces HGSC development, especially in high-risk breast cancer gene (BRCA) 1 and 2 mutation carriers[12,22]. The FTE has become widely accepted as the primary origin of HGSC, though both theories still prevail.

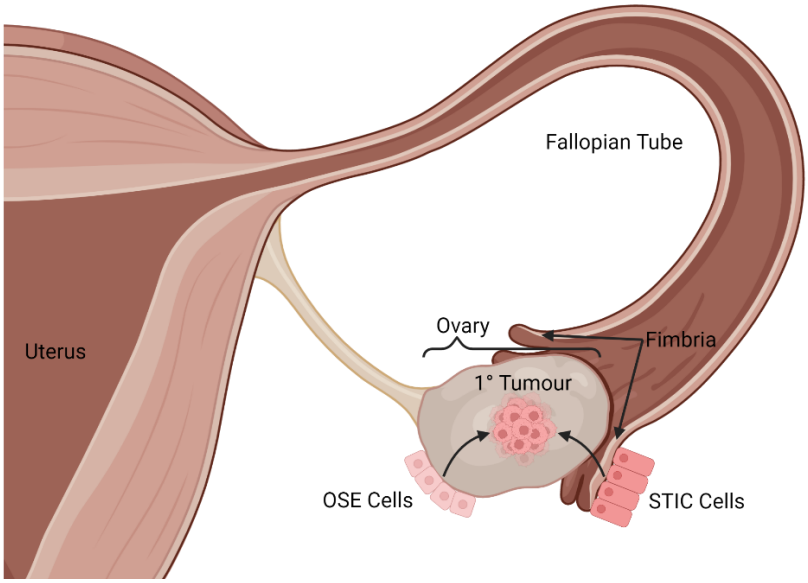

Figure 3: Cellular origins of EOC. *Primary EOC tumours are thought to arise primarily from serous tubal intraepithelial carcinoma (STIC) lesions in the fallopian tube epithelium (FTE) located in the fimbria. These cells transform into pre-cancerous lesions, then migrate and implant into the ovary. Alternatively, the ovarian surface epithelium (OSE) can undergo transformation and directly form EOC tumours.*

1.1.4 Risk Factors and Prevention

Various risk factors govern a woman's likelihood of developing EOC in her lifetime. Mutation in the *BRCA1* and *BRCA2* genes is a strong predictor of EOC development. Both genes are responsible for the repair of homologous double-stranded DNA (dsDNA) breaks. Loss of *BRCA1* or *BRCA2* severely compromises the ability of cells to maintain a stable genome during DNA replication, thus rendering cells vulnerable to tumorigenic mutations[23,24]. Women with *BRCA1/2* mutations have a high lifetime risk of developing EOC and breast cancer, accounting for 10% of all HGSC cases[11,23–25]. Autosomal dominant inheritance of *BRCA1* and *BRCA2* mutations accounts for 90% of hereditary HGSC cases and is the source of familial Hereditary Breast and Ovarian Cancer Syndrome[25]. The genetic risk of EOC is also associated with certain ethnicities[5,26]. For example, Jewish women, especially those of Ashkenazi ancestry, have a high probability of carrying *BRCA1* or *BRCA2* mutations[26].

The age-related risk of OC spikes dramatically after a woman reaches 50 years of age[5]. Higher EOC risk is associated with an increased number of lifetime ovulations, which accumulates with age; a lack of oral contraception use, early age of menarche or late age of menopause can all contribute to this increased risk[5,8,12]. Specific reproductive conditions can also increase EOC risk. For instance, endometriosis affects 10-15% of all reproductive-aged women and can give rise to endometrioid carcinomas[5,27].

A few modifiable lifestyle factors also influence the lifetime risk of EOC development. Most notably, hormone replacement therapy can have various impacts on EOC risk. While estrogen and androgens may increase risk by promoting OSE proliferation, progesterone has been shown to be protective against tumorigenesis by inhibiting cell growth[5,11]. Diet, obesity, and smoking also play minor roles in EOC risk[5,11].

Several options exist to help control OC risk and provide different avenues for prophylactic protection. Oral contraception reduces OC risk by 50% with long-term use by blocking recurrent ovulation and is widely available to Canadian women[12,28,29]. The most effective method for OC prevention is bilateral salpingo-oophorectomy, which can reduce OC risk by 80% [12]. However, due to the early onset of menopause and loss of fertility resulting from ovary removal, this method is typically reserved for the highest-risk women carrying *BRCA1* or *BRCA2* mutations [12]. Preservation of the ovaries is recommended for the average risk woman, in which population salpingectomy alone is highly effective at reducing OC incidence[22,30].

1.1.5 Diagnosis

OC can be diagnosed at any life stage, though it is rare in patients below 30 years of age[5]. The typical OC patient at the time of diagnosis is a post-menopausal female aged 55-65[4,5]. Incidence rates of OC in Canada have declined over the past decade by approximately 3.7% each

year, with similar trends noted in other developed countries[4,29]. This positive trend may be attributed to various factors, including increased hormonal contraception use and more frequent uptake of preventative interventions such as salpingectomy[5,12].

Late-stage diagnosis of OC is very common, resulting from inadequate screening methods and non-specific symptoms of the disease. Symptoms such as bloating, abdominal/lower back pain, and low energy are everyday experiences among healthy, reproductive-aged women and OC patients alike[5,31]. Incidence rates of these symptoms are elevated in OC patients, but still affect a notable proportion of both populations to be perceived as non-concerning regardless of malignancy status[31].

Two methods have been historically used for OC screening with little success: measurement of serum cancer antigen 125 (CA125) and transvaginal ultrasound. The primary failure of both methods for detecting type II EOCs is the inability to identify STICS, the most common precursor lesion for cancer development[5,7,15]. CA125 levels are non-specific to OC patients and inconsistently elevated among true patient populations[5]. Transvaginal ultrasound may only identify changes in ovarian size and morphology resulting from already advanced-stage tumours[32]. Neither screening method has been shown to reduce mortality and achieve success as a screening tool[5,32].

When medical practitioners are at last able to identify EOC in a suspected patient, the confirmed diagnosis will occur with a core-needle biopsy used to sample tissue for classification of stage and subtype[5]. The typical delay in diagnosis by this time means that the window of opportunity for early intervention, when the tumour is most responsive to therapy, has already been lost. Ongoing research has aimed to identify new screening measures to detect early-stage

tumours without solid results. What remains are the OC patients and their medical teams who are combatting complex, advanced diseases.

1.1.6 Current Standards of Care

Surgical tumour debulking has been a mainstay of OC therapy, regardless of the recommended treatment combinations that have shifted with medical advancement. The primary functions of surgical debulking are to remove as much tumour mass as possible, collect tissue for biopsy and definitively stage the malignancy[5,33]. Tumour resection is most effective when any residual tumours are below $1cm^3$ in size[33,34]. Despite the necessity of tumour debulking surgery, this treatment requires an effective adjuvant therapy to prolong progression-free survival and reduce disease mortality.

Chemotherapy has historically been the adjuvant drug used for the treatment of HGSC and is usually a combination of a taxane and a platinum drug. It is a systemic treatment usually given by intravenous delivery. Taxane- or platinum-based chemotherapy drugs are cytotoxic DNA damaging agents that target rapidly and uncontrollably proliferating cells, such as cancer cells. Patients with chemotherapy-naive tumours face the best chance for tumour regression with these drugs[35,36]. However, the recurrence of chemotherapy-resistant tumours is common and severely reduces patient prognosis[35]. Resistance to chemotherapy may occur through various cellular mechanisms, including drug efflux, loss of drug target and loss of membrane transport[35,37]. As a result, most HGSC patients are repeatedly left to battle recurrent tumours with ineffective chemotherapy regimes, with a worse prognosis each time the tumour returns.

Neoadjuvant chemotherapy was introduced in the 2000s to achieve two main functions: 1) increase the chance of a successful surgical intervention by proactively reducing tumour size, and 2) assess tumour responsiveness to drug intervention at an early treatment stage[33,36].

Evidence suggests a small benefit of this combined regime in stage IV advanced EOCs[34]. Across all cases of EOC, neoadjuvant chemotherapy has not been shown to improve survival outcomes in patients compared to primary surgical debulking alone[36].

The mechanism of chemotherapy action leads to wide-spread and adverse side effects on the patient, limiting their ability to undergo successive rounds of treatment. Side-effects of chemotherapy may include loss of hair, nausea and vomiting, and development of skin rashes/sores[38]. Poor hematopoiesis in the bone marrow can lead to easy fatigue, leukopenia, and thrombocytopenia: three conditions with their own adverse effects[38].

The development of Poly-ADP Ribose Polymerase (PARP) inhibitors (PARPi) as an adjuvant EOC therapy in the early 2010s provided what seemed to be a breakthrough in cancer therapeutics. PARPs are responsible for single-stranded DNA repair, and if inhibited, their responsibilities can be taken care of by homologous DNA repair pathways such as those controlled by BRCA1/2[39,40]. PARPi's are most effective in tumours carrying loss-of-function *BRCA1/2* mutations, as the tumour cells cannot compensate for PARPi-induced DNA damage[39]. PARPi's can work well in combination therapy regimes by reducing the ability of tumours to repair chemotherapy-induced DNA damage[5,39]. However, tumour cells can become resistant to PARPi's through the same mechanisms that cause chemotherapy resistance[40].

Despite the severity of EOC disease, "old-school" regimes combining chemotherapy and surgical debulking are still relied upon today and have not been dramatically improved in a generation. These current therapies have failed to treat HGSC long-term, creating an urgent need for novel therapies. Such treatments must overcome drug resistance and be effective against diverse HGSC tumours.

1.2 Tumour Factors Shaping HGSC Progression

1.2.1 The Inflammatory Tumour Microenvironment

The tumour microenvironment (TME) can be defined as the entire habitat within which a tumour exists. The TME is a complex, interwoven network of many components, including healthy resident tissue cells, tumour cells, immune cells, stromal cells, blood vessels, cytokines, and extracellular matrices. Effective tumour regression relies on strong innate and adaptive immune responses within the TME. An anti-tumour inflammatory TME is a strong and positive predictor of patient prognosis [41,42].

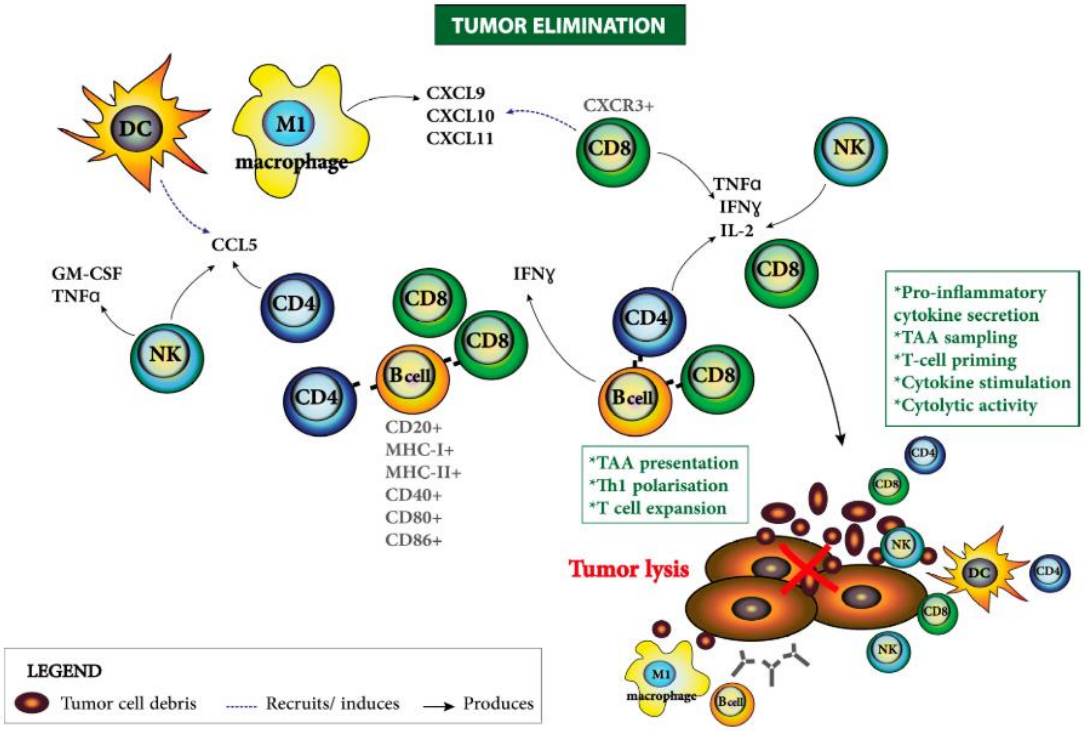

Figure 4: Antitumoral immune response in the tumour microenvironment of EOC. *Immunogenic cell death is induced by circulating innate immune cells, allowing for antigen sampling and activation of adaptive immune responses. Further tumour destruction is achieved through both arms of the immune system. Presented by Rodriguez, et al (2018)*[41].

In the absence of immune suppression, many key immune players circulate the TME to combat tumour growth (summarized above **Figure 4** by Rodriguez et al[41]). Adaptive CD8+ T

lymphocytes recognize tumour-associated antigens (TAA) presented on the cell surface by major histocompatibility (MHC) class I complexes[41,42]. The result is the release of cytotoxic granules or pro-inflammatory cytokines and the induction of tumour apoptosis via Fas/FasL interaction [41,43,44]. TAAs distinguish a tumour from healthy tissue in the eyes of the immune system and include neoantigens unique to the mutated tumour cell[45]. When tumour cells are lysed, the release of immunogenic damage-associated molecular patterns (DAMPs) recruits and activates more immune cells within the TME. Natural killer (NK) cells are innate, cytotoxic immune cells controlled by the balance of inhibitory and stimulatory signals; the NK cells fight alongside CD8+ T cells using similar mechanisms to destroy cancer cells[42,46]. The increased presence of CD8+ T and NK cells is associated with improved EOC patient prognosis[41,42]. CD4+ T-helper cells critically support the activation of nearly all immune cells.

Antigen-presenting cells (APCs) – including dendritic cells (DC), macrophages, and B lymphocytes – enhance the activation of T and NK cells by presenting tumour antigens on MHC-II complexes[41,42,46]. Co-stimulatory ligands, such as CD80/86, assist with MHC-II antigen presentation to activate lymphocytes. Tumour-associated macrophages (TAMs) exhibit high plasticity and can change functionality based on signals within the TME. M1 polarized TAMs are a good prognostic indicator when present within the TME and function to amplify anti-tumour responses[41,42,47]. However, the presence is typically reduced in advanced stage EOC in favour of immune-inhibiting M2 polarized TAMs[42].

DCs are crucial APCs forming the interface between the adaptive and innate immune responses. Plasmacytoid DCs produce mass amounts of type I interferons (IFN) upon TAA recognition and are associated with beneficial outcomes in primary and metastatic EOC [42]. Conventional DCs (cDC) are highly efficient at sampling and presenting TAAs on MHC-II to

activate CD8+ T cells[41,42,46]. CDC-1 cells primarily assist in activating CD8+ T cytotoxic cells, whereas cDC-2 cells are more adept at activating CD4+ T helper cells[48,49]. Finally, B lymphocytes can be found in stromal or intraepithelial locations within the TME[41]. Their presence can enhance survival benefits conferred by CD8+ T cells, with which B lymphocytes often co-localize [41].

1.2.2 The Immunosuppressed Tumour Microenvironment

The TME of EOC is often highly immunosuppressed. This state is associated with poor survival outcomes and an inadequate response to treatment, presenting an additional challenge for novel therapies to overcome[41,42]. In many cases of EOC, the selective pressure applied by the robust anti-tumour immune responses described above drives the development of non-immunogenic tumours. The resulting tumours evade identification by the immune system and actively enhance immune suppression through multiple, diverse mechanisms, which are described below. Effective treatment of EOC must overcome these challenges to improve patient survival outcomes and prevent recurrent disease.

The primary mechanism by which EOC tumours remain hidden from detection by the immune system is a loss of TAA presentation on MHC-I; however, recent studies have provided hope that this mechanism could be restored to ignite anti-tumour immune response [41,43,44,50]. Though invisible to the immune system, these tumours remain highly active in the TME by secreting immune inhibitory cytokines. This process of immunoediting is associated with poor patient prognosis and treatment efficacy.

Immunoediting is modulated mainly through the secretion of pro-tumour cytokines, including indoleamine-2,3-dioxygenase, transforming growth factor β, interleukin-10 or vascular endothelial growth factor[41]. These secreted factors assist in creating a favourable environment

for tumour growth by polarizing and recruiting suppressive immune cell populations. Regulatory CD4+ T lymphocytes (Tregs) function to lyse anti-tumour immune cells, inhibit antigen presentation, and secrete pro-tumour cytokines[42,46]. A high ratio of Tregs vs. CD8+ T cells is known to be associated with poor patient prognosis[41,42]. M2 polarized TAMs promote neo-angiogenesis to sustain the growing tumour, foster the development of tumour metastasis, and assist in rewiring the TME by secreting interleukin (IL) 10 and TGF-β[41,46,47]. The ratio of M2 vs. M1 polarized TAMs is often a critical prognostic indicator within the TME[42,47]. Myeloid-derived suppressor cells (MDSCs) assist in the loss of tumour immunogenicity by secreting reactive oxygen and nitrogen species into the TME. They also support the functions of other inhibitory immune cells while attenuating the actions of inflammatory immune cells[41]. The prognosis of both primary and metastatic EOC is reduced by the presence of MDSCs[42].

Many of the aforementioned inhibitory immune cells utilize immune checkpoints and co-inhibitory ligands to inactivate anti-tumour immune responses. For example, the interaction between programmed death receptor 1 (PD-1) and its partner programmed death ligand 1 (PD-L1) is one immune checkpoint that can be leveraged by cancer cells to enhance immune suppression. During antigen presentation, PD-L1 on the tumour cell surface will disable a surveying CD8+ T cell via interaction with PD-1 on the immune cell surface[51,52]. Thus, the tumour cells have adapted to escape immunogenic cell death at the hands of the CD8+ T lymphocyte. PD-L1 expression is typically consistent between primary tumours and the peritoneal metastases they give rise to[51]. High tumour PD-L1 expression is associated with lymph node metastasis but not reduced survival outcomes in HGSC patients[51].

In addition to the immunosuppressive mechanisms described above, tumour cells can also limit access of anti-tumour immune cells to the tumour site. Recent research has carefully

analyzed three broad categories of immune exclusion and their associated molecular phenotypes[53,54]. The "immune infiltrated" TME is characterized by thorough CD8+ T cell infiltration and TAA presentation by MHC-I[53,54]. As such, patients with immune infiltrated tumours face the best prognosis. In contrast, "immune excluded" tumours restrict CD8+ T cells to the stromal tissue; this limits the ability of the immune system to access, identify and target tumour cells [53,54]. Finally, in "immune desert" phenotypes, there is little to no immune activity in the TME [53,54]. Tumours express low levels of MHC-I and are predisposed to metastasize by undergoing the epithelial-mesenchymal transition, which contributes to a poor patient prognosis[54].

1.2.3 Specific Genetic Mutations in HGSC

The impact of specific tumour mutations on their molecular signalling pathways and tumour proliferation has been well established. Ongoing research is now providing a new perspective examining the impact of these genetic mutations on the immune composition in the TME in pre-clinical murine models and human HGSC tumours[55,56]. This section will discuss the role of specific genetic mutations in altering tumour progression via the hijacking of molecular signalling pathways and influencing the TME.

Mutation in Tumour Repressor Protein 53 (*TP53* in humans or *Trp53* in mice) is a hallmark of HGSC occurring in >95% of cases[57]. Wild-type (WT) TP53 is a tumour suppressor involved in exerting cell cycle control, DNA repair and apoptosis. Without proper regulation by TP53, the cell cycle becomes dysregulated and can promote cancer development. Loss of function mutations therefore release the tumour-suppressive effects directed by WT TP53. On the other hand, "gain of function" mutations (such as R273H) result in oncomorphic changes to the WT TP53 protein, which switches the overall protein function to promote tumorigenesis and

proliferation[58]. Both inactivation and overexpression of TP53 increase the risk of metastasis, chemotherapy resistance and early recurrence[18,59,60]. Immunohistochemistry performed on human OC samples revealed that *TP53* mutations are associated with an increased presence of tumour infiltrating lymphocytes (TILs); however, the ratio of CD8+/Treg cells was a better predictor of patient survival than was the level of TILs in the TME[61]. A pre-clinical murine model has also revealed preferential T cell infiltration associated with a mutation in *Trp53*[56].

Mutations in the breast cancer genes (*BRCA*) 1 and 2 are responsible for 90% of hereditary and 10% of all EOC cases (see **section 1.1.4** for *BRCA1/2* mutation as a risk factor for EOC) [11,23–25]. These proteins function in the homologous repair of dsDNA breaks[23]. The resulting loss of genetic stability renders cells susceptible to mutation and tumorigenesis. A pre-clinical study showed increased inflammation when *Brca1* deletion was added to tumours generated from transformed murine FTE cells carrying a panel of other pre-existing genetic mutations[55]. Notably, *Brca1* mutation in this model enhanced the presence of TAMs and T lymphocytes. Assessment of human HGSC tumours has also recognized *BRCA1* mutation inducing an immunogenic phenotype[62].

The phosphatase and tensin homolog (PTEN) is a tumour repressor protein rendered dysfunctional in approximately 30% of HGSC cases[63,64]. Functional PTEN reverses the conversion of PIP_2 to PIP_3, thereby disrupting the PI3K growth pathway. As such, an inactivating mutation in PTEN releases the breaks applied to this critical cell proliferation pathway, allowing for tumour growth. Given this mechanism, it is not surprising that loss of *Pten* alone was sufficient to drive tumorigenesis in FTE-derived murine models[17]. Multi-method analysis of HGSC patients and their tumours has shown that PTEN loss is a frequent driver of clinical HGSC and is associated with low TIL counts[65,66].

The Kirsten rat sarcoma oncogene homolog (*KRAS*) plays an important role in tumour progression by transducing extracellular signals to stimulate growth pathways, primarily the RAS-RAF-MEK-ERK and PI3K pathways. *KRAS* mutation is prevalent in approximately 10% of HGSC cases[57]. Sustained activation of KRAS targets multiple downstream effector proteins to enhance cell growth, proliferation, and differentiation. Within the TME, *KRAS* mutation has been associated with strongly immunosuppressive phenotypes and the conversion of CD4+ CD25+ T cells into Tregs[67].

Lastly, a mutation in the neurofibromatosis type 1 (*NF1*) gene is less frequent in HGSC (<5%), though still defined as significant in OC by the Cancer Genome Atlas Research Network[57]. NF1 dephosphorylates RAS, thus inhibiting multiple growth pathways that rely on RAS for stimulation (including the PI3K and MEK pathways)[68]. The downregulation or absence of NF1 leaves cells vulnerable to constitutive growth pathway activation and tumorigenesis. Due to the low frequency of *NF1* mutation in HGSC, little is known so far about the impact of *NF1* mutation alone on the TME immune landscape. However, *NF1* mutation has been included in many pre-clinical HGSC models utilizing large panels of genetic mutations in the study of the TME[55].

1.2.4 Pre-Clinical Models to Study Tumour Factors in HGSC

Murine HGSC-like cell lines and their use in syngeneic models have been instrumental in uncovering tumour factors shaping disease progression. These cell lines can arise from the OSE or oviductal epithelium (murine equivalent of the FTE) and be altered to harbour specific tumour mutations present in HGSC. When used to create syngeneic models, a functional immune system allows for TME analysis. Three murine cell lines are typically used in pre-clinical study of HGSC: the ID8, STOSE and MOE cells.

The ID8 cells are a widely used model of HGSC, first described by Roby et al. over twenty years ago[14]. These cells were spontaneously derived *in-vitro* from OSE cells of C57BL/6 mice. Intraperitoneal (IP) injection of ID8 cells into syngeneic hosts leads to the growth of widespread abdominal tumours and ascites, which is characteristic of late-stage HGSC[14]. Lacking any known clinically relevant mutations, the ID8 cells were modified by Dr. Ian McNeish using the CRISPR-Cas9 system to introduce various combinations of mutations common to HGSC, including $Trp53^{-/-}$, $Brca1^{-/-}$, $Brca2^{-/-}$, $Nf1^{-/-}$ and $Pten^{-/-}$ [69,70]. Similarly, the STOSE cells originated from the OSE of FVB/N mice and were first developed in the Vanderhyden lab[13]. IP injection of STOSE cells into syngeneic hosts creates large tumours that favour localization in the fatty tissue of the omentum, a trait commonly seen in clinical cases of metastasized HGSC[13]. The STOSE cells have yet to be modified to include additional mutations.

In murine models, additional cell lines are needed to represent the alternate origin of HGSC: the oviductal epithelium[15]. To address this gap, the murine oviductal epithelial (MOE) cells were generated by the Vanderhyden lab as the basis for HGSC models derived from the oviduct of the FVB/N mice. Dr. Joanna Burdette modified the MOE cells to include a $Pten^{shRNA}$ knockdown alone or in combination with either the $KRas^{G12V}$ or $Trp53^{R273H}$ gain-of-function mutations[17,19]. The MOE cells and their specific genetic mutations are a valuable complement to the genetically diverse cohort of OSE-derived HGSC cell models.

Tumour placement is an important choice in the development of syngeneic models and is thoroughly summarized by Karakashev and Zhang (2021)[71]. Primary orthotopic tumours are placed directly into the site of origin and are contained by the bursa surrounding the ovary in mice. These models best recapitulate the TME, though require skilled surgical injection and are the most expensive. IP injection is a more accessible implantation method that results in

widespread peritoneal tumours and ascites, similar to clinical metastatic cases. Though no primary tumours are created, IP tumours are a good choice for studying advanced-stage disease, immunological events, and survival benefits conferred by immunotherapy treatments. Lastly, subcutaneous injection results in consistent tumours that are easy to monitor but lack the ability to evaluate the TME.

The Vanderhyden lab has previously characterized the TME of diverse orthotopic models of HGSC and provided a comprehensive review of more pre-clinical HGSC models[56,72]. Other research groups have performed large-scale studies of HGSC syngeneic models with tumour mutations using IP models[19,55,69,70].

1.3 Oncolytic Virus Immunotherapy

1.3.1 Oncolytic Viruses: A Promising Front-Runner in EOC Immune Therapy

Many different immune therapies are under development in response to the ever-growing awareness of the importance of the TME in determining cancer survival. Reversal of immune suppression in the TME is a promising strategy for treating EOC[41,73]. Currently, various immune therapies are being evaluated for the treatment of EOC, of which oncolytic virus (OV) therapy is considered highly promising.

OVs are naturally discovered or genetically engineered viruses that preferentially infect and kill tumour cells, leaving healthy tissue unharmed (mechanisms of specificity discussed with regards to specific OVs in sections **1.3.2**, **1.3.3**, and **1.3.4**). Immunogenic cell death (ICD) caused by OV-induced tumour lysis activates critical innate and adaptive immune responses. The resulting multi-faceted attack against the tumours is essential to reverse immune suppression in the TME of EOC.

A summary of ICD as induced by OV infection is presented in **Figure 5**. TAAs, DAMPs and pathogen-associated molecular patterns (PAMPs) that were previously inaccessible are spilled into the TME for recognition by APCs. PAMPs and DAMPs drive innate production of type I IFNs (α and β) to 1) enhance MHC-I/II antigen presentation by APCs, 2) induce APC maturation, and 3) stimulate the further production of immunogenic cytokines (ex. IL1β, TNF-α, and IL-12) thus recruiting more immune cells to the TME[74–76]. Released TAAs are processed and presented by the APCs, which will then prime T lymphocytes and NK cells to attack all tumour cells they encounter, including those at distant metastatic sites.

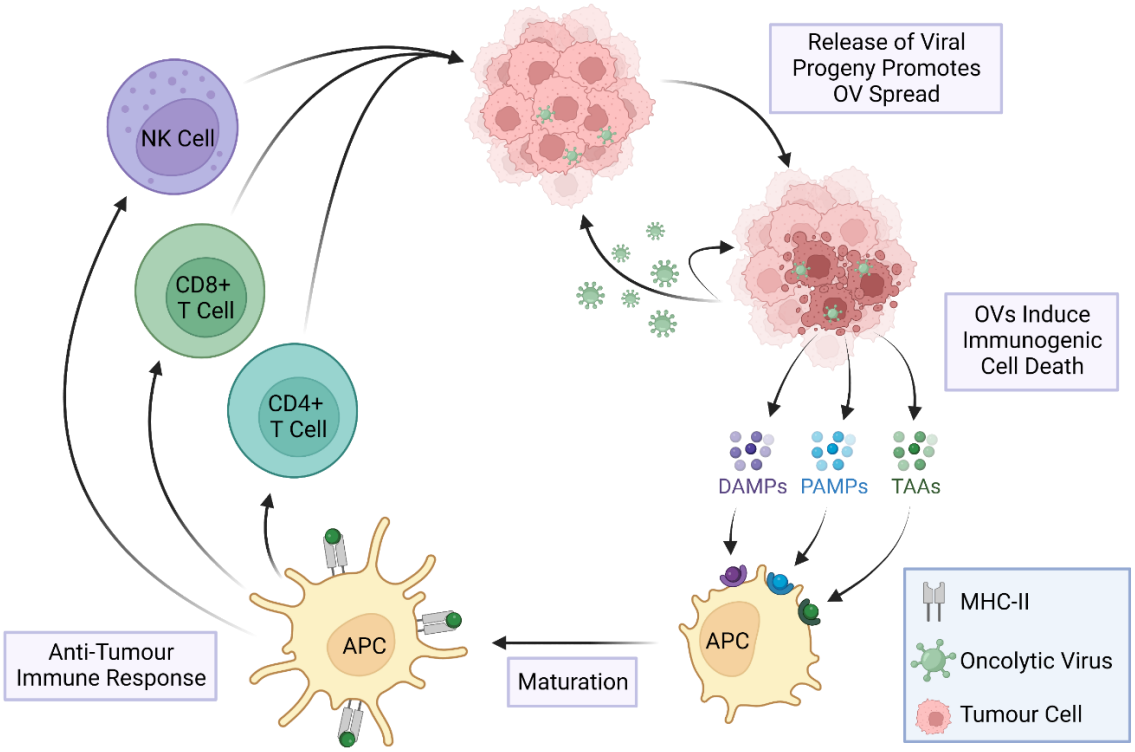

***Figure 5: OV induction of tumour immunogenic cell death in TME**. Immunogenic cell death (ICD) releases tumour-associated antigens (TAAs), damage-associated molecular patterns (DAMPs), and pathogen-associated molecular patterns (PAMPs) in the TME to stimulate antigen-presenting cell (APC) maturation and further immune cell recruitment. Lymphocytes are targeted to the tumour cells for further destruction while the OV spreads to infect new tumour cells. Created in BioRender.*

The release of new OV particles during ICD promotes infection of neighbouring tumour cells and distant metastatic sites. It also induces anti-viral immune responses that can benefit or hinder tumour regression [75,77]. Efficient spread of the OV requires sufficient time before lysis for an infected cell to reproduce more viral progeny. As such, anti-viral responses could reduce the efficacy of OV therapy by limiting viral replication. On the other hand, anti-viral responses provide another mechanism by which the immune system can target tumour cells constantly shifting between immune evasion mechanisms. All together, an optimal balance between intertwined immune responses must be achieved for the success of OV therapy [75,77]. Researchers are still working to understand this optimal balance and learn how to elicit it during OV therapy.

Finally, OV therapy can be enhanced by various mechanisms, such as transgene expression and co-treatment regimes. Transgenes encoding for pro-inflammatory cytokines (most commonly GM-CSF) can be inserted into the OV genome and augment immune responses to therapy. Syngeneic action has also been noted between OV therapy and specific chemotherapy drugs. Chemo-sensitizing effects have been attributed to the increased presence of inflammatory immune cells in the TME, such as CD8+ T cells and M1 macrophages, achieved by OV therapy [41,78]. In reverse, certain chemotherapy drugs can help reduce the presence of immune-suppressive cell types in the TME, which can help pave the way for OV success [79–81]. Taxol-based drugs and gemcitabine have been previously shown to deplete immunosuppressive MDSCs in the TME of murine models [79–81].

1.3.2 HSV-1-γ34.5

The Herpes Simplex Virus Type I (HSV-1) provided the backbone for the first FDA-approved OV, known as T-VEC, and is a predominant OV featured in clinical trials[82]. HSV-I has succeeded as an OV due to broad oncotropism, a large genome with space for transgene

insertion, and natural cytolytic activity[83]. The availability of existing HSV-I attenuating drugs boosts the safety profile of this OV should any adverse patient reactions occur with treatment[83].

A key protein encoded by the HSV-I genome during replication is γ34.5. The γ34.5 protein aids in escape by HSV-I via resuscitation of host-cell protein synthesis[78,84]. Upon viral infection, IFN-I is induced to mediate anti-viral response pathways and clear HSV-I from the host cell. The host cell is directed to shut off protein synthesis by activating protein kinase R, which disables the translation initiation factor eIF2α via phosphorylation. As a result, both host and viral protein synthesis become impaired. The γ34.5 protein reverses this inhibition by directing phosphatase PP1α to dephosphorylate eIF2α and force the resumption of protein synthesis required for HSV-I replication[84,85]. The function of γ34.5 in HSV-I infection is illustrated in **Figure 6**.

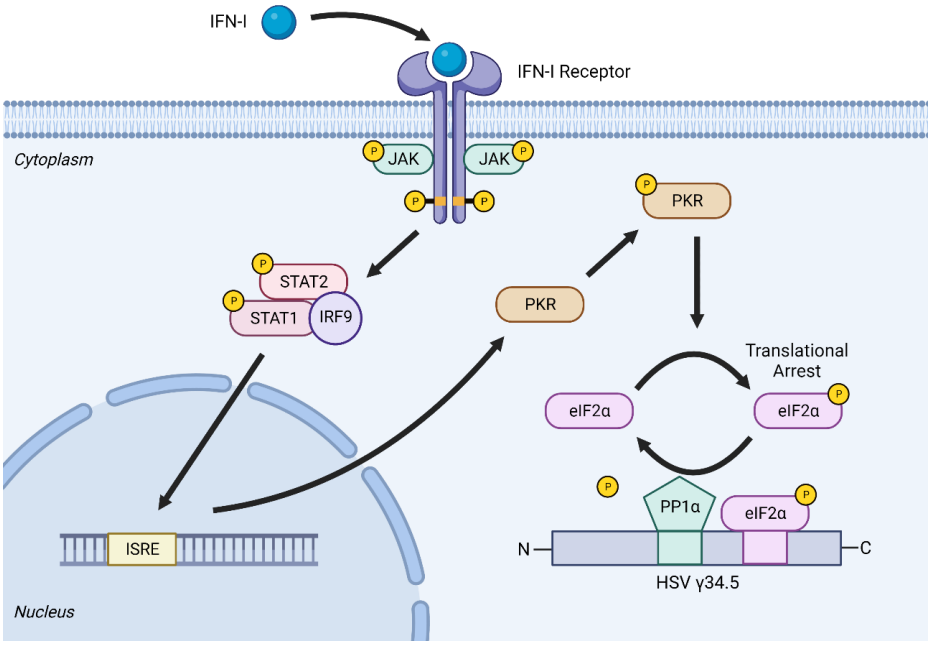

Figure 6: γ34.5 mutation reverses HSV-I induced shut-off of host protein synthesis. *Infection with HSV-I encoding wild-type γ34.5 reverses the shut-off of host protein synthesis due to the inactivation of eIF2α. Key proteins include Janus tyrosine kinase (JAK), signal transducers and activators of transcription (STAT), interferon regulatory factor 9 (IRF9), interferon-stimulated regulatory element (ISRE), protein kinase RNA-activated (PKR), eukaryotic translation initiation factor 2A (eIF2a), and protein phosphatase 1A (PP1α). Created in BioRender.*

The gene encoding γ34.5 is deleted in many HSV-I-based OVs for two main reasons [85]. Firstly, γ34.5 is required for full neurovirulence of HSV-I. As such, its deletion reduces off-target and adverse side effects of HSV-I treatment. Secondly, γ34.5 deletion confers enhanced tumour specificity because most tumour cells cannot initiate a strong IFN-I response. Healthy cells are able to undergo normal IFN-I mediated shut-off protein synthesis to attenuate HSV-I replication without interference by γ34.5. Tumour cells, on the other hand, do not induce sufficient IFN-I to achieve the same response and thus will support HSV-I replication despite the absence of γ34.5.

1.3.3 VVDD

Vaccinia virus (VV) is a member of the *Poxviridae* family and carries a dsDNA genome. It is commonly recognized as the basis of the vaccine used to eradicate smallpox. Similar to HSV-I, the large genome of VV lends itself well to the insertion of transgenes to enhance therapeutic efficacy. VV is a promising OV treatment due to its rapid replication, cytoplasmic life cycle ensuring host genome protection, and broad oncotropism[86]. This virus was previously shown to successfully control OC tumours in an *in-vivo* study[87].

Deletion of the vaccina growth factor (VGF) and thymidine kinase (TK) genes are commonly used to enhance the safety and tumour specificity of VV therapy. The highly-virulent Western Reserve strain of VV has been modified to include double mutation (VVDD) in these two genes. This genetically engineered combination was first described in the early 2000s after enhanced VV oncotropism was found upon deletion of either VGF or TK alone compared to the WT strain[88].

VGF is encoded twice in the VV genome and shares homology with epidermal and transforming growth factors. VV host cells secrete VGF to prime neighbouring tissue for

infection and enhance viral spread. VGF deletion reduces virulence and is important for the safety profile of VV as an OV[88,89]. TK is a critical enzyme for DNA synthesis and catalyzes the conversion of deoxythymidine to deoxythymidine 5' phosphate. When TK is deleted, viral replication relies on the available pool of nucleotides present in the host cell. Cancer cells are fast-growing hosts and typically boast large nucleotide reserves to support constant replication; this commonality is thought to be the basis for the tumour specificity of TK deleted VV strains[88,90]. One of the most commonly used VV platforms in pre-clinical study is JX-549, which includes deletion of TK and addition of a transgene encoding granulocyte-macrophage colony-stimulating factor[90].

Pre-clinical models utilizing immune-competent mice have shown nearly no viral recovery after infection with VVDD[88]. VVDD has since been found to be well-tolerated in human patients and exhibits selective tumour infection that elicits anti-tumour activity[91].

1.3.4 VSVΔM51

Vesicular stomatitis virus (VSV) is a *Rhabdovirus* built on a negative-sense single-stranded RNA genome. The small VSV genome encodes for only five proteins, allowing for rapid completion of the viral life cycle and quick production of new viral particles. VSV is favoured for its ability to grow to high titers, low levels of pre-existing immunity in the global population, and easy-to-modify genome[92–94]. This virus enters the cells through the ubiquitously expressed low-density lipoprotein receptor (LDLr)[95]. It has shown success against tumours with various genetic mutations, including those involved in the TP53 and RAS pathways[96].

The matrix (M) protein is a highly versatile component of VSV that plays multiple functional and structural roles. Notably, the M protein can halt host cell protein synthesis and

induce cell apoptosis through well-defined mechanisms (outlined in **Figure 7** and the below paragraphs), thus shifting host cell molecular pathways to favour VSV replication.

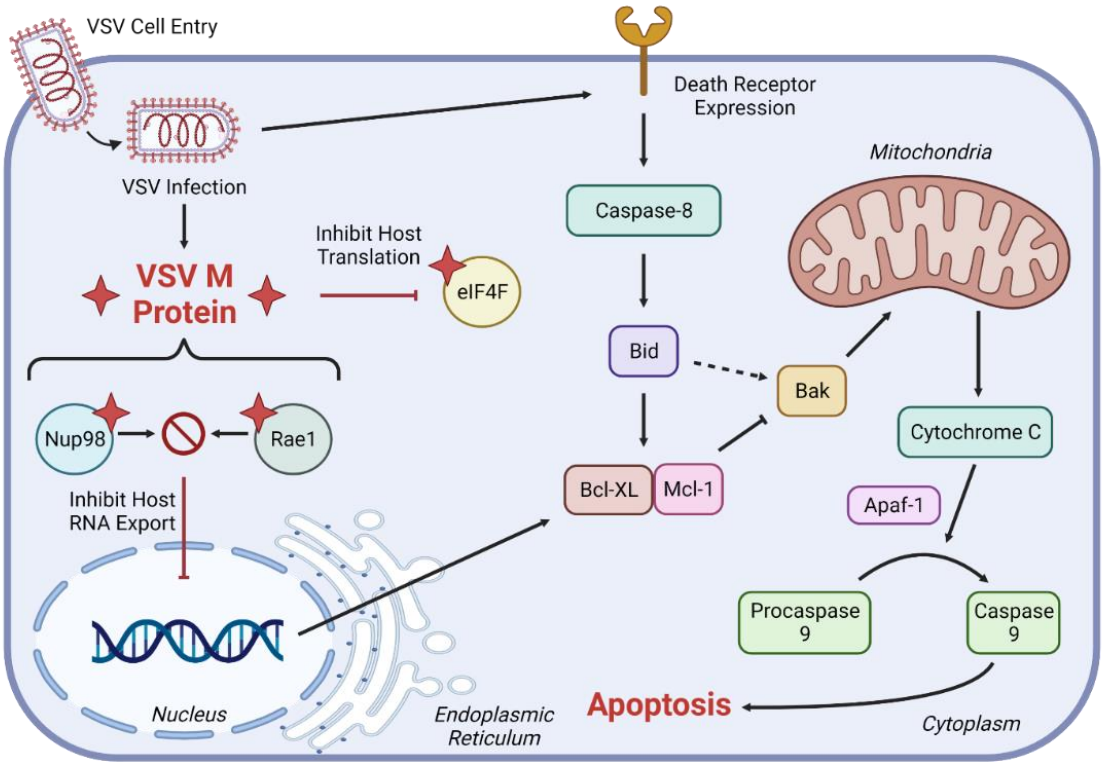

Figure 7: Mechanisms used by the VSV M protein to inhibit host protein synthesis and initiate apoptosis. *The VSV M protein inhibits host translation by preventing appropriate interaction of nucleoporin (Nup98) and ribonucleic acid export (Rae1), or by inhibiting the function of eukaryotic initiation factor 4F (eIF4F). VSV infection stimulates apoptosis through caspase-8 mediated pathway. Other abbreviated protein names include B-cell lymphoma XL (Bcl-XL), myeloid leukemia cell differentiation protein (Mcl-1), and apoptotic peptidase activating factor 1 (Apaf-1). Created in BioRender.*

Firstly, the M protein turns off host mRNA export by forming a binding complex with the nucleoporin Nup98 and nuclear export factor Rae1. Complex formation is achieved due to structural components of the M protein that mimic the phosphate backbone of nucleic acids and bind in its place to Rae1[93,97,98]. As a result, the M protein prevents appropriate interaction between Rae1-Nup98, and host mRNA export is thus halted. Importantly, this function of the M protein does not require assistance from other viral components and is achieved independently

from its role in virus assembly[99]. Secondary to this mechanism, the VSV M protein inhibits host translation factor eIF4F. This function further inhibits host protein synthesis and ensures priority use of the protein synthesis machinery by VSV.

Upon infection, the M protein mediates the overexpression of Bcl-2 as a mechanism of delaying VSV-induced apoptotis[100]. This ensures sufficient time for viral replication before cell death[100]. It is important to note that translation of the viral genome is unaffected by these mechanisms due to several VSV modifications, including unique *cis*-acting elements in the 5' end of the viral mRNA and the completion of the VSV life cycle outside of the nucleus[93].

To ensure tumour cell specificity when used as an OV, VSV is commonly mutated at the M protein methionine position 51 (ΔM51) to allow for host mRNA nuclear export and translation. This mutation takes advantage of a trait common to many cancer types, including EOC: a severely impaired capacity to produce IFN-I in response to host cell viral infection. VSV is highly sensitive to anti-viral IFN-I[101]. When infected with VSVΔM51, healthy cells can easily combat VSV infection with strong IFN-I induction. Infected tumour cells will fail to inhibit VSV infection due to poor capacity for IFN-I induction. In addition to improving tumour specificity, the ΔM51 mutation of VSV also enhances pathogenesis by inducing TNF-α[102].

1.4 Rationale, Hypothesis & Aims

1.4.1 Rationale

There is an urgent need for the development of novel HGSC therapies. The current standards of care – platinum-based chemotherapy and surgical debulking – fail to provide effective long-term responses for most patients. Successful therapy of HGSC must overcome carboplatin resistance and combat immune suppression in the TME across a diverse group of tumours with specific genetic mutations. Many immune therapies are currently in development to achieve this goal. OV therapy is one front-runner due to the ability of this biologic to activate critical anti-tumour and anti-viral immune responses in the TME. This mechanism of action is achieved while specifically replicating within and lysing tumour cells, leaving healthy tissue unharmed and reducing systemic side effects.

Clinically relevant models used to evaluate OV therapies against HGSC are extremely important to represent the heterogeneity of this disease. These models must include specific genetic mutations and represent both the OSE and FTE origins of HGSC to comprehensively assess novel therapeutic efficacies. In studying the therapeutic benefits of OVs *in-vivo*, syngeneic models of HGSC reign superior due to their fully-functional immune system that critically determines the responsiveness to therapy. Investigations by multiple research groups, including the Vanderhyden lab, have already begun to characterize many such syngeneic models of HGSC, including those harbouring specific tumour mutations[55,56]. The responses of these models to the standard of care (ex. carboplatin) and a diverse array of promising HGSC treatments (including OVs) remains to be thoroughly evaluated.

In response to the potential for therapeutic advancement, this project assessed the impact of clinically relevant mutations on chemotherapy resistance and the response to OV immunotherapy in diverse murine models of HGSC.

1.4.2 Hypothesis

I hypothesize that the sensitivity of HGSC models to chemotherapy and OV infection will be influenced by the presence of clinically relevant, specific mutations. These mutations are predicted to do so by uniquely orchestrating tumour cell growth, OV replication and TME immune landscape in the pre-clinical models studied.

1.4.3 Aims

1. Evaluate the effects of specific tumour mutations on chemotherapy sensitivity, *in-vitro* and *in-vivo.*
2. Characterize the effects of specific tumour mutations on OV infection *in-vitro.*
3. Assess the survival and immune responses of *in-vivo* syngeneic tumour models with specific mutations after OV infection.

Chapter 2: Methods

2.1 Cell Lines

All three murine HGSC cell models and their mutant derivatives, as introduced above, were included in the present research project. This includes ID8 cells with *Trp53*$^{-/-}$ mutation alone and in combination with *Brca1*$^{-/-}$, *Brca2*$^{-/-}$, *Nf1*$^{-/-}$, or *Pten*$^{-/-}$. The ID8 C3 cells were the non-mutated CRISPR-Cas9 control for this group. STOSE cells without modification were included. MOE cells were used with *Pten*^{shRNA} mutation alone and in combination with *Trp53*^{R273H} or *KRas*^{G12V}. The culture conditions for all murine cell lines are summarized in **Table 1**.

Table 1: Cell line information and culture conditions for murine HGSC models. *All cell lines were cultured at 37ºC with 5% CO_2 in filter-sterilized media.*

Cell type(reference)	Known Mutations	Origin	Culture Condition
ID8 WT (69,70)	None	C57BL/6, OSE	DMEM[1]+ 4% FBS[2] + ITSS
ID8 *Trp53*$^{-/-}$ (69,70)	*Trp53*$^{-/-}$		
ID8 *Trp53*$^{-/-}$ *Brca1*$^{-/-}$ (69)	*Trp53*$^{-/-}$, *Brca1*$^{-/-}$		
ID8 *Trp53*$^{-/-}$ *Brca2*$^{-/-}$ (69,70)	*Trp53*$^{-/-}$, *Brca2*$^{-/-}$		
ID8 *Trp53*$^{-/-}$ *Nf1*$^{-/-}$ (69,70)	*Trp53*$^{-/-}$, *Nf1*$^{-/-}$		
ID8 *Trp53*$^{-/-}$ *Pten*$^{-/-}$ (69,70)	*Trp53*$^{-/-}$, *Pten*$^{-/-}$		
STOSE (13)	None	FVB/N, OSE	α-MEM[3]+ 4% FBS + ITSS[4] + EGF[5]
MOE *Pten*^{shRNA} (17,19)	*Pten*^{shRNA}	FVB/N, MOE	α-MEM + 4% FBS + ITSS + EGF + β-Estradiol[6]
MOE *Pten*^{shRNA} *Trp53*^{R273H} (17,19)	*Pten*^{shRNA}, *Trp53*^{R273H}		
MOE *Pten*^{shRNA} *KRas*^{G12V} (17,19)	*Pten*^{shRNA}, *KRas*^{G12V}		

[1]Dulbecco's Modified Eagle's Medium (Corning; #10-013-CV)
[2]Fetal Bovine Serum (Glibco, #12483-020)
[3]Minimal Essential Media (Glibco, #12571-063)
[4]1x Insulin-Transferrin-Selenium (Sigma Roche, #11074547001)
[5]Murine Epithelial Growth Factor, 2µg/mL (Cedarlane; #2028-EG-200)
[6] β-Estradiol, 18.2ng/mL (Sigma; #E2257)

Vero cells, derived from the kidney of the African Green Monkey, are highly susceptible to OV infection[103]. As such, they were used for the propagation and titration of VSV virus strains. Vero cells were maintained in complete media (CM): DMEM (Corning; #10-013-CV) + 10% Fetal Bovine Serum (FBS, Gibco; 12483-020).

All cell lines were regularly tested for infection with mycoplasma approximately every four months and before mouse injection *in-vivo*. Testing was performed via polymerase chain reaction using a commercial kit (Cedarlane; #G238-AG) following the manufacturer's protocol.

2.2 Oncolytic Virus Strains and Preparation

2.2.1 Oncolytic Virus Strains

Three promising OVs were selected for initial study and are briefly summarized in **Table *2*** (in-depth background found in **Section 1.3)**. All viruses used for this project were generously provided by the Diallo Lab at the Ottawa Hospital Research Institute. The virus stocks were received previously purified and quantified via plaque assay and stored at -80°C.

Table 2: Summary of oncolytic virus selections and genomic alterations.

Oncolytic Virus	Family	Genome Alterations	Genome Type
HSV-1-γ34.5	*Herpesviridae*	γ34.5 deletion	150kb dsDNA
VVDD	*Poxviridae*	Deletion in Thymidine Kinase & Vaccinia Growth Factor genes	190kb dsDNA
VSVΔM51	*Rhabdoviridae*	Matrix protein M51 mutation (ΔM51)	11kb ss(-)RNA
VSVΔM51-GFP		Matrix protein M51 mutation (ΔM51); Green fluorescent protein (GFP) transgene	
VSVΔM51-FLuc		Matrix protein M51 mutation (ΔM51); Firefly Luciferase (Fluc) transgene	

Virus stocks for HSV-1-γ34.5, VVDD, and VSVΔM51-FLuc were obtained in sufficient quantities for completion of this project; as such, the donated stocks were used directly for experimental purposes. Production of additional VSVΔM51 and VSVΔM51-GFP stocks was required to yield sufficient stock quantities of virus for all experiments; the details of this process are described in the following section.

2.2.2 VSVΔM51 Propagation and Purification

Viral propagation and purification were required to create a sufficient stock of the VSVΔM51 and VSVΔM51-GFP viruses. All steps were completed adhering to the protocol described previously by Diallo et al.[104] with the following minor modifications. Firstly, viral supernatant was collected after VSV had been sufficiently propagated in Vero cells, as noted by cell morphology changes. Secondly, two rounds of high-speed centrifugation were required to accommodate the large volume of viral supernatant created by mass batches of virus production. These two centrifugation steps were necessary to A) reduce the volume of viral supernatant and B) pool the concentrated supernatants before it was possible to proceed with production.

Finally, the OptiPrep® gradients were prepared manually via successive layering of solutions C and D, pre-mixed at the appropriate ratios. This procedure was completed without the use of a gradient maker. To maintain the unique density of each OptiPrep® layer during preparation, the gradient tube and its contents were frozen using a dry ice bath between addition of successive density layers. All virus stocks purified using the OptiPrep® gradients were collected and quantified via standard plaque assay prior to use.

2.2.3 Standard Plaque Assay

Standard plaque assay allowed for quantification of the active viral particles within each virus stock. Quantification of VSVΔM51 -GFP, and -FLuc was performed as described by Diallo

et al.[104] with one modification. The initial infection time, during which cells were treated with VSVΔM51 diluted in serum-free DMEM (DMEM-Ø), was extended from 45 minutes to 1.5 hours. Quantification of HSV-1-γ34.5 and VVDD-GFP by plaque assay was performed by the Diallo lab prior to the donation of virus stocks to this project.

2.3 In-Vitro Assays

All *in-vitro* assays were completed with cells growing in the appropriate complete media (CM, detailed in **Table 1**) at 37°C, unless noted otherwise.

2.3.1 Alamar Blue Assay

The Alamar Blue assay was used to screen for cell viability in response to treatment with the following therapeutics: carboplatin, VVDD-GFP, HSV-1-γ34.5 or VSVΔM51-GFP. All ID8, STOSE and MOE cells were seeded in 96-well, clear plates to reach 95% confluence at the time of infection. Treatment media was prepared by diluting carboplatin in CM or virus stock in DMEM-Ø, to achieve the desired drug concentration or multiplicity of infection (MOI), respectively. Note that serum free DMEM-Ø was required to support efficiency of the initial viral infection process in all cell lines. To commence cell treatment with carboplatin or OV, CM was aspirated from all wells and replaced with the treatment media for 72h (carboplatin) or 1.5 hours (OV). Carboplatin treated cells remained in the treatment media until the end of the 72h incubation; OV treatment media was aspirated after 1.5 hours and replaced with CM until the total incubation time was reached (24h, 48h, or 72h post-infection).

After the treatment incubation, AlamarBlue™ media was prepared by diluting 10% AlamarBlue™ Cell Viability Reagent (ThermoFisher; #DAL1100) in fresh CM for each cell line. Treatment media was aspirated from all wells and replaced with the new AlamarBlue™ dilution. Plates were then incubated for 3 hours in the dark: this was determined as the

appropriate incubation time for the positive control wells (untreated, healthy cells) to produce a near complete colour-change reaction. Plate reads were performed on a Bio-Tek Microplate Reader, measuring fluorescence at an absorbance of 530nm and emission of 590nm. Plates requiring multiple time-point reads were returned to the incubator until the subsequent read time (48h or 72h post-infection), at which time the Alamar Blue read procedure was repeated. The average raw measure of all negative control wells was subtracted from all samples, and the resulting data for each cell line was normalized to the untreated positive control cells (set to 100% viability).

2.3.2 Incucyte® Live-Cell Analysis

The Incucyte® Live-Cell Analysis System was used to measure proliferation rates of all ID8, STOSE and MOE cells. The cells were seeded in CM at low density in a 96-well plate (4,500 cells/well for ID8 and STOSE; 7,500 cells/well for MOE lines). Cells were placed in the Incucyte® to continue incubating under standard growth conditions (37°C with 5% CO_2) during live-cell analysis. Cell confluence was measured by the Incucyte® every 2 hours until all cell lines had reached full confluence (up to 48h required). The raw data was normalized to align the starting confluence (0h) of all biological replicates for each cell line at ~20-25% confluence. Mean confluence was compared during statistical analysis.

2.3.3 Luciferase Titration of VSVΔM51

Quantification of viral replication by infected ID8, STOSE and MOE was performed using the VSVΔM51 virus expressing the FLuc transgene. VSVΔM51-FLuc quantities in infected cell supernatants were titered using the bioluminescent signal produced when the FLuc protein interacts with its substrate, D-Luciferin. The following methods are based on the previously described protocol for titering Luciferase-expressing virus by Garcia et al[105]. ID8,

STOSE and MOE cells were seeded to reach 95% confluence at the time of infection. All media were aspirated and replaced with 500µL of the treatment media, consisting of VSVΔM51-FLuc diluted in DMEM-Ø for treatment with MOI 0 (no virus), 0.1, 1 or 10. After initial infection for 1.5h in 500µL treatment media alone, 1mL of CM was added to each well to provide additional serum to support cell growth. Simultaneously, Vero cells were seeded to reach 95% confluence on the same day in 96-well, white wall plates with 100µL CM/well.

At 6h hours post-infection, 25µL of the supernatant from the infected ID8, STOSE and MOE cells was collected and applied directly to the pre-seeded Vero cells without aspirating the existing CM. The Vero cells were then infected for three hours. Next, an additional 25µL of 2mg/mL D-Luciferin Bioluminescent Substrate (PerkinElmer; #122799) was gently mixed into every well via a multi-channel pipette. At the same time, a standard curve was prepared by infecting Vero cells with 25µL of VSVΔM51-FLuc diluted in DMEM-Ø at known concentrations ($10e^1$ to $10e^7$). Plates were read using the Bio-Tek plate reader, measuring luminescence 30 minutes after application of the substrate; this procedure quantified the VSVΔM51-FLuc present in each well.

A Hill curve was created for each plate of infected Vero cells using the standard curve sample described above. From this plot, the concentrations of VSVΔM51-FLuc in the ID8, STOSE & MOE supernatants were calculated based on the quantified FLuc signal produced by infected Vero cells.

2.3.4 Quantitative Polymerase Chain Reaction

Analysis via quantitative polymerase chain reaction (qPCR) was used to assess changes to the expression of key genes involved in antigen presentation and cell immunogenicity after VSVΔM51 infection. Cells were seeded to reach 95% confluence on the day of infection and

treated with VSVΔM51-GFP at an MOI of 0.1 for 0 (no-infection control), 6 or 12 hours. All infections began with cells growing for 1.5 hours in DMEM-Ø infection media, which was replaced with CM for the remaining incubation time. After treatment, cells were collected, washed in Phosphate Buffered Saline (PBS, Glibco™; #14190-144), and stored at -80°C until RNA extraction.

RNA was extracted from all samples using either the RNeasy® Mini Spin Kit (Qiagen; #74106) or RNeasy® Plus Mini Spin Kit (Qiagen; #74136) as per the manufacturer's protocol. cDNA was then prepared from each sample using the iScript™ Reverse Transcription Supermix (Bio-Rad; #1708841) as per the manufacturer's protocol.

All primers used for qPCR were previously designed and validated by the Vanderhyden Lab; extensive screening of primer efficiency and specificity ensured reliability of results. A summary of all primers used is shown in **Table 3**. GAPDH, HRPT1 and β-ACTIN were used as housekeeping genes to normalize experimental samples.

Table 3: Summary of qPCR primer nucleotide sequences. *The Vanderhyden lab previously validated all primers to ensure murine genes were targeted with efficiency and specificity.*

Gene of Interest	Forward Primer	Reverse Primer
Gapdh	ACAACTTTGGCATTGTGGAA	GATGCAGGGATGATGTTCTG
Hrpt1	AGGACCTCTCGAAGTGTTGG	CGTGATTCAAATCCCTGAAG
β-Actin	CCTTCCTTCTTGGGTATGGA	ACGGATGTCAACGTCACACT
Ldlr	GCAGCCACATGGTATGAGGT	CTGACCATCTGTCTTGAGGGG
B2M	ACCGTCTACTGGGATCGAGA	TGCTATTTCTTTCTGCGTGCAT
H2Kb	GCTGGTGAAGCAGAGAGACTCAG	GGTGACTTTATCTTCAGGTCTGCT
K2Db	AGTGGTGCTGCAGAGCATTACAA	GGTGACTTCACCTTTAGATCTGGG
H2Kq	ACGACACTGAGTTGGTGCGTTGAC	ACTCTGCTCATTGTCCTTGGCGTTGAC
PD-L1	CAGCAACTTCAGGGGGAGAG	TTTGCGGTATGGGGCATTGA
Ifn-β	AAGAGTTACACTGCCTTTGCCATC	CACTGTCTGCTGGTGGAGTTCATC
Ifn-γ	TTGCCAAGTTTGAGGTCAACAA	CGCTTCCTGAGGCTGGATTC

2.3.5 Flow Cytometry of In-Vitro Samples

Flow cytometry was used to assess immunogenicity changes in ID8, STOSE and MOE after VSVΔM51-GFP infection. Confluent cells were infected for 6h with VSVΔM51-GFP at MOI 0, 0.1, 1 and 10. As with previous experiments, cells were initially incubated with VSVΔM51-GFP diluted in DMEM-Ø for 1.5 hours before the infection media was replaced with CM for the remainder of the 6-hour incubation period. Cells were then collected for staining in a V-bottom 96-well plate and protected from light after the first round of staining commenced.

Cells bound for the experimental treatment and control groups were first washed in PBS (Glibco™; #14190-144) before incubating in viability stain dilution for 15 minutes. A wash in PBS + 2% FBS (Glicbo™; #12483-020) was applied before staining (all antibodies used for flow cytometry *in-vitro* are listed in **Table 4**). Cells were then co-stained for 15 minutes with both PD-L1 and MHC-I (either H2K/Db or H2Kq antibodies for C57BL/6 or FVB/N derived cell lines, respectively) antibodies simultaneously. Finally, cells were washed in PBS + 2% FBS cells and fixed by resuspension in paraformaldehyde 1%. All samples were kept in the dark at 4°C until data acquisition using the BD LSRFortessa™ in the University of Ottawa Flow Cytometry and Virometry Core Facility.

Table 4: Summary of anti-mouse antibodies used for in-vitro flow cytometry staining. *All antibodies are anti-mouse targeting and were previously optimized in the Vanderhyden lab.*

Antibody Target	Fluorochrome	Staining Dilution	Company; Catalogue #
Fixable Viability Stain (FVS)	BV510	1:1000	BD BioSciences; #564406
PD-L1	PE	1:200	BioLegend; #124308
H2K/Db	APC	1:200	BioLegend; #114614
H2D/Lq	BV711	1:200	BD BioScience; #745487

Raw data collected from acquisition was processed using FlowJo™ version 10.8.1 to determine the percent expression of the above markers and MFI values, which could then

undergo statistical analysis (see section 2.5 for statistical analysis). The specific gating strategy applied to all samples is presented in the appendix (section **5.1.1**, **Figure 25**) and summarized in the following sequential steps: 1) exclusion of cell debris, 2) gating of single cells, 3) application of PD-L1, H2K/Db, H2D/Lq and GFP gates based on the appropriate negative control samples (fluorescence minus one controls).

2.3.6 Cell Microscopy

Cell images were taken 6 hours after VSVΔM51-GFP infection in samples bound for flow cytometry (see section 2.3.5 for full infection protocol). These include samples of ID8, STOSE and MOE cells infected at MOI 0 (no virus), 0.1, 1 and 10. Light microscopy images were taken to show the confluent cell monolayer, and pictures were taken on the green fluorescence channel to identify VSVΔM51-GFP infected cells. Images were adjusted to normalize brightness with no changes to contrast.

2.4 In-Vivo Tumour Models

2.4.1 Syngeneic Models of Murine HGSC

Six syngeneic IP tumour models were used to assess the ability of carboplatin and VSVΔM51 monotherapy to prolong survival in murine HGSC models with clinically relevant, specific tumour mutations. Information for all models used is summarized in **Table 5**. All mice were housed in the Animal Care and Veterinary Services (ACVS) facilities at the University of Ottawa in conditions meeting or exceeding the ethical standards set by the Canadian Council for Animal Care. All *in-vivo* studies were performed under a protocol approved by the University of Ottawa's Animal Care Committee. Mice were given ad-libitum access to standard chow and water. Facility veterinary staff monitored the mice closely to ensure humane care by distributing

extra enrichments and medical treatment as needed. All mouse euthanasia procedures were performed via CO_2 exposure, followed by manual dislocation of the cervical spine.

The C57BL/6 (The Jackson Laboratories; strain ID #664) and FVB/N (Charles River Laboratories; strain ID #207) mice were used as syngeneic tumour hosts for the ID8 and STOSE/MOE models, respectively. For all models, cells were implanted into 6–8-week-old mice via IP injection of $5e^6$ tumour cells. Treatment regimes with carboplatin, VSVΔM51 or the appropriate control began at 25% of the expected survival time for untreated mice, as determined previously by the Vanderhyden lab.

Table 5: Summary of syngeneic murine models of HGSC with specific tumour mutations. *Mice received tumour cell injections ($3e^8$ cells) via IP injection on day 0. 25% of expected survival was identified as the treatment start time for VSVΔM51 or carboplatin dosing.*

Tumour Model ***($5e^6$ IP injected cells)***	**Syngeneic Host Strain**	**Expected Survival of Control Mice** ***(days since tumour cell implant)***	**25% Expected Survival** ***(days since tumour cell implant)***
ID8 C3	C57BL/6	120	30
ID8 *Trp53*$^{-/-}$ F3		55	14
ID8 *Trp53*$^{-/-}$ *Brca1*$^{-/-}$		55	14
STOSE	FVB/N	75	19
MOE *Pten*^{shRNA} *Trp53*^{R273H}		50	13
MOE *Pten*^{shRNA} *KRas*^{G12V}		28	7

2.4.2 Carboplatin Treatment of Syngeneic HGSC Models

Five of the six syngeneic models described in section 2.4.1 were used to assess the ability of carboplatin treatment to prolong survival in murine HGSC models with specific tumour mutations: these were mice bearing ID8 C3, ID8 *Trp53*$^{-/-}$ F3, STOSE, MOE *Pten*^{shRNA} *Trp53*^{R273H} and MOE *Pten*^{shRNA} *KRas*^{G12V} tumours. At 25% of expected survival (see **Table 5**), mice were administered the first of three IP doses of carboplatin at 12.5 mg/kg or saline control

(200-240μL volume per injection based on mouse size, n=5 mice per treatment group). The remaining doses were given 7 and 14 days after the initial treatment. Mice were held in a designated cytotoxic chemical treatment room within the uOttawa ACVS containment level-1 facilities until 2-weeks after the final dose, when mice could be returned to general housing.

After treatment, mice were closely monitored and euthanized at a humane endpoint to assess survival outcomes. Observations resulting in humane endpoint included loss of mobility, loss of skin pigmentation, presence of abdominal distension due to ascites and visible signs of distress. Necropsy was performed to measure total tumour weight, ascites volume, and spleen weight. This study was repeated twice with n=5 mice per treatment group in each cohort once again, and the results presented show the pooled data from both cohorts.

2.4.3 VSVΔM51 Treatment of Syngeneic HGSC Models

All six of the syngeneic models described in section 2.4.1 were used to assess the ability of VSVΔM51 treatment to prolong survival in murine HGSC models: these were mice bearing ID8 C3, ID8 *Trp53*$^{-/-}$ F3, ID8 *Trp53*$^{-/-}$ *Brca2*$^{-/-}$, STOSE, MOE *Pten*^{shRNA} *Trp53*^{R273H} and MOE *Pten*^{shRNA} *KRas*^{G12V} tumours. At 25% of the expected duration of survival (**Table 5**), mice were administered the first of three IP doses of 3e^{8} particle forming units (PFU) VSVΔM51 or PBS control (100μL volume per injection, n=8 mice per treatment group). The remaining two doses were given 3 and 6 days after the first treatment dose.

During treatment, mice were held in Containment Level 2 within the uOttawa ACVS facilities until two weeks after the final dose, when mice could safely be returned to general housing (Containment Level 1). After treatment, mice were closely monitored and euthanized at

a humane endpoint to assess survival outcomes. Necropsy was performed to measure total tumour weight, ascites volume, and spleen weight.

2.4.4 Collection of TME Samples from Syngeneic HGSC Models

Treatment of the MOE *Pten*^{shRNA} *KRas*^{G12V} and ID8 *Trp53*$^{-/-}$ *Brca1*$^{-/-}$ syngeneic models with VSVΔM51 (section 2.4.3) resulted in prolonged survival compared to PBS control-treated mice. These two models were repeated using identical methods as described above, with n=5 mice per treatment group. All mice were euthanized five days after the last VSVΔM51 treatment to assess the immune landscape of the TME. Peritoneal wash was completed to collect tumour cells from the abdominal cavity, a representation of the ascites TME (performed due to minimal to no ascites to collect at this early timepoint). 5 mL of PBS-EDTA was delivered into the abdominal cavity via IP injection and incubated for five minutes while gently palpating the mouse abdomen. Peritoneal wash was recovered via an incision in the abdominal cavity. Mice were then carefully dissected to collect the mesenteric lymph nodes (mLN) and spleens, which were placed in tubes containing PBS + 2% FBS on ice. Both solid tissue sample types were homogenized using abrasive glass cover slips and the cells were re-suspended in PBS + 2% FBS.

All peritoneal washes, mLN and spleen samples were strained using 70μM cell strainers (Fisher Scientific; #22-363-548) to remove any non-dissociated tissue and washed in PBS + 2% FBS. Ammonia-Chloride-Potassium Lysing Buffer (Fisher Scientific; #A10492-01) was applied for 3 minutes to remove red blood cells. Cells in each sample were manually counted and stained for flow cytometry (section 2.4.5).

2.4.5 Flow Cytometry of In-Vivo Samples

All antibodies used for staining the TME samples (section 2.4.4) are listed in **Table 6**. Samples were protected from light as much as possible to prevent deterioration of the staining.

First, a fixable viability stain was applied to all samples, diluted in serum-free PBS, for 15-minutes. Cells were washed in PBS + 2% FBS. A 5-minute Fc block (BD Bioscience; #553142) was applied to all samples. Each sample was then divided for staining with one of two separate panels of antibody master mixes (diluted in PBS + 2% FBS) for 20 minutes. Cells were washed in cold PBS + 2% FBS, fixed with a paraformaldehyde 1% solution, and kept in the dark at 4°C until acquisition using the Cytek® Aurora in the University of Ottawa Flow Cytometry and Virometry Core Facility.

Table 6: Flow cytometry antibodies for TME immune analysis of VSVΔM51 treated mice. *The Vanderhyden lab previously optimized all antibodies used for flow cytometry.*

Panel	Target	Fluorochrome	Staining Dilution	Company; Catalogue #
1	Viability	BV510	1:1000	BD Bioscience; # 564406
	CD3e	BV650	1:100	BD Bioscience; #564378
	CD45	PerCP-Cy5.5	1:200	BD Bioscience; #550994
	CD4	APC-H7	1:200	BD Bioscience; #560181
	CD8	PE-Cy7	1:200	BD Bioscience; #552877
	CD25	BV421	1:200	BD Bioscience; 562606
	LAG3	BV605	1:200	BD Bioscience; #745214
	PD-1	BV786	1:200	BioLegend; #135225
	NKp46	BV711	1:200	BioLegend; #740822
	DX5	FITC	1:200	BD Bioscience; #553126
	NKG2D	PE-CF595	1:200	BD Bioscience; #562614
2	Viability	BV510	1:1000	BD Bioscience; # 564406
	CD3e	BV605	1:200	BD Bioscience; #100351
	CD45	PerCP-Cy5.5	1:200	BD Bioscience; #550994
	CD11c	PE-Cy7	1:200	BD Bioscience; #558079
	CD11b	BV786	1:400	BD Bioscience; #740861
	CD86	PE	1:200	BD Bioscience; #553692
	I-A/I-E	BV650	1:200	BD Bioscience; #563415
	PD-L1	APC	1:200	BD Bioscience; #564715
	Gr1	FITC	1:200	BD Bioscience; #553126
	F4/80	BV421	1:150	BD Bioscience; #565411
	CD8	BUV615	1:200	BD Bioscience; #613004
	NK1.1	APC-Cy7	1:200	BD Bioscience; #560618

Raw data collected from the acquisition was processed using FlowJo™ version 10.8 to determine immune cell population frequencies and the MFI of the above surface markers; these values could then be compared by statistical analysis (see section 2.6). The gating strategy for each staining panel is shown in the appendix as applied in sequential order (section 5.1, **Figure 26** and **Figure 27**) and is the sequential steps summarized below. Note that "parent" population refers to the current cell population of interest minus the last applied gate (ex. parent population of $CD45^+$ $CD3^+$ $CD8^+$ cytotoxic T cells is population of all $CD45^+$ $CD3^+$ T lymphocytes).

Panel 1 (**Table 6**) selected for and separated lymphoid immune cell populations based on the following strategy: 1) gating of single cells, 2) exclusion of cell debris, 3) exclusion of dead cells, 4) selection of CD45+ leukocytes, 5) separation of CD3+ T cells ($DX5^-$ $CD3^+$), NK-T cells ($DX5^+$ $CD3^+$), and NK cells ($DX5^+$ $CD3^-$), 6) separation of CD8+ cytotoxic T cells ($CD8^+$ $CD4^-$) and CD4 helper T cells ($CD8^-$ $CD4^+$) within the CD3+ population. All separated populations were assessed for PD-1, LAG3 and CD25 expression. NK cell populations were additionally assessed for NKp46 and NKG2D expression.

Panel 2 (**Table 6**) selected for and separated myeloid immune cell populations based on the following strategy: 1) gating of single cells, 2) exclusion of cell debris, 3) exclusion of dead cells, 4) selection of CD45+ leukocytes, 5) selection of myeloid cells ($DX5^-$ $CD3^-$), 6) separation of cDC-1 ($CD11b^-$ $CD11c^+$), cDC2 ($CD11b^+$ $CD11c^+$), and non-DC myeloid cells ($CD11b^-$ $CD11c^-$), 7) further separation of non-DC myeloid cells by exclusion of granulocytes ($Gr1^{high}$) and subsequent selection of macrophages ($F4/80^{high}$). All separated populations were assessed for PD-L1, MHC-II, and CD86 expression.

2.5 Statistical Analysis

All statistical analyses were performed using GraphPad Prism (version 9.0 or higher) unless otherwise noted. The significance level was set *a priori* to 0.05 for all statistical tests.

Two-way ANOVA tests were used frequently to compare the impact of genetic mutation in HGSC cell models *in-vitro* amongst ID8 and STOSE/MOE cell lines. Depending on the experiment, either Tukey's or Dunnett's post hoc test was applied. In the case of Dunnett's post hoc test, the ID8 *Trp53*$^{-/-}$ F3 and MOE *Pten*^{shRNA} cells were set as the control comparator, respectively, for each cell group in this analysis. Multiple comparisons tests were set up to identify differences only amongst cells within the same treatment group (MOI or timepoint).

Incucyte® cell proliferation rates were analyzed by Melanie Grondin, a graduate student in the Vanderhyden lab. The raw data was first normalized to align the starting confluence of each biological replicate to ~20-25% for all cell lines. A logistic growth curve was fitted using the GraphPad Prism software for each cell line and an asymmetric 95% confidence interval was calculated. Outliers were removed by the Prism software using the integrated Robust Regression and Outlier Removal (ROUT) method of analysis. Cell lines were compared via one-way ANOVA with Tukey's post-hoc test to compare the mean confluence of each cell line.

The Mantle-Cox Rank-Sum test determined the significance of survival benefits in carboplatin- and VSVΔM51-treated syngeneic models, as compared to the appropriate control for each cell line. The Welch's T-test assessed the comparison of the necropsy data between VSV or carboplatin and their appropriate control counterparts.

Analysis of *in-vivo* flow cytometry data was performed using two-way ANOVA. This test was run independently for each sample type to compare PBS and VSV treated groups; as such, a full model of multiple comparisons (such as Tukey's or Dunnett's) was not required and a Bonferroni correction was applied to the comparisons.

Chapter 3: Results

3.1 Screening of Carboplatin Sensitivity in Murine HGSC Cell Lines

Screening for loss of viability in response to carboplatin (i.e. sensitivity) was performed in a diverse cohort of murine HGSC models with specific genetic mutations (**Table 1**). The carboplatin sensitivity of all cell lines was evaluated using the Alamar Blue assay. ID8 *Trp53*$^{-/-}$ *Nf1*$^{-/-}$ and ID8 *Trp53*$^{-/-}$ *Pten*$^{-/-}$ cell lines were not available in the Vanderhyden lab at the time of initial carboplatin screening; both cell lines were excluded from the further *in-vivo* analysis using carboplatin.

The ID8 C3 cells required the highest dose of carboplatin to achieve 50% loss of viability (IC50 = 77.50ng/µL) and thus were the least sensitive compared to other ID8 cell lines (**Figure 8**). Adding *Trp53*$^{-/-}$ mutation the ID8 cells enhanced sensitivity ($p<0.0001$), reducing the dosage required to achieve IC50 by nearly 75%. A combination of the *Trp53*$^{-/-}$ mutation with either *Brca1*$^{-/-}$ or *Brca2*$^{-/-}$ further enhanced the carboplatin sensitivity of the ID8 cells. These double knock-out combinations in the ID8 cells resulted in the most carboplatin-sensitive cells of all models tested, with IC50 values of 2.83ng/µL or 4.84ng/µL, respectively. STOSE cells responded to an IC50 dose of 8.52ng/µL, a relatively low dose compared to all other cell lines tested. The STOSE cells were also more carboplatin sensitive than each of the MOE cell lines. In the MOE *Pten*^{shRNA} cell lines, an additional *KRas*^{G12V} mutation significantly increased carboplatin resistance ($p<0.0001$), while *Trp53*^{R273H} mutation resulted in the opposite effect ($p<0.0001$). Thus, in both ID8 and MOE cell lines, the addition of a *Trp53* mutation increased sensitivity to carboplatin.

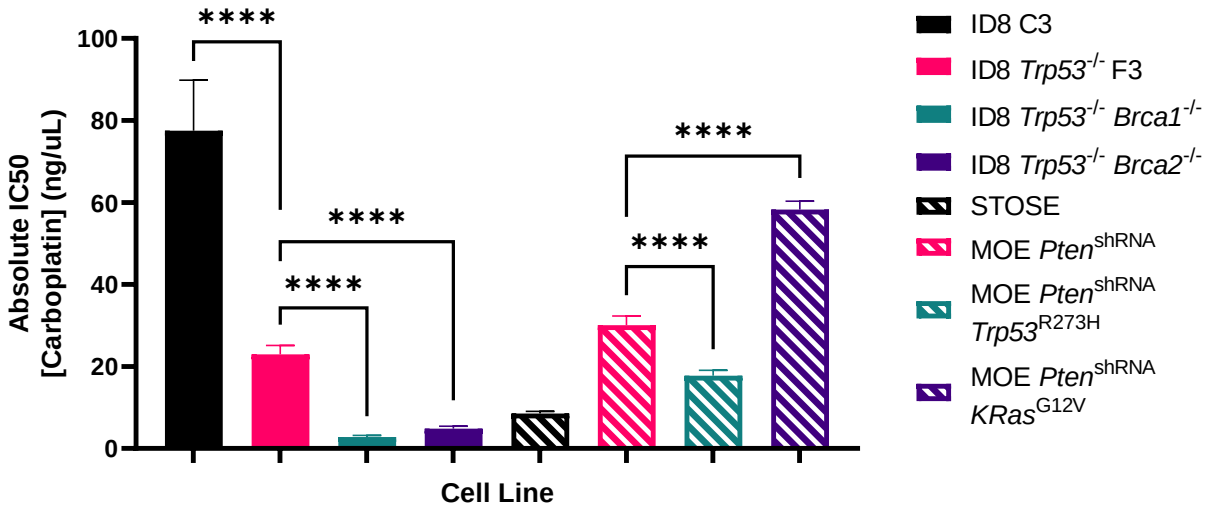

Figure 8: Carboplatin sensitivity of murine HGSC cell lines 24 hours post-treatment. *Cell lines were treated with carboplatin for 72 hours at doses ranging from 0 to 1000ng/µL diluted in CM. After treatment, the Alamar Blue assay was performed to measure cell viability. The resulting dose-response curves allowed the calculation of the IC50 for each cell line. Analysis was done via two-way ANOVA followed by Tukey's post hoc test – only the most relevant significant comparisons are shown (n=3). Error bars depict SD. ****p<0.0001.*

3.2 Screening of Oncolytic Virus Sensitivity in Murine HGSC Cell Lines

The responsiveness of the murine HGSC cell lines to OV therapy was examined next, using the same Alamar Blue method applied for carboplatin sensitivity screening. Screening of OV sensitivity was assessed using three unique OVs: VSVΔM51-GFP (**Figure 9**), VVDD-GFP (**Figure 10**), and HSV-1-γ34.5 (**Figure 11**). These three promising OVs were selected to represent very diverse types of OVs, from which a front-runner would be chosen for further analysis (the three OVs are detailed in **Table 2**).

All ID8 cell lines responded to VSVΔM51 treatment with a clear dose-dependent loss of viability, which was substantial at 24 hours post-infection and further enhanced at 48 hours post-infection (**Figure 9A**). The main effect of the virus treatment was highly significant ($p<0.0001$ at both time points). At the 24-hour timepoint, all ID8 cells showed progressively reduced viability with increasing virus treatment. After 48 hours, the viability of all ID8 cells treated with

VSVΔM51 was reduced below 20% when normalized to the untreated control cells. Only one ID8 cell line was identified as significantly different than the remaining group of cells in post hoc analysis: the ID8 *Trp53*$^{-/-}$ *Nf1*$^{-/-}$ cells had significantly higher viability than the ID8 C3 cells 24 hours post-infection at MOI 1 and 10. The interaction between the cell line and MOI main effects at both time points was found to be non-significant.

The STOSE and MOE cell lines responded more slowly to VSVΔM51 treatment than the ID8 cells (**Figure 9B**). At 48 hours post-infection, the STOSE cells achieved the greatest loss of viability with MOI 1, instead of the highest MOI treatment. MOE cell lines followed a similar trend, with a reduction of viability following an increasing treatment until minimum viability was reached at MOI 0.1 or 1. All four cell lines showed an increase in viability compared to their respective minimum at an MOI of 10. Significant comparisons between cell lines were not consistent within each MOI group. STOSE cells maintained significantly higher viability at the two lowest MOI treatments than the MOE *Pten*^{shRNA} *Trp53*^{R273H} and MOE *Pten*^{shRNA} *KRas*^{G12V} cells ($p<0.0001$). MOE *Pten*^{shRNA} single-mutant cells maintained a relatively stable level of viability across MOI treatments and are significantly more viable than the STOSE cells at MOI 0.01 and 1 ($p<0.01$). Both main effects (cell line and MOI) and the interaction effects were highly significant ($p<0.0001$).

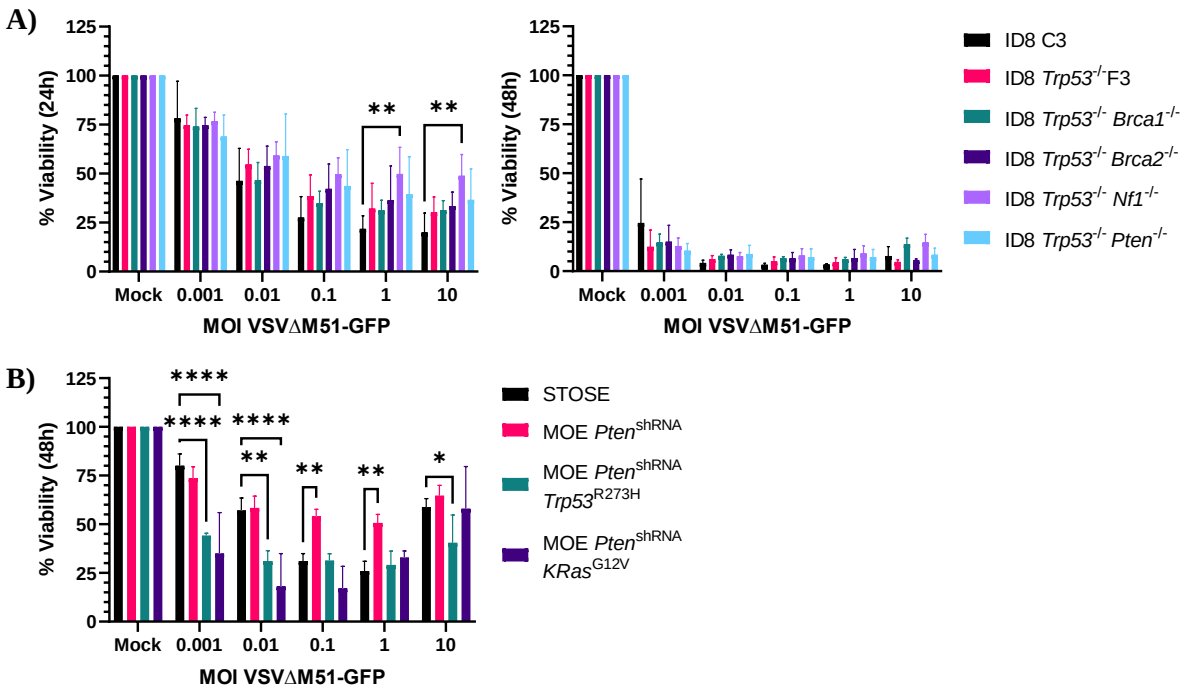

Figure 9: VSVΔM51 sensitivity of murine HGSC cell lines 24 and 48 hours after infection. *A) ID8 (24 hours on the left, 48 hours on the right), and B) STOSE and MOE cell lines (48 hours) were infected with VSVΔM51-GFP at MOI 0, 0.001, 0.01, 0.1, 1 and 10 for 24-48 hours. After completion of the infection time, Alamar Blue assays were performed to measure cell viability. Viability for each cell line was normalized to the mock (MOI 0) sample. Analysis was done via two-way ANOVA followed by Tukey's post hoc test (n=3). Error bars depict SD. *p<0.05, **p<0.01, ****p<0.0001.*

Next, all ID8, STOSE and MOE cells were tested for sensitivity to the OV VVDD-GFP. The main effect of MOI was highly significant in the ID8 cells 48 hours post-infection ($p<0.0001$, **Figure 10A**), all of which exhibited reduced viability at the highest MOI treatments (MOI 1 and 10). Viability at the MOI 10 treatment for each cell line was reduced to approximately 30%. No significant difference was found due to the main effect of cell line ($p=0.4748$). A panel of reduced MOI treatments was used to test the STOSE and MOE cell lines at 72 hours post-infection (**Figure 10B**); this was done after attempts at higher-MOI treatments yielded highly inconsistent results in these cells. Under these conditions, all four cell lines maintained full viability compared to the mock controls. As such, there was no main effect of

MOI (p=0.2314). The MOE *Pten*^{shRNA} *Trp53*^{R273H} achieved a small increase in viability at 10e^{-2} when compared to the MOE *Pten*^{shRNA} *KRas*^{G12V} cells under the same conditions (p=0.0310). Overall, however, statistical analysis determined no main effect of cell line (p=0.0776).

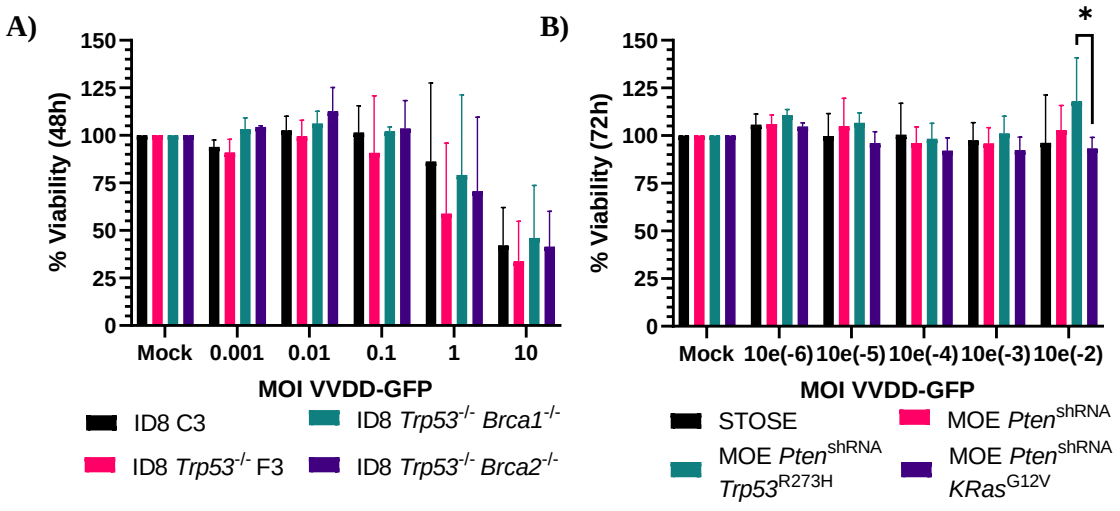

Figure 10: VVDD-GFP sensitivity of murine HGSC cell lines. *A) ID8 (48 hours), and B) STOSE and MOE cell lines (72 hours) were infected with VVDD-GFP at 10e^{-6} to 10e^{1} for 48-72 hours. After completion of the infection time, Alamar Blue assays were performed to measure cell viability. Viability for each cell line was normalized to the mock (MOI 0) sample. Analysis was done via two-way ANOVA followed by Tukey's post hoc test (n=3). Error bars depict SD. *p<0.05.*

Finally, all cell lines were screened for sensitivity to HSV-1-γ34.5. ID8 cells showed reduced viability at the two highest treatments, MOI 1 and 10, 72 hours after treatment (**Figure 11A**). ID8 cells achieved a maximum loss of viability at MOI 10, under which conditions the viability of all ID8 cells was reduced to 20-30% of the mock controls with no significant differences between cell lines. The ID8 C3 cells maintained higher viability than the ID8 *Trp53*$^{-/-}$ *Pten*$^{-/-}$ cells at MOI 0.1 (p=0.0076) and 1 (p=0.0314); these were the only two significant comparisons found within a single MOI treatment group. The interaction effect between cell line and MOI was non-significant (p=0.8919).

STOSE and MOE cells were again screened at lower treatment doses 72 hours post-infection (**Figure 11B**). No loss of viability was found for any cell line compared to the mock-treated controls at the lowest doses of HSV-1-γ34.5 tested. However, adding *Trp53*^{R273H} mutation to the MOE *Pten*^{shRNA} cells resulted in a significant loss of viability at MOI 10e^{-5} (p=0.0008) and 10e^{-4} (p=0.0019). This effect was also true for the addition of *KRas*^{G12V} mutation to the MOE *Pten*^{shRNA} cells at MOI 10e^{-4} (p=0.0235). The interaction effect between cell line and MOI was non-significant (p=0.1079).

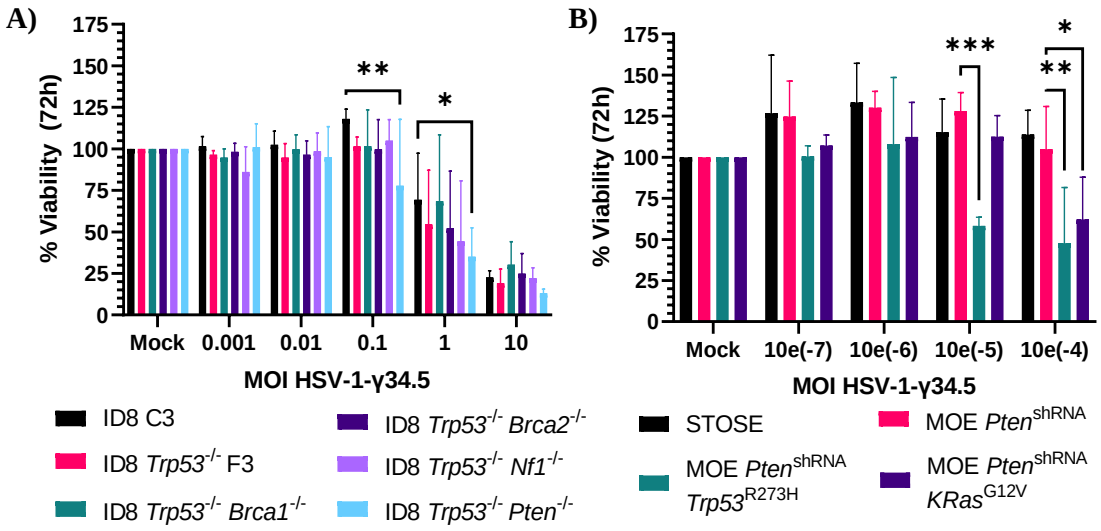

Figure 11: HSV-1-γ34.5 sensitivity of murine HGSC cell lines 72 hours after infection. *A) ID8, and B) STOSE and MOE cell lines were infected with VVDD-GFP at 10e^{-7} to 10e^{1} for 72 hours. After completion of the infection time, Alamar Blue assays were performed to measure cell viability. Viability for each cell line was normalized to the mock (MOI 0) sample. Analysis was done via two-way ANOVA followed by Tukey's post hoc test (n=3). Error bars depict SD. *p<0.05, **p<0.01, ***p<0.001.*

In summary, VSVΔM51 treatment of the ID8 cell lines yielded the most robust dose-dependent responses in the shortest among of time. Treatment with HSV-1-γ-34.5 and VVDD showed promise in the ID8 cell lines, with reduced viability present at the higher MOI treatments after prolonged infection. Due to limitations discussed in section 4.1.2, the compared sensitivity

of STOSE and MOE cells to the three OVs was determined inconclusive. Based on these findings, VSVΔM51 was selected as the primary OV of study for all subsequent experiments.

3.3 Characterization of VSVΔM51 Replication Kinetics in Murine HGSC Cell Lines

Comprehensive screening of viral replication kinetics in murine models of HGSC first required measurement of cell proliferation due to enhanced natural growth being a factor that could explain a higher capacity for viral replication. The confluence of all ID8, STOSE and MOE cell lines was measured using the Incucyte® Live-Cell Analysis system. All growth curves were normalized to start at ~25% confluence; in doing so, a higher mean confluence was indicative of faster growth. Cell confluence was measured in 2-hour increments until a fully confluent monolayer was achieved (up to 72 hours). The results for ID8, STOSE and MOE cells are presented below (**Figure 12**).

Analysis of ID8 growth revealed a significant effect of cell line ($p < 0.0001$) on the growth rate as determined by comparisons of mean confluence. However, limited biologically relevant differences were found among ID8 cells. Post-hoc analysis revealed significant differences ($p<0.0001$) between nearly all cell lines, with two exceptions. The ID8 *Trp53*$^{-/-}$ F3 and ID8 *Trp53*$^{-/-}$ *Brca2*$^{-/-}$ cells had equivalent mean confluences ($p = 0.9906$, 66.56% and 66.59%, respectively), which was only greater than that of the ID8 *Trp53*$^{-/-}$ *Brca1*$^{-/-}$ cells (64.63%). Conversely, the ID8 *Trp53*$^{-/-}$ *Nf1*$^{-/-}$ and ID8 *Trp53*$^{-/-}$ *Pten*$^{-/-}$ cells ($p = 0.0536$, 70.50% and 70.63%, respectively) had statistically equivalent mean confluences over time, which was minimally elevated compared to the ID8 C3 cells (69.67%) and higher than all other cell lines.

Analysis of STOSE and MOE cell growth rates revealed significantly different mean confluences between most lines ($p < 0.0001$ for each comparison) with one exception. The mean confluence of MOE *Pten*^{shRNA} and MOE *Pten*^{shRNA} *KRas*^{G12V} cells was equivalent ($p = 0.1450$).

The STOSE cells were the fastest growing line with the highest mean confluence (66.43%). Though double mutation of the MOE *Pten*^{shRNA} (59.51%) did not result in large increases in mean confluence, both the MOE *Pten*^{shRNA} *Trp53*^{R273H} (61.11%) and MOE *Pten*^{shRNA} *KRas*^{G12V} (60.22%) cells grew to full confluence while their parent cell line did not. This suggests a higher growth potential of the double mutant cells conferred by *Trp53*^{273H} or *KRas*^{G12V} mutation.

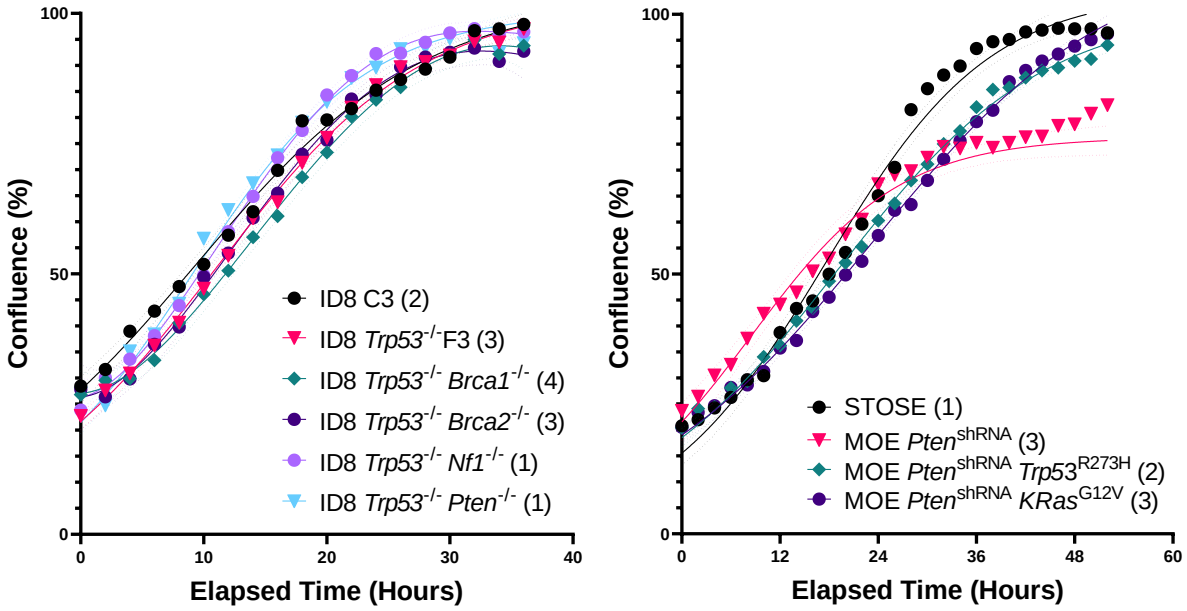

Figure 12: Proliferation rates of ID8, STOSE and MOE cells with specific genetic mutations. *Cell confluence was measured every two hours with the Incucyte® Live-Cell Analysis system. A logistics regression was fit to each cell line, and the 95% interval was calculated (shown by faint dotted lines). Analysis via one-way ANOVA and Tukey's post-hoc test to compare mean confluence (n=3 or 4). Rankings are given from 1 (highest mean confluence) to 4 (lowest mean confluence) in brackets for each cell line.*

Since cell lines were normalized to begin growth at statistically identical confluences (approximately 25%), differences in mean percent confluence indicated subtle changes in growth rates. In the case of the MOE *Pten*^{shRNA} cells, it is also important to also consider the growth to full confluence conferred by additional *Trp53*^{R273H} or *Kras*^{G12V} mutation.

Titering of supernatants collected from infected cell lines directly measured viral production. VSVΔM51-FLuc was used to infect ID8, STOSE and MOE cells at MOI 0.1, 1 and 10 for six hours, at which time supernatants were collected for titration via luminescence. No differences between ID8 cell lines were found within each MOI (**Figure 13A**, cell line main effect p=0.6761). As a group, the ID8 cells showed enhanced viral production by approximately 10-fold with each increased MOI treatment of VSVΔM51-FLuc (MOI main effect p<0.001). STOSE and MOE cells (**Figure 13B**) showed a similar main effect of MOI, with viral production increasing approximately 5-fold with each elevated treatment with VSVΔM51-FLuc (main effect p<0.0001). No significant differences among the cell lines in the quantity of virus produced was found at MOI 0.1 and 1. However, treatment at MOI 10 led to a 10-fold increase in virus production by the MOE *Pten*^{shRNA} *KRas*^{G12V} and STOSE cells compared to the MOE *Pten*^{shRNA} (p=0.004, and p=0.0053) and MOE *Pten*^{shRNA} *Trp53*^{R273H} cells (p=0.0001, and p=0.0021).

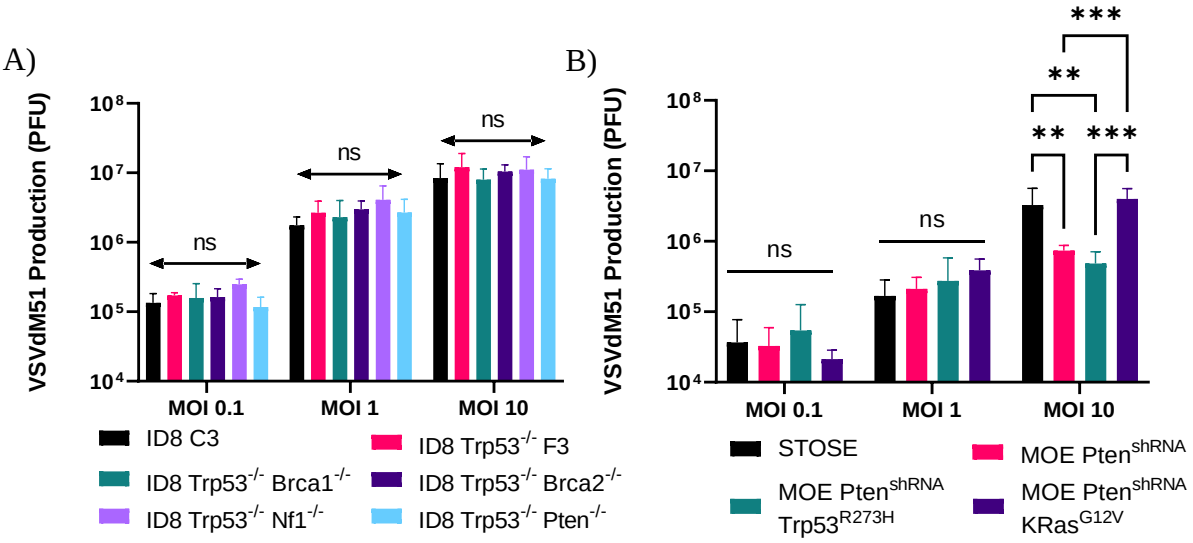

Figure 13: Replication of VSVΔM51 in ID8, STOSE and MOE cell lines. *Cell lines were infected with VSVΔM51 at MOI 0.1. After 6 hours of infection, cell supernatant was collected to quantify virus concentration via Luciferase titering on Vero cells. Analysis was done via two-way ANOVA with Tukey's post hoc test (n=3). *p<0.01, **p<0.01, ****p<0.0001.*

Images of VSVΔM51-GFP infected ID8 (**Figure 14**) and STOSE/MOE (**Figure 15**) cells via fluorescent microscopy. Confluent monolayers were treated with VSVΔM51-GFP at MOI 0 (mock), 0.1, 1 and 10 for 6 hours. GFP images showed infected cells, and a representative image of the confluent monolayer was taken via light microscopy.

All ID8 cells grew to similar monolayers of <95% confluence at the time of infection (**Figure 14**). Mock cells retained the normal "cobblestone" morphology during treatment and were free of VSVΔM51-GFP. Across treatment groups, all ID8 cells exhibit similar levels of infection. At the lowest treatment, MOI 0.1, few infected cells were visible that showed strong GFP signals. More infected cells were present at MOI 1, including those with lower levels of GFP expression. Finally, at the highest treatment at MOI 10, most cells in the monolayer had been infected and could be identified by the GFP signal. Morphological changes were consistent with VSV treatment though no evidence of mass cell death was present yet.

STOSE and MOE cells grew to confluent monolayers upon infection and control-treated samples retained normal morphology throughout treatment (**Figure 15**). No visibly infected cells were seen in the mock treatment. At MOI 0.1, a few MOE *Pten*^{shRNA} *Trp53*^{R273H} cells were easily identifiable, and a small number of MOE *Pten*^{shRNA} cells exhibited very low GFP signal. STOSE and MOE *Pten*^{shRNA} *KRas*^{G12V} cells showed no signs of infection. All cell lines showed visible infection and low GFP signal at MOI 0.1, though this was extremely subtle in the MOE *Pten*^{shRNA} *KRas*^{G12V} cells. At MOI 10, the majority of cells in each cell type are visibly infected with strong GFP signals; many cells also exhibit typical morphological changes associated with high VSVΔM51 treatment. The MOE *Pten*^{shRNA} *KRas*^{G12V} cells were most affected by these changes, as evident by their loss of confluence at MOI 10 and the sparser appearance of GFP-positive cells.

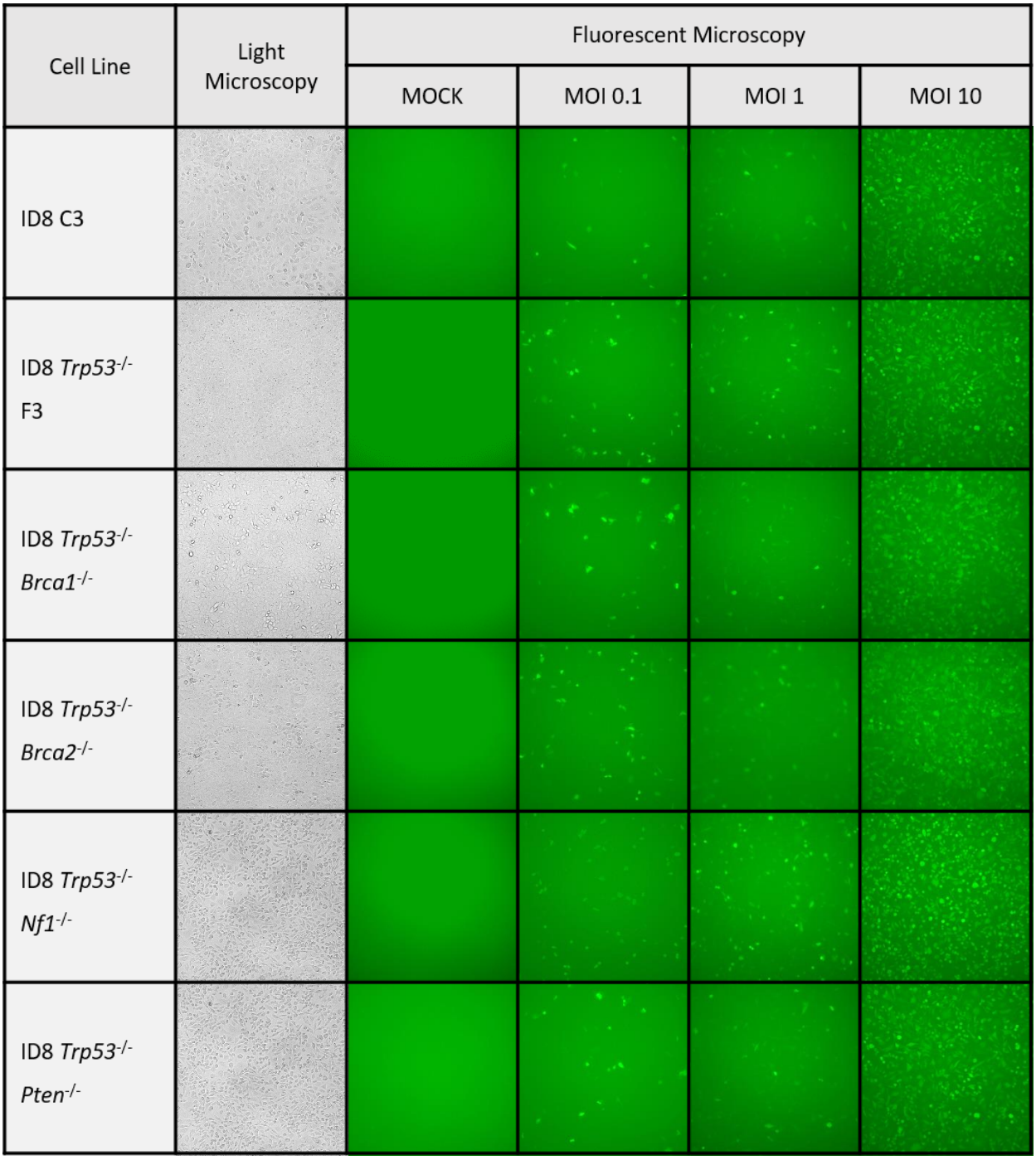

Figure 14: Microscopy of VSVΔM51-GFP infected ID8 cells. *ID8 cells were infected with VSVΔM51-GFP at an MOI of 0, 0.1, 1 and 10 for 6 hours. Images were captured at 100x. A representative image is shown of the cell monolayer captured with light microscopy. Fluorescence imaging captured the GFP produced by infected cell lines (n=1).*

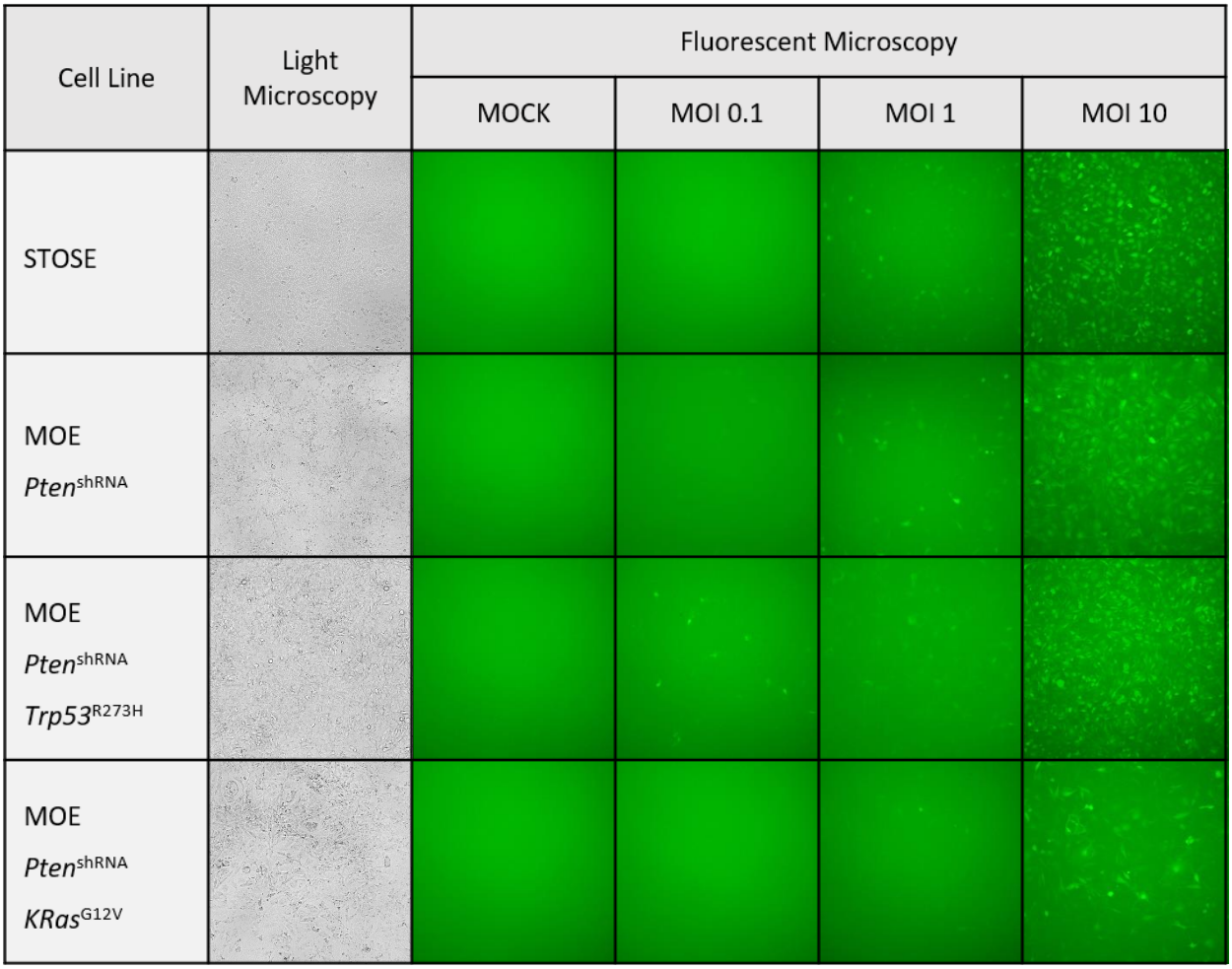

Figure 15: Microscopy of VSVΔM51-GFP infected STOES and MOE cells. *Cells were infected with VSVΔM51-GFP at an MOI of 0, 0.1, 1 and 10 for 6 hours. Images were captured at 100x. A representative image is shown of the cell monolayer captured with light microscopy. Fluorescence imaging captured the GFP produced by infected cell lines (n=1).*

In summary, VSVΔM51 was reproduced similarly in the ID8 cells despite various mutation combinations, which also showed similar growth rates. The addition of *Pten*^{R273H} and *KRas*^{G12V} mutations allowed MOE *Pten*^{shRNA} cells to grow to full confluence. Based on viral titers, *KRas*^{G12V} enhanced viral production. This finding was not apparent with fluorescent microscopy, where *Trp53*^{R273H} mutated MOE *Pten*^{shRNA} cells visually showed the highest amounts of intracellular VSVΔM51-GFP.

3.4 Analysis of Immunogenicity Changes post-VSVΔM51 Infection in Murine HGSC Cell Lines

Increases in immunogenic markers on tumour cells in response to VSVΔM51 infection are a contributing factor that help reverse immune suppression in the TME. Analysis of VSVΔM51-induced cell immunogenicity was first assessed using qPCR. This method evaluated the change in expression of key infection and immune markers after treatment with VSVΔM51-GFP (MOI 0.1) at three time points (0, 6 and 12 hours). The genes assessed were markers of antigen presentation capacity (B2M, H2K/Db or H2Kq) and inflammation induction (IFN-β and IFN-γ). The expression of the VSV receptor, LDLr, was also measured in untreated (0h) cells to determine if its level of expression might help to explain any differences in infectivity.

In ID8 cells, the main effect of treatment duration was highly significant for all genes tested ($p < 0.0001$, **Figure 16**). Expression of all antigen presentation genes (B2M, H2Kb and H2Db) was increased with a longer duration of VSVΔM51 infection. IFN-β levels increased substantially at 6h post-infection and remained consistently high at 12h post-infection. IFN-γ levels did not change from 0h to 6h post-treatment but increased slightly after 12h. Only a few significant differences between cell lines were found within a treatment group, indicating similar responses to treatment. At 12h post-infection, addition of *Nf1*$^{-/-}$ mutation increased H2Kb expression ($p = 0.0250$) and *Pten*$^{-/-}$ mutation increased H2Db expression ($p = 0.0047$), in comparison to the ID8 *Trp53*$^{-/-}$ cells. *Trp53*$^{-/-}$ mutation alone increased IFN-γ production compared to the control ID8 C3 cells. No significant differences in LDLr expression were found among any ID8 cell lines.

The response of STOSE and MOE cells to VSVΔM51 infection is shown in **Figure 17**. Across all genes tested, the main effect of treatment duration was significant, and no differences among cell lines were found at baseline (0h infection). B2M and H2Kq expression remained

overall unchanged 6h post-infection but dropped dramatically below baseline at 12h post-infection. MOE *Pten*^{shRNA} *Trp53*^{R273H} cells expressed significantly higher levels of B2M at the 6h time point. Otherwise, the expression of antigen presentation genes was consistent among cell lines. IFN-β production was strongly increased at 6h post-infection and remained relatively stable at 12h; notably, the *KRas*^{G12V} mutation decreased this induction when added to the MOE *Pten*^{shRNA} cells (p = 0.0174). IFN-γ expression was only elevated at 12h post-infection and was significantly higher in the MOE *Pten*^{shRNA} cells compared to all other cell lines. Importantly, LDLr expression was not different among STOSE and MOE cell lines.

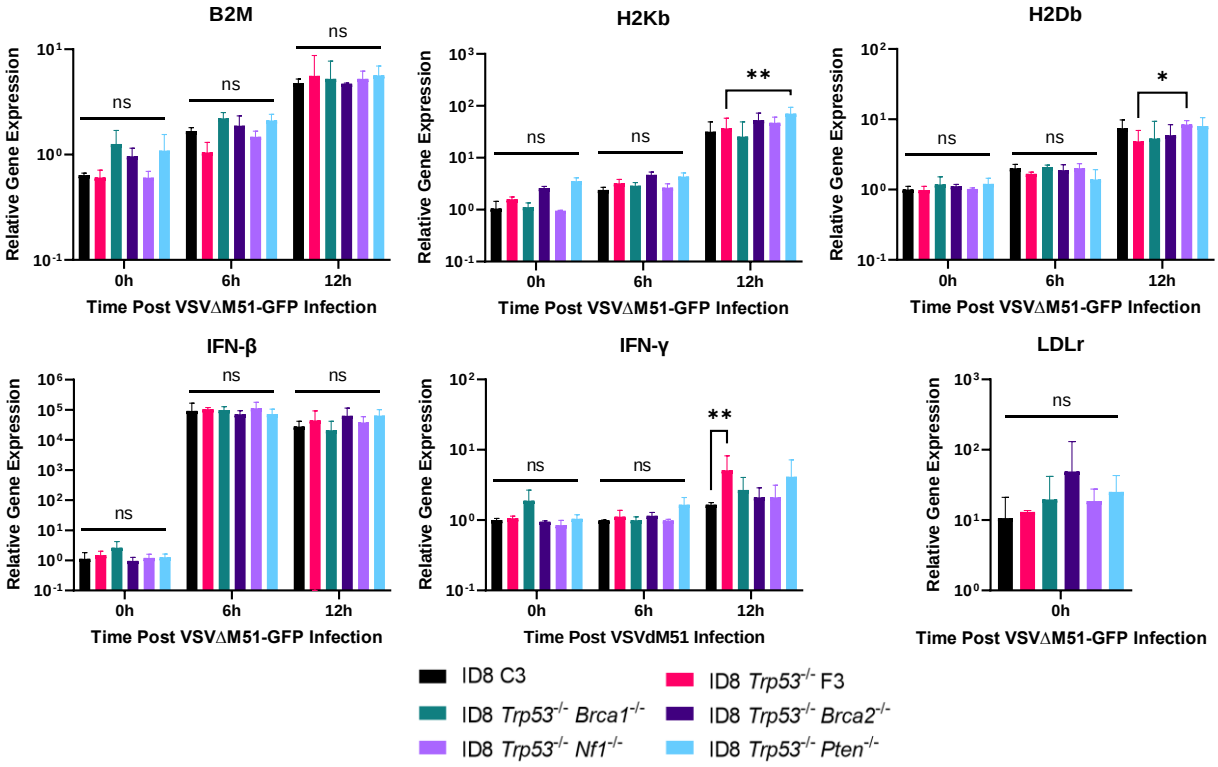

Figure 16: qPCR analysis of VSVΔM51 induced immunogenicity changes in ID8 cell lines. *ID8 cell lines with CRISPR-Cas9 induced mutations were infected with VSVΔM51-GFP for 0, 6 and 12 hours at MOI 0.1 and assessed via qPCR. Analysis of LDLr expression done via one-way ANOVA followed by a Dunnett's post-hoc test. All other gene expression levels were analyzed via two-way ANOVA followed by a Dunnett's post-hoc test (n=3). *p<0.05, **p<0.01.*

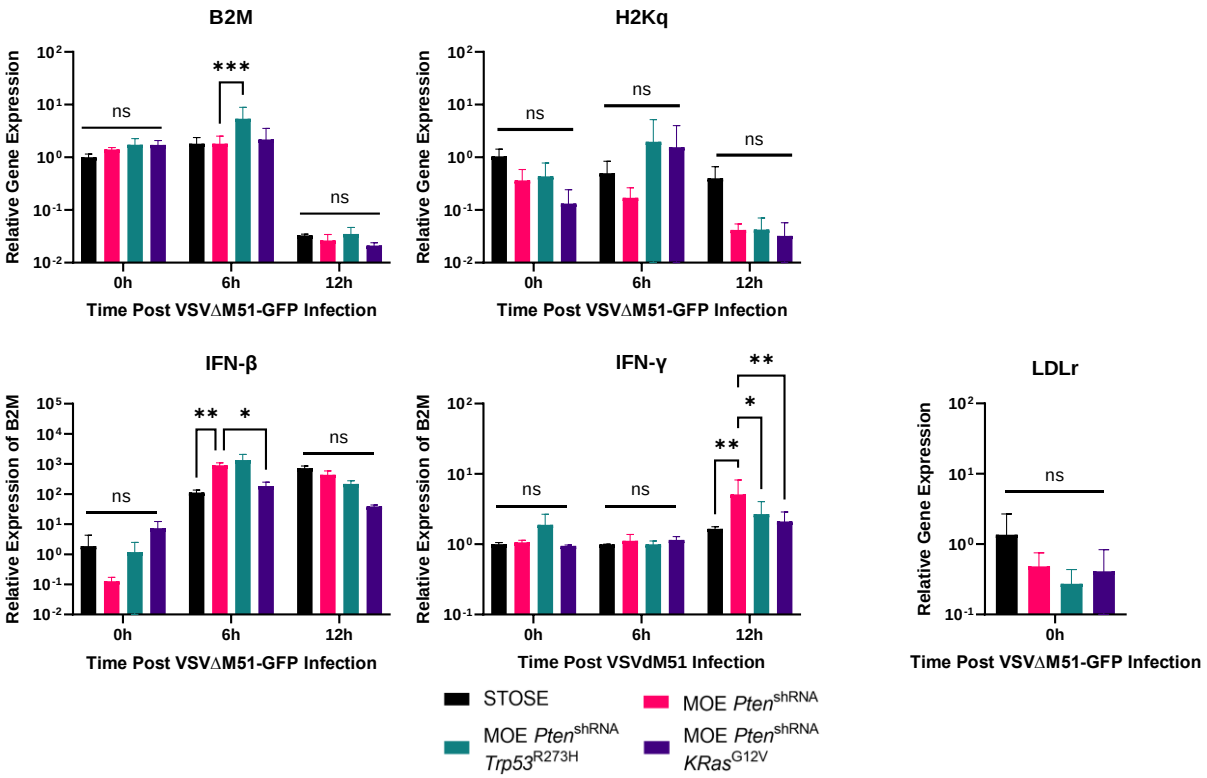

Figure 17: qPCR analysis of VSVΔM51 induced immunogenicity changes in STOSE and MOE cell lines. *STOSE and MOE cells with genetic mutations were infected with VSVΔM51-GFP for 0, 6 and 12 hours at MOI 0.1 and assessed via qPCR. Analysis of LDLr expression done via one-way ANOVA followed by a Dunnett's post-hoc test. All other gene expression levels were analyzed via two-way ANOVA followed by a Dunnett's post-hoc test (n=3). *p<0.05, **p<0.01, ***p<0.001.*

Flow cytometry was performed to analyze further the *in-vitro* response of ID8, STOSE and MOE cells to OV infection. The induction of key immunogenicity markers was measured after 6h of VSVΔM51-GFP treatment at multiple doses (MOI 0, 0.1, 1 and 10). These cells were collected and stained to assess MHC-I and PD-L1 presentation on the cell surface, in parallel to measuring GFP levels marking VSVΔM51 infection.

In the ID8 cells (**Figure 18**), the percent of GFP+ cells (i.e. VSVΔM51 infected) increased with MOI until nearly all cells were GFP+ at MOI 10. Significant differences among cell lines were only noted at MOI 10: ID8 Trp53-/- Nf1-/- cells expressed less GFP than their parental cell line, the ID8 *Trp53*$^{-/-}$ cells, as measured by MFI and % GFP+. All cell lines

increased PD-L1 with increasing doses of VSVΔM51; the ID8 C3 cells rose significantly higher in MFI than the rest of the group at MOI 1 and 10. MHC-1 expression by each cell line remained stable across treatments. However, consistent and significant differences among the cell lines were found. Most notably, adding *Brca1*$^{-/-}$ and *Pten*-/- mutations to the ID8 *Trp53*$^{-/-}$ cells repeatedly elevated the proportion of MHC-1+ cells and the MFI of expression.

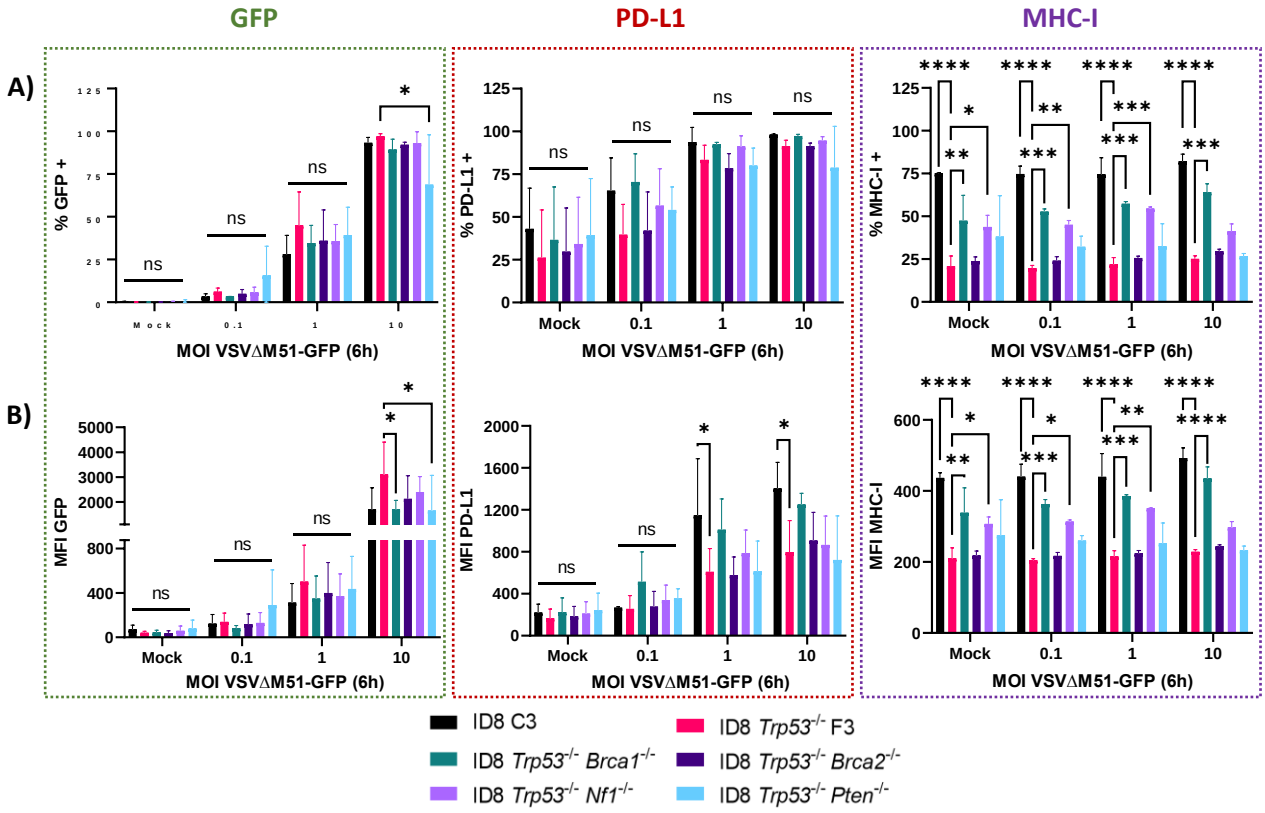

Figure 18: Flow cytometry analysis of VSVΔM51 induced immunogenicity changes in ID8 cell lines. *ID8 cell lines with CRISPR-Cas9 induced mutations were infected with VSVΔM51-GFP for 6 hours at MOI 0, 0.1, 1 and 10. Cells were stained using murine PD-L1, and H2-K/Db targeting antibodies conjugated to fluorophores and analyzed via flow cytometry. Measurements include A) the % of total cells expressing each protein and B) the mean fluorescence intensity (MFI) of each protein in the samples. Analysis done via two-way ANOVA followed by a Dunnett's post-hoc test (n=3). *p<0.05, **p<0.01, ***p<0.001, ****p<0.0001.*

In STOSE and MOE cells (**Figure 19**), GFP expression is minimally induced at MOI 0.1 and 1, and strongly induced at MOI 10. Of note, addition of *KRas*^{G21V} mutation reduced the expression of GFP in the MOE *Pten*^{shRNA} *KRas*^{G12V} cells (MFI and % GFP+ $p < 0.0001$). PD-L1 expression was increased in all cell lines with higher MOI treatments and was found overall consistent among cell lines. Nearly 100% of STOSE and MOE populations expressed MHC-1 across all treatments. However, analysis of MFI reveals a higher intensity of MHC-I expression in STOSE cells ($p<0.01$), and a much lower, but consistent level of expression in MOE cells.

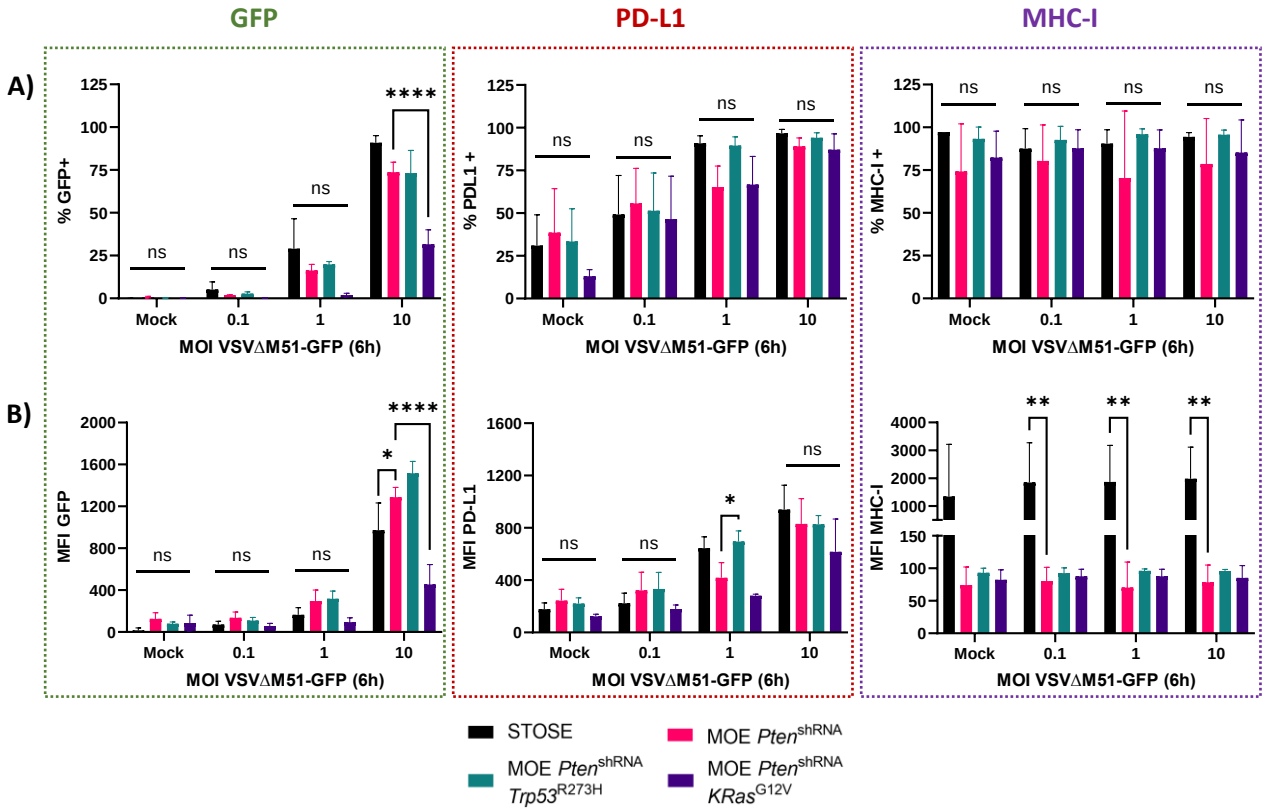

Figure 19: Flow cytometry analysis of VSVΔM51 induced immunogenicity changes in STOSE and MOE cell lines. *STOSE and MOE cell lines with specific genetic mutations were infected with VSVΔM51-GFP for 6 hours at MOI 0, 0.1, 1 and 10. Cells were stained using murine PD-L1 and H2-K/Db targeting antibodies conjugated to fluorophores and analyzed via flow cytometry. Measurements include A) the % of total cells expressing each protein and B) the mean fluorescence intensity (MFI) of each protein with the samples. Analysis done via two-way ANOVA followed by a Dunnett's post-hoc test (n=3). *p<0.05, **p<0.01, ****p<0.0001.*

The above results suggest an overall response VSVΔM51 associated with increases in tumour immunogenicity. These changes were most strongly noted in the ID8 cells, in comparison to the STOSE and MOE cells.

3.5 Survival Benefit of Carboplatin and VSVΔM51 Treatments in Syngeneic HGSC Murine Models

Syngeneic *in-vivo* models provide means to assess survival responses to carboplatin or OV therapy with a functional immune system present. Two independent studies were conducted to evaluate the survival benefit of each treatment administered as a monotherapy in syngeneic murine models of HGSC with specific genetic mutations and unique TMEs. Tumours were established via IP injection, and three doses of carboplatin (1 week apart) or VSVΔM51 (3 days apart) were also given via IP injection starting at 25% of the expected duration of survival of control (untreated) mice.

The survival of mice receiving carboplatin treatment or saline control is shown in **Figure 20**. Carboplatin did not significantly prolong survival in four of the five models tested: the ID8 C3 ($p = 0.6267$), ID8 *Trp53*$^{-/-}$ F3 ($p = 0.3577$), STOSE ($p = 0.07846$), and MOE *Pten*^{shRNA} *Trp53*^{G12V} ($p = 0.2038$). The survival of MOE *Pten*^{shRNA} *KRas*^{G21V} tumour-bearing mice was significantly, albeit modestly, prolonged by treatment ($p = 0.0024$); the difference between median survival of the saline control and carboplatin-treated mice was 6 days. Necropsy at the endpoint measured differences in spleen weight, ascites volume, and tumour weight between saline-control and carboplatin treated mice. These data sets did not show any consistent trends, and most comparisons between treatment groups were insignificant. The necropsy data are presented in the appendix (**Section 5.2**).

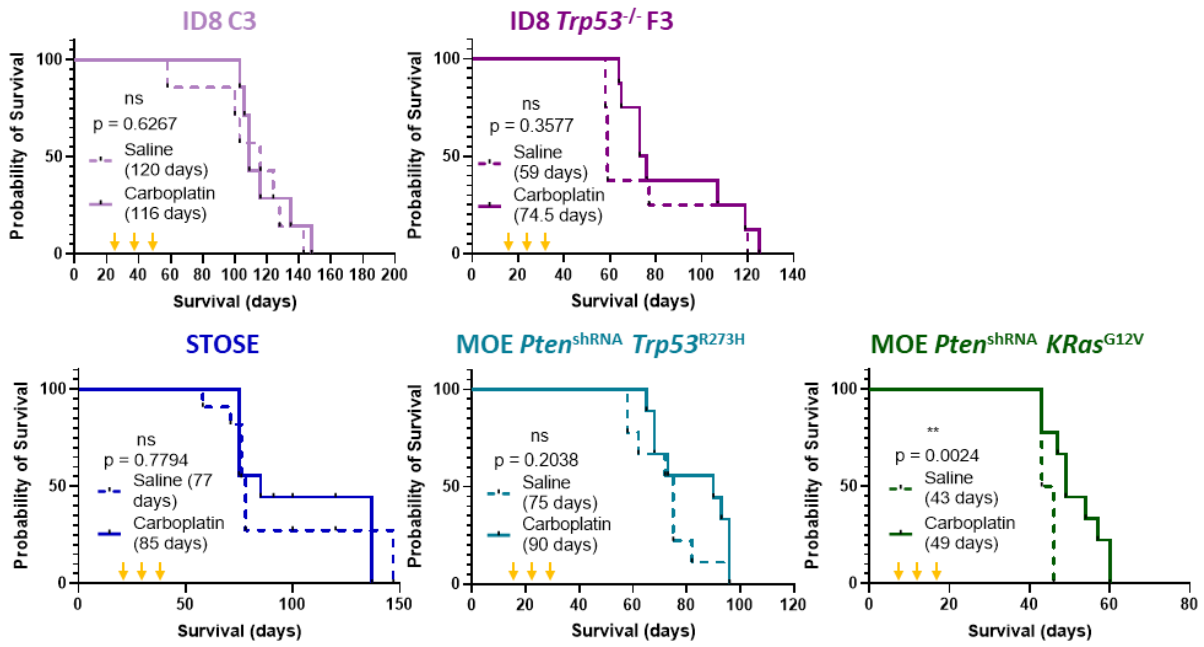

Figure 20: Survival of ID8, STOSE and MOE syngeneic tumour-bearing mice after carboplatin treatment. *Mice (n=20 per model) received 5e^6 tumour cells via intraperitoneal injection. Three doses of 12.5mg/kg of carboplatin (n=10 per model) or saline control (n=10 per model) were given one week apart (noted by yellow arrows), beginning at 25% of the expected survival time for that model. All mice were euthanized at humane endpoint. Analysis done via Mantle-Cox Log-Rank Test. **p<0.01.*

The assessment of survival benefit conferred by VSVΔM51 treatment included the same five models described above, in addition to mice bearing ID8 *Trp53*$^{-/-}$ *Brca2*$^{-/-}$ tumours (**Figure 21**). Half of these models were found non-responsive to VSVΔM51: the ID8 C3 (p = 0.8091), ID8 *Trp53*$^{-/-}$ F3 (p = 0.0981) and STOSE (p = 0.0786). VSVΔM51 treatment was able to prolong survival in the three remaining models: ID8 *Trp53*$^{-/-}$ *Brca2*$^{-/-}$ (p < 0.0001, median survival extended by 14 days), MOE *Pten*^{shRNA} *Trp53*^{R273H} (p = 0.0013, median survival extended by 15 days) and MOE *Pten*^{shRNA} *KRas*^{G12V} (p = 0.0191, median survival extended by 28 days). As with carboplatin treatment, the necropsy statistics of VSVΔM51 study mice did not yield consistent trends, and comparisons were typically insignificant. The necropsy also yielded few significant findings and are presented in the appendix (**section 5.2**).

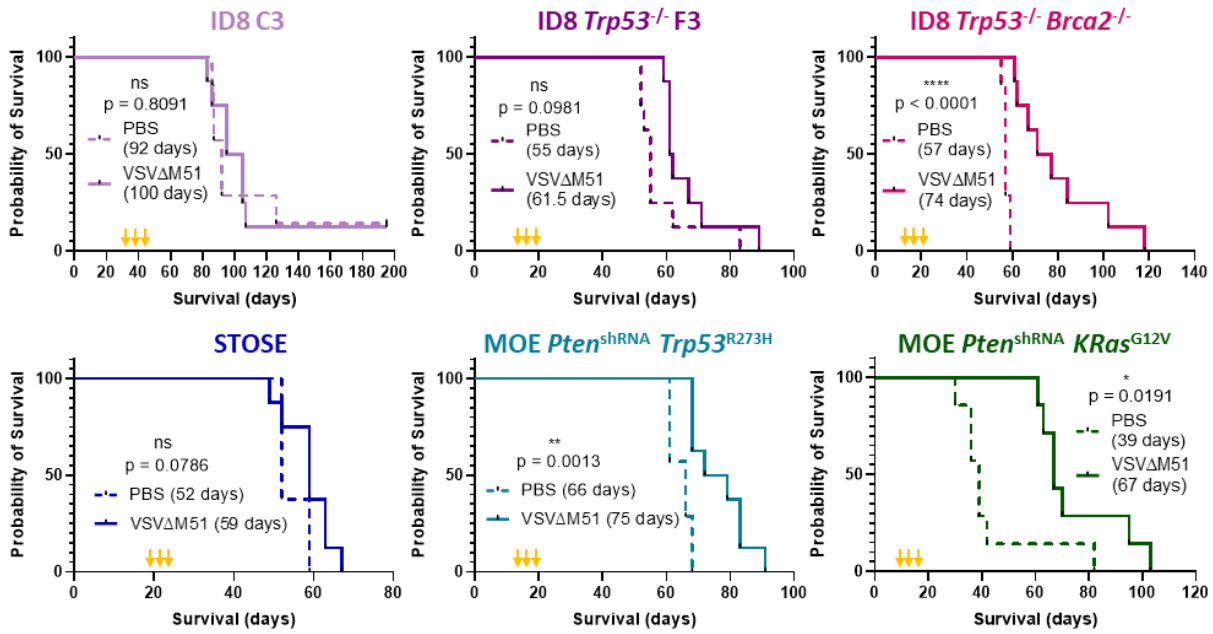

Figure 21: Survival of ID8, STOSE and MOE syngeneic tumour bearing mice after VSVΔM51 treatment. *Mice (n=16 per model) received $5e^6$ tumour cells via intraperitoneal injection. Three doses of $3e^8$PFU of VSVΔM51 (n=8 per model) or PBS control (n=8 per model) were given three days apart beginning at 25% of the expected survival time for that model (noted by yellow arrows). Mice were euthanized at humane endpoint. Analysis done via Mantle-Cox Log-Rank Test.*p<0.01, **p<0.01, ****p<0.0001.*

These syngeneic models have shown the ability of VSVΔM51 to prolong survival in three models, one of which was found unresponsive to carboplatin treatment. The specific immune changes in the TME of responsive models conferring this survival benefit was evaluated next.

3.6 Characterization of TME Immune Landscape in VSVΔM51 Responsive Syngeneic Models

Characterization of the TME in VSVΔM51 sensitive tumour models has the potential to provide insight into the immune response that favour treatment success. Survival was prolonged by VSVΔM51 treatment in MOE *Pten*^{shRNA} *Trp53*^{R273H}, MOE *Pten*^{shRNA} *KRas*^{G12V} and ID8 *Trp53*$^{-/-}$ *Brca2*$^{-/-}$ tumour bearing mice, as shown in **section 3.5**; the latter two models were selected for further study. The immune activity of the TME can be evident within the immediate

tumour sites (modelled by peritoneal wash to mimic the ascites TME) and at distant immune hubs (ex. the spleen and mLN).

The syngeneic models bearing MOE *Pten*^{shRNA} *KRas*^{G12V} and ID8 *Trp53*$^{-/-}$ *Brca2*$^{-/-}$ tumours were repeated and treated with VSVΔM51 as described above. Five days after the final treatment dose, mice were euthanized to collect relevant tissues and to perform immune analysis via flow cytometry. The proportional distribution of leukocyte populations within the three tissue types collected is shown in **Figure 22**.

In the ID8 *Trp53*$^{-/-}$ *Brca2*$^{-/-}$ model, VSVΔM51 treatment increased the CD8+ T cell presence in the peritoneal wash ($p < 0.0001$) but these cells were decreased in the mLNs ($p = 0.0136$). CD4+ T cells were favoured in the spleen ($p < 0.0001$) after treatment. VSVΔM51 led to a decrease of cDC-2 cells in both peritoneal wash ($p = 0.0215$) and mLN ($p = 0.0015$) samples. No other significant differences were found in the distant immune hub samples. However, NK cells and TAMs were decreased in the peritoneal wash ($p = 0.0007$ and $p = 0.0046$, respectively).

VSVΔM51 treatment of MOE *Pten*^{shRNA} *KRas*^{G12V} gave rise to fewer significant changes in the immune profile of each tissue sample. In the peritoneal wash, an increase in CD4+ T cells ($p < 0.0001$) and a decrease in NK cells ($p < 0.0001$) was noted due to treatment. The CD8+ T cell population was slightly, but significantly, decreased in the spleen samples. No other differences were found between PBS and VSVΔM51 treated samples in this model across all three tissue types.

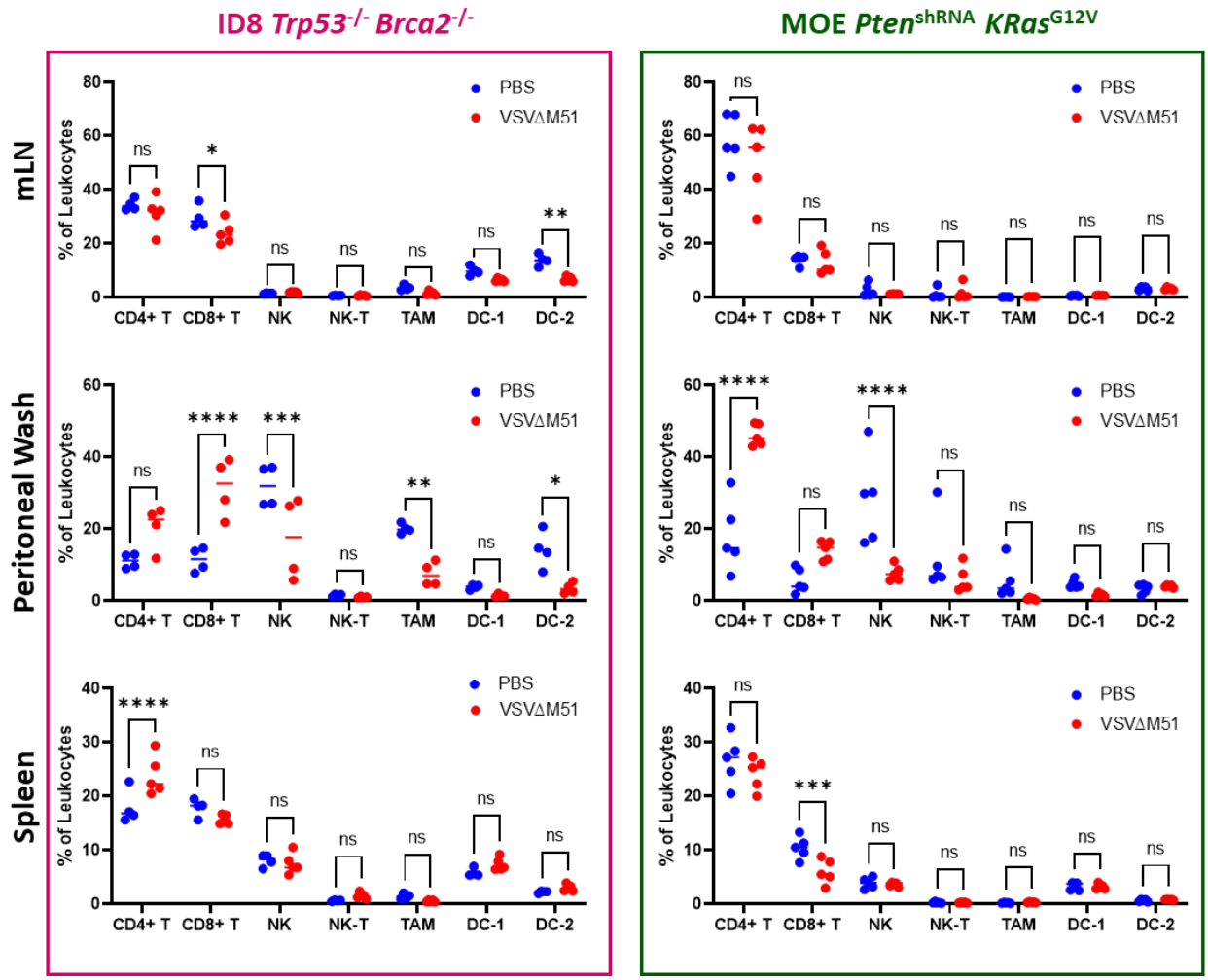

Figure 22: Percent of leukocytes within the TME and distant immune hubs of ID8 Trp53$^{-/-}$ Brca2$^{-/-}$ and MOE Pten^{shRNA} KRas^{G12V} tumours treated with VSVΔM51. *Mice bearing syngeneic IP tumours were treated with 3 doses of PBS (n=5 per model) or VSVΔM51 (n=5 per model). Five days after the final treatment, the mesenteric lymph nodes (mLN), peritoneal wash and spleen samples were collected for analysis via flow cytometry to identify proportion of immune cell populations. Total population of leukocytes is defined as CD45+ live cells. *p<0.05, **p<0.01, ***p<0.001, ****p<0.0001.*

A more comprehensive analysis of immune cell activation was conducted within all three sample types: the spleen, mLN and peritoneal wash. In both the ID8 *Trp53*$^{-/-}$ *Brca2*$^{-/-}$ and MOE *Pten*^{shRNA} *KRas*^{G12V} mice, VSVΔM51 treatment led to few significant differences in the distant immune hubs compared to PBS control treatment. As such, results for these tissue samples are shown in the Appendix (**section 5.3**).

Analyses of lymphocyte and myeloid immune populations within the peritoneal wash are shown below. Lymphocyte cells analyzed included CD4+ T cells, CD8+ T cells, and NK cells (**Figure 23**). Upon VSVΔM51 treatment, fewer CD4+ T cells expressed CD25 (MOE only, $p = 0.0043$) and MFI was decreased (ID8 $p = 0.0078$, MOE $p = 0.0208$) on this cell type. CD25 expression was unchanged by treatment in CD8+ T cell and NK cell populations in both models. Treatment with VSVΔM51 did not alter LAG3 expression in CD4+ and CD8+ T cell populations; this finding was consistent across both ID8 and MOE models. However, expression of LAG3 was more frequently expressed among ID8 *Trp53*$^{-/-}$ *Brca2*$^{-/-}$ NK cells treated with VSV ($p = 0.0022$) and expressed at lower levels in the MOE *Pten*^{shRNA} *KRas*^{G12V} NK cells ($p = 0.0034$). In both models, VSVΔM51 significantly increased PD-1 in CD4+ and CD8+ T cells, but not NK cells. Expression of two NK cell specific markers, NKp45 and NKG2D, did not change in response to VSVΔM51 treatment in both models.

Analysis of myeloid cells included TAMS, cDC-1 cells, and cDC-2 cells, three populations which all function in MHC-II antigen presentation (**Figure 24**). In the MOE *Pten*^{shRNA} *KRas*^{G12V} model, PD-L1 MFI was significantly increased in macrophages and DC-2 cells; no change in MFI was found in ID8 *Trp53*$^{-/-}$ *Brca2*$^{-/-}$ samples. Fewer ID8 derived DC-1 cells expressed PD-L1 after VSVΔM51 treatment ($p < 0.0001$), with no change noted between treatment groups in other cell types or within the MOE model. VSVΔM51 treatment had an inconsistent effect on the MHC-II and CD86 expression of macrophages and DC-2 cells. In most cases, MHC-II expression was decreased; this finding was associated with no change or a decrease in CD86 expression on the same cell type.

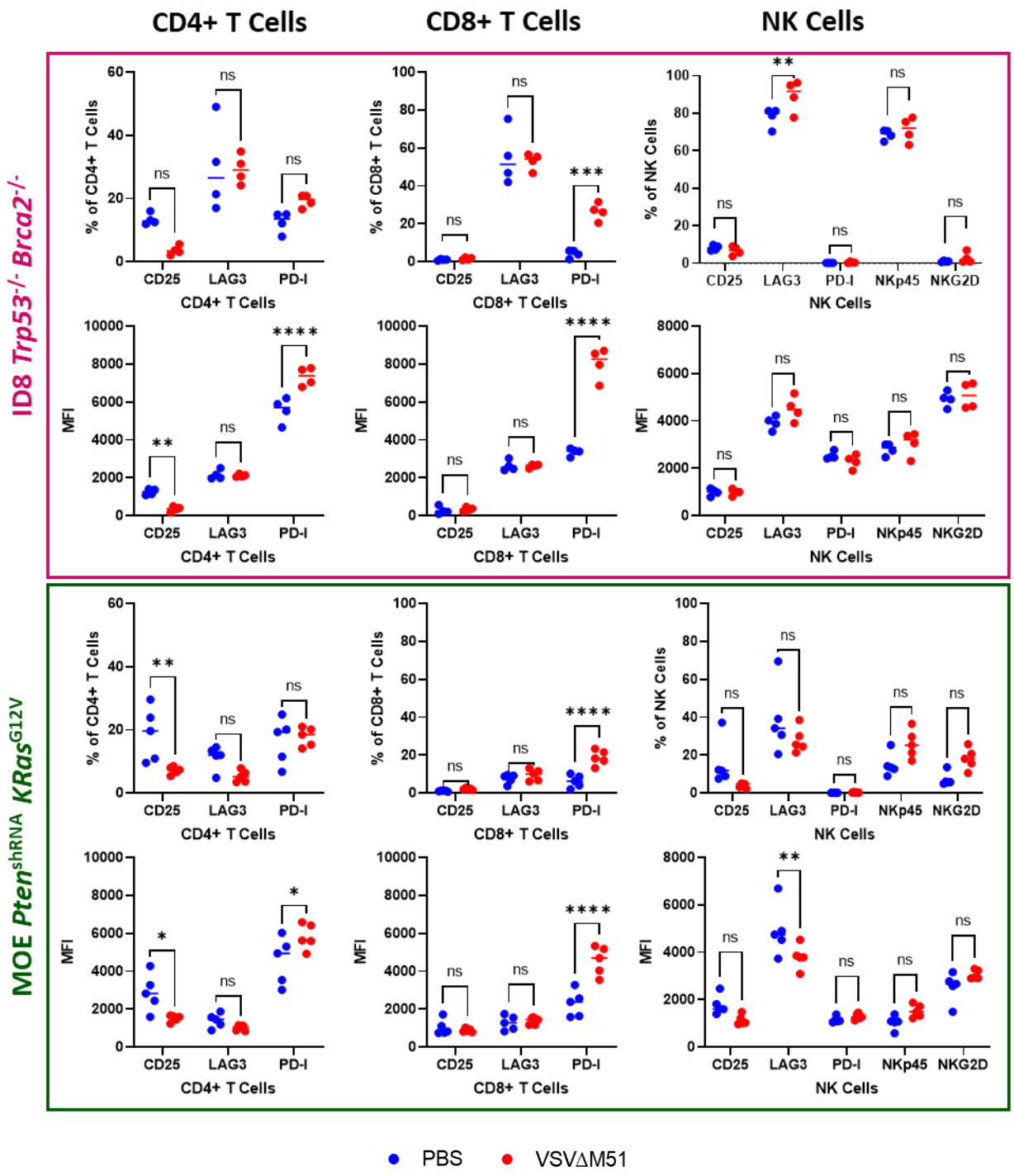

Figure 23: Activation markers of lymphocyte immune cells collected from peritoneal wash of tumour bearing mice treated with VSVΔM51. *CD4+ T cells, CD8+ T cells and NK cells were collected from the peritoneal wash of ID8 Trp53$^{-/-}$ Brca2$^{-/-}$ and MOE PTEN^{shRNA} KRas^{G12V} mice, previously treated with PBS or VSVΔM51. Flow cytometry analysis of activation markers CD25, LAG3 and PD-1 was performed. *p<0.05, **p<0.01, ****p<0.0001.*

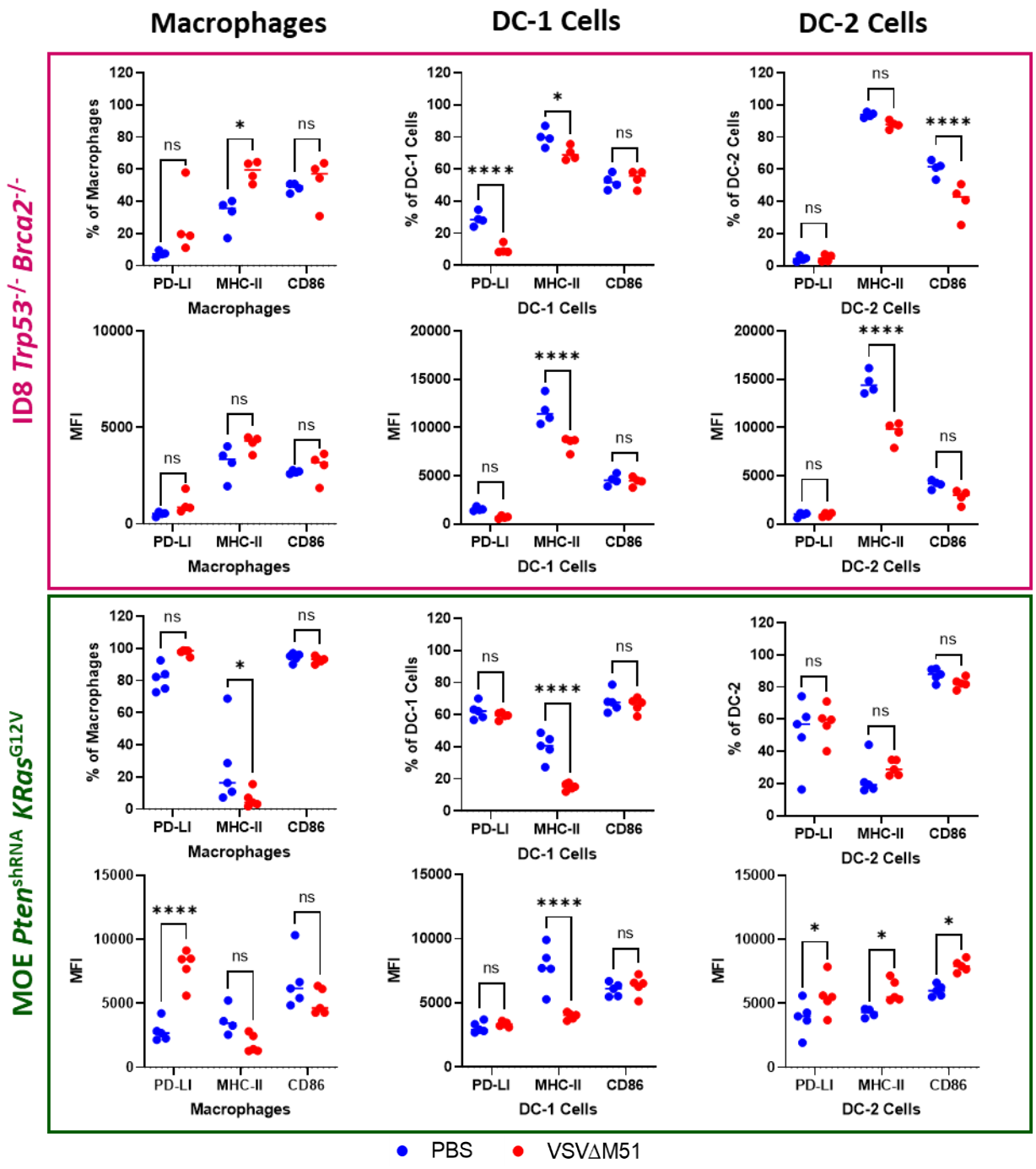

Figure 24: Activation markers of myeloid immune cells collected from peritoneal wash of tumour bearing mice treated with VSVΔM51. *Macrophages, DC-1 cells, and DC-2 cells were collected from the peritoneal wash of ID8 Trp53$^{-/-}$ Brca2$^{-/-}$ and MOE PTEN^{shRNA} KRas^{G12V} mice, previously treated with PBS or VSVΔM51. Flow cytometry analysis of PD-L1, MHC-II and CD86 was performed on each cell type. *p<0.05, ****p<0.0001.*

Chapter 4: Discussion

4.1 In-Vitro Experiments

The *in-vitro* experiments completed during this project provide a foundational assessment of carboplatin and VSVΔM51 sensitivity in murine HGSC models with specific genetic mutations. Assessment *in-vitro* uncovered important findings to help explain differences in VSVΔM51 sensitivity and support later *in-vivo* results. These pieces of *in-vitro* data first require independent discussion before the results can be considered a strong support of later *in-vivo* findings.

4.1.1 Sensitivity of In-Vitro Murine HGSC Cell Lines to Carboplatin Treatment

Initial testing of carboplatin sensitivity provided a baseline assessment of cell responsiveness to the current standard of care. Loss of Trp53 function in the ID8 C3 cells enhanced loss of viability in response to carboplatin treatment (defined here as an increased sensitivity); the same effect was found in MOE *Pten*^{shRNA} cells due to oncomorphic stabilization of Trp53 (**Figure 8**). In both cases, aberration of WT Trp53 function enhanced carboplatin sensitivity, a result that is not commonly seen in the scientific literature.

Analysis of human HGSC outcomes has shown aberrations in *TP53* – primarily due to gain of function mutations – are commonly associated with platinum-based chemotherapy resistance[59,106–108]. Oncomorphic gain of function Trp53 mutations enhance chemo-resistance by activating multiple growth pathways and preventing apoptosis induction (ex. via caspase downregulation or disfavouring ROS production)[58,60,108]. The evidence relating loss of TP53 function to chemosensitivity is less consistent. WT TP53 stimulates many pro-apoptotic genes including Bid, Bax/Bak, and Fas[109]. Thus, the loss of WT TP53 function is typically associated with poor apoptosis induction and chemo-resistance. However, evidence exists that tumours with

loss of TP53 function are less chemo-resistant than those harbouring oncomorphic TP53; in one pre-clinical model of human HGSC, increased sensitivity to platinum-based chemotherapies was found when TP53 function was lost in the A2780 cell line[107,110].

These previous findings on P53 function are inconsistent with the results of this project, where both loss of function and oncomorphic *Trp53* mutations enhanced carboplatin sensitivity in mouse HGSC cell models *in-vitro.* These inconsistencies require further investigation to be fully understood. In this endeavour, analysis of the specific apoptotic pathways activated by carboplatin may provide mechanisms by which the *Trp53* mutations in question fail to confer resistance. Another potential pathway of study is the upregulation of glutamine metabolism, which is common amongst aggressive tumour types and in OC has been associated with resistance to platinum-based chemotherapy[111,112]. Comparison of glutamine consumption and use in carboplatin-sensitive and -resistant cells found here may provide insight into the mechanisms underlying deviation of the Trp53 mutant cells from common literature findings.

The most carboplatin-sensitive cell lines harboured a loss-of-function *Brca1* or *Brca2* mutation. This finding was very much expected since the inability of *Brca1/2* mutated cells to repair dsDNA breaks renders cells highly vulnerable to DNA damage, as induced by carboplatin[23]. Patients with tumours that harbour these mutations are known to be more responsive to chemotherapy[24,113]. Previous studies have also shown ID8 *Trp53*$^{-/-}$ *Brca1*$^{-/-}$ and ID8 *Trp53*$^{-/-}$ *Brca2*$^{-/-}$ cells to be more carboplatin sensitive than their parental line, the ID8 *Trp53*$^{-/-}$ F3 cells[69,70]. Unfortunately, the ID8 *Trp53*$^{-/-}$ *Nf1*$^{-/-}$ and ID8 *Trp53*$^{-/-}$ *Pten*$^{-/-}$ cell lines were not available for the carboplatin screening. Previous studies have shown both *Nf1*$^{-/-}$ and *Pten*$^{-/-}$ are ineffective at increasing chemotherapy sensitivity of the ID8 *Trp53*$^{-/-}$ F3 cells[70].

4.1.2 Sensitivity of In-Vitro Murine HGSC Cell Lines to Oncolytic Virus Treatment

All cell lines tested responded to VSVΔM51 treatment *in-vitro* with a loss of viability as determined by the Alamar Blue assay (**Figure 9**). ID8 *Trp53*-/- *Nf1*-/- cells were slightly more resistant to high MOI treatments than the ID8 C3 control, though this result was not repeated in further experiments conducted within the scope of this project. A near complete loss of viability was achieved by all ID8 cells 48 hours post-infection, indicating a high susceptibility to VSVΔM51 treatment. In comparison, STOSE and MOE cells responded to VSVΔM51 less uniformly and with more resistance to loss of viability.

In response to multiple MOI treatments, MOE *Pten*^{shRNA} *Trp53*^{R273H} cells were more resistant to VSVΔM51 treatment than the MOE *Pten*^{shRNA} and MOE *Pten*^{shRNA} *KRas*^{G12V} cells. This agrees with previous work showing that VSV is effective against tumours with TP53 pathway mutations and that KRAS overactivity can orchestrate defective IFN-mediated responses to infection, thus paving the way for enhanced VSV-mediated cell death[96,114].

VVDD (**Figure 10**) and HSV-1-γ34.5 (**Figure 11**) sensitivity was also measured in the ID8, STOSE and MOE cell lines. A viability reduction was noted in the ID8 cells at the two highest MOI doses (MOI 1 and 10) after 48h or 72h of treatment. Overall, higher doses of both viruses and longer incubation times were required to achieve a similar loss of viability in the ID8 cells, in comparison to results achieved with VSVΔM51 treatment. The sensitivity of MOE and STOSE cells with both dsDNA viruses was tested using reduced MOI treatments, which did not show strong efficacy. Furthermore, these lower MOI treatments were extremely limited by the small 96-well screening format that resulted in minimal to no infection of cells. Strong conclusions could not be made regarding the sensitivity of STOSE/MOE cells to VVDD and HSV-1-γ34.5 as a result. This limitation should be addressed by utilizing the same MOI dosing

range that was applied to other cell lines (MOI 0.001 to 10) and/or increasing well size to allow for sufficient infection at low MOI's.

It should be noted that the use of multiple MOI treatments was employed for screening of OV sensitivity instead of calculating an IC50 value, which was used to assess cell sensitivity to carboplatin. This decision was made firstly to enhance relevance to the literature, where standard MOIs (ex. MOI 0.1 and 10) are commonly used as treatment doses in diverse *in-vitro* models. Secondly, the use of multiple MOIs shows the breadth of the range of sensitivity for each cell line to the OVs, whereas IC50 lacks interpretation for the size of this window of opportunity. However, the use of multiple MOIs instead of IC50 is limited because it does not generate a standardized treatment dose for each cell line at which identical efficacy is seen.

Based on these results, VSVΔM51 was determined as the most efficacious OV in the ID8 cell lines, where a shorter 24 timepoint was sufficient to reduce cell viability regardless of mutation status and with relatively low MOI treatment doses required. The remaining experiments were thus conducted using only VSVΔM51. However, there is still believed to be therapeutic potential of VVDD and HSV-1 that is worthy of investigation in murine HGSC models, if the limitations presented here for these viruses can be addressed. Both viruses have shown efficacy in *in-vitro* models of human and murine OC tumours by other studies[78,87,90].

4.1.3 Cell Kinetics Enhancing VSVΔM51 Replication

The high proliferation rates typical to HGSC tumours create favourable conditions for OV replication, as reviewed in **Section 1.3.1**. Rapid replication may provide a foundation for improved OV sensitivity and many genetic mutations studied in this project stimulate various growth pathways. As such, it was essential to compare baseline proliferation of all cell lines.

The ID8 cells exhibited similar growth rates, though many significant differences were found between mean confluences. *Nf1*$^{-/-}$ and *Pten*$^{-/-}$ mutations in the ID8 *Trp53*$^{-/-}$ cells resulted in the fastest growth, consistent with their effects of released inhibition on the RAS and PI3K growth pathways[63,68]. The slowest growth belonged to the ID8 *Trp53*$^{-/-}$, ID8 *Trp53*$^{-/-}$ *Brca1*$^{-/-}$ and ID8 *Trp53*$^{-/-}$ *Brca2*$^{-/-}$ cell lines. This finding was not unexpected, as we have previously shown that the inactivation of *Brca1* in OSE cells suppresses cell proliferation[115]. These subtle differences in ID8 replication, as determined by mean confluence, are likely biologically irrelevant for VSVΔM51 growth: few mutation-associated differences in virus output were found upon further *in-vitro* study.

Of the four FVB/N-derived models tested, the STOSE exhibited the fastest growth rate as indicated by the highest mean confluence; this was expected and noticeable when completing *in-vitro* experiments. Previous studies have measured the doubling time for STOSE cells as 13 hours, similar to the growth rate measured here[13]. An initial study of the MOE cell lines by Eddie et al. showed that *Pten*^{shRNA} mutation alone is sufficient to increase proliferation rate compared to parental, unmutated MOE cells; this result was minimally enhanced by additional *KRas*^{G12V} or *Trp53*^{273H} mutations[19]. In the present project, the mean confluence of single-mutated MOE *Pten*^{shRNA} cells was similar to that of both double mutant lines. However, the addition of *KRas*^{G12V} or *Trp53*^{273H} allowed the cells to grow to full confluence, whereas the parental line did not.

It should be noted that growth was measured and compared based on mean confluence over a set window of time, which was a departure from the commonly used measurement of doubling time. Statistical comparison of mean confluence enhanced ability to uncover subtle differences between cell growth patterns by better accounting for unique cell growth patterns.

For instance, doubling time did not optimally account for the inability of some cell lines to achieve full confluence or the inconsistent growth between early and late growth phases (both especially prevalent in the MOE *Pten*^{shRNA} cells). Measuring mean confluence of all cell lines improved upon these issues by giving an average assessment of growth that was inclusive of both factors. Despite this advantage, mean confluence generates a relative value that cannot be interpreted outside the context of the present experiments, whereas doubling time could be compared easily to other studies.

The comparison of VSVΔM51 replication capacity supported the conclusion that ID8, STOSE and MOE are all susceptible to VSVΔM51; VSV titers increased dramatically in all cell lines with higher MOI of treatment. No significant differences between the ID8 cell lines were found, consistent with their similar replication rates and suggesting that the specific gene mutations are insufficient to influence viral replication in the ID8 model *in-vitro*. In support of this finding, ID8 cells exhibited equivalent expression of LDLr at the mRNA level. This is an important finding because VSVΔM51 relies on the LDLr to enter host cells[95]. Equivalent LDLr expression across mutant ID8 cell lines suggests equal susceptibility to VSVΔM51 infection, which was evident across multiple experiments.

Findings generated using VSVΔM51-GFP for flow cytometry and microscopy also consistently showed the equivalent dose-dependent responses of ID8 cells to treatment. The only significant comparisons here were reduced GFP in ID8 *Trp53*$^{-/-}$ *Nf1*$^{-/-}$ and ID8 *Trp53*$^{-/-}$ *Brca1*$^{-/-}$ at MOI 10 measured using flow cytometry. This was likely biologically irrelevant since this result did not re-appear in microscopy and did not impact VSVΔM51 replication capacity.

In contrast, mutation status played a significant role in VSVΔM51 replication capacity in the FVB/N models at MOI 10. STOSE and MOE *Pten*^{shRNA} *KRas*^{G12V} cells replicated

approximately 10-fold more virus than the MOE *Pten*^{shRNA} or *Pten*^{shRNA} *Trp53*^{R273H} cells. In STOSE cells, this effect might be attributed to the faster growth rate (as evidenced by higher mean confluence) or other factors unique to this model. It has previously been shown that the RAS/RAF/MEK/Erk pathway, which is constitutively active in *KRas*^{G12V} mutant cells, facilitates VSV infection by restricting anti-viral IFN-I responses: this renders *KRas* mutant cells more sensitive to VSV infection[114]. In other experiments discussed in the following section, IFN-β production was shown to be reduced in the MOE *Pten*^{shRNA} *KRas*^{G12V} cells after treatment with VSVΔM51 for 6 hours at MOI 10, which supports this mechanism and result.

Fluorescent microscopy showed findings that were seemingly contradictory to those uncovered during analysis of VSVΔM51 replication: MOE *Pten*^{shRNA} *KRas*^{G12V} cells showed visibly low-level infection with VSVΔM51-GFP compared to other MOE cell lines at multiple MOIs. This data suggests weaker infection in MOE *Pten*^{shRNA} *KRas*^{G12V} cells, in contrast to the results discussed in the previous paragraph. Adding *KRas*^{G12V} mutation to the MOE *Pten*^{shRNA} cells similarly reduced the frequency and intensity of cell GFP expression as measured using flow cytometry, a finding that was significant at MOI 10. This result suggests reduced VSV infection and was unexpected due to A) previous literature showing *KRas* activation facilitates VSV infection[114], and B) the results above showing *KRas*^{G12V} mutation increased viral replication at MOI 10.

The microscopy and flow cytometry findings could suggest that cell death in the MOE *Pten*^{shRNA} *KRas*^{G12V} model is more abundant after VSVΔM51 infection; however, this was not evident in the previous Alamar Blue experiments 24h post-infection and is therefore not suspected at the shorter 6-hour post-infection timepoint tested here. Furthermore, LDLr gene expression was confirmed equivalent between all STOSE & MOE cells at baseline, thus reducing

the possibility of compromised viral entry in the MOE *Pten*^{shRNA} *KRas*^{G12V} cells. With these factors in mind, the results suggest that *KRas*^{G12V} mutated cells paradoxically supported higher viral production at MOI 10 but lower levels of infection.

It should be posited that viral titering measured VSVΔM51 released by cells into the supernatant, whereas microscopy and flow cytometry measured intracellular VSVΔM51. Therefore, more investigation is required to support the remaining paradox whereby few infected MOE *Pten*^{shRNA} *KRas*^{G12V} cells seem to be producing large quantities of VSVΔM51. A first experiment to shed light on this finding would be to repeat the above experiments with MOE *Pten*^{shRNA} *KRas*^{G12V} cells while using a functional inhibitor of KRAS. From this experiment, it should be noted whether or not any differences in viral replication kinetics are attenuated as a means to further validate the role of KRAS in producing the above results.

Overall, ID8 cells showed similar growth rates which supported equivalent, dose-dependent replication of VSVΔM51. STOSE and MOE *Pten*^{shRNA} *KRas*^{G12V} cells produced elevated quantities of VSVΔM51, though this finding in the latter cell line was conflicted by findings shown through flow cytometry and microscopy. Further research is required to elucidate this discrepancy.

4.1.4 VSVΔM51 Induced Immunogenicity Changes in ID8, STOSE and MOE Cell Lines.

Enhanced tumour immunogenicity post-VSVΔM51 infection is one mechanism that can help reverse immune suppression in the TME. VSVΔM51 infection (MOI 0.1) upregulated B2M and MHC-I (H2Db and H2Kb) gene expression in all ID8 cell lines, suggesting inducible antigen presentation in response to treatment. This effect was barely evident 6h post-infection and increased substantially at 12h post-infection. However, VSVΔM51 infection for 6 hours at any MOI was insufficient to increase MHC-I presentation on the surface of any cell type, as

measured by flow cytometry. In previous experiments, the Vanderhyden lab has shown that 24-hour treatment with IFN-γ enhances MHC-I surface presentation on the ID8 cells, which is low at baseline[56]. This result is expected to become apparent in VSVΔM51 treated cells with prolonged infection (ex. 12+ hours).

High MHC-I expression suggests good immunogenicity via antigen presentation. Though no consistent differences between ID8 expression of MHC-I genes were found, surface presentation of MHC-1 was significantly elevated in ID8 *Trp53*$^{-/-}$ *Brca1*$^{-/-}$ and ID8 *Trp53*$^{-/-}$ *Nf1*$^{-/-}$ cell lines. This finding was apparent at baseline and did not change after 6 hours of VSVΔM51 treatment. In our previous work, no significant differences in MHC-I surface presentation were found between the ID8 *Trp53*$^{-/-}$ *Brca1*$^{-/-}$ cells and their parental ID8 *Trp53*$^{-/-}$ F3 cells without treatment, but the ID8 *Trp53*$^{-/-}$ *Nf1*$^{-/-}$ cells have not previously been tested[56].

In the STOSE and MOE cells, the levels of MHC-I gene expression and surface presentation were consistent among cell lines within the same treatment group, barring one major exception. At 6h post-infection, MHC-I was presented more intensely on the surface of STOSE cells. High proportions of all four cell lines were MHC-1+; this finding is consistent with our previous study of STOSE/MOE cell immunogenicity *in-vitro* and held regardless of MOI[56]. However, 12h post-infection, all FVB/N cell lines exhibited reduced expression of B2M and H2Kq (MHC-1) genes, a finding that was not present at 6h post-infection and may limit tumour immunogenicity. This result is perhaps a FVB/N specific mechanism of immune evasion induced by viral infection, a hypothesis that could be evaluated through future study in the STOSE and MOE models.

PD-L1 surface presentation was present in all cell lines at baseline and increased with VSVΔM51 treatment regardless of mutation status; however, ID8 C3 cells exhibited more

intense PD-L1 expression at MOI 1 and 10. While counterintuitive, this effect of OV therapy is commonly observed in cancer cells as a mechanism to counteract newly induced inflammatory responses[52,116]. It is for this reason that OV therapy has shown promise when combined with PD-1/PD-L1 blockade[117]. As such, PD-L1 upregulation suggests strong infection has been achieved.

Tumour production of IFN-β is an important pro-inflammatory response that helps reverse immune suppression in the TME. Six hours of VSVΔM51 treatment was sufficient to induce IFN-β gene expression substantially in all cell lines. This finding suggests a solid pro-inflammatory response by all cell lines after infection that may translate to improved *in-vivo* responses to VSVΔM51 treatment. However, the responsiveness of each cell line to IFN-β production must be assessed to test this prediction. Additionally, IFN-I production post-VSVΔM51 remains to be quantified at the protein level via ELISA.

APCs are the primary producers of pro-inflammatory IFN-γ. As such, it was not expected that IFN-γ levels would change significantly among ID8, STOSE and MOE cells. All cell lines produced extremely low levels of IFN-γ regardless of mutation. No differences in IFN-γ production were found due to mutation in all cell lines measured at baseline and 6 hours post-infection. At 12h, ID8 *Trp53*$^{-/-}$ F3 and MOE *Pten*^{shRNA} cells showed increased production of IFN-γ within their respective comparison groups; this finding is likely biologically irrelevant and caused due to the lack of sensitivity in qPCR assays when measuring extremely low levels of gene expression, though it is worth noting for future study.

In summary, the above results present broad and early findings that collectively suggest increased immunogenicity in ID8, STOSE and MOE cell lines post-VSVΔM51 infection. Increased expression of key antigen presentation genes and the anti-viral IFN-β gene support better immune recognition of tumour cells, a mechanism that requires functional study to be

confirmed. MHC-I upregulation on the cell surface was not apparent at the protein level 6 hours post-infection but is expected to follow the same trend at later time points. Enhanced PD-L1 presentation in all cells suggests strong VSVΔM51 infection in all cell lines.

4.1.5 Additional Limitations and Future Direction of In-Vitro studies

During the early stages of this study, confluent adherent cell monolayers were subjected to treatment for carboplatin and OV sensitivity screening. While this monolayer model remains a mainstay of *in-vitro* study, tandem assessment of treatment sensitivity in 3D spheroid models would have provided enhanced relevance towards *in-vivo* studies. Spheroids are non-adherent cell clusters that capture the free-floating capacity of HGSC metastases in the ascites. These models are typically more chemotherapy resistant due to physical drug exclusion mechanisms and may also assist tumours in resisting OV infection[118,119].

Tong et al.[118] have tested three unique OVs – myxoma, VVDD and Maraba MG1 – against EOC spheroid models. They found that VVDD replication in spheroids was blocked at the lytic stage of the life cycle, a complication that does not typically arise in monolayer models. Initial spheroid infection by Maraba MG1, a *Rhabdovirus* with high similarity to VSV, was significantly attenuated. However, MG1 spread rapidly after successfully achieving this early step. The impact of specific genetic mutations in EOC spheroid models has yet to be assessed in the context of OV therapy; these models will provide more relevant *in-vitro* findings to support the results of *in-vivo* studies and to better understand the treatment responsiveness of metastasizing tumour cells.

Many interesting trends in gene expression were noted at 12h post-VSVΔM51 infection. Changes in gene expression were typically most substantial at this time point. However, supporting results by flow cytometry have only been completed at the 6h post-VSVΔM51

timepoint, though multiple MOIs have been tested. As such, it would be meaningful to re-assess immunogenicity via flow cytometry at the 12-hour time to support emerging trends in gene expression. This experiment would fill a missing piece in assessing immunogenicity changes due to tumour mutation post-VSVΔM51 infection.

4.2 In-Vivo Experiments

4.2.1 Survival Benefit of Carboplatin in Syngeneic Models with Specific Mutations

While not all HGSC cell lines examined *in-vitro* were selected for study using syngeneic *in-vivo* models, many mutations have been examined to understand the impact of specific genetic mutations on the TME and the response to therapy. Only one of the five models studied here achieved prolonged survival in response to carboplatin treatment: the MOE *Pten*^{shRNA} *KRas*^{G12V} tumour-bearing mice. This result was fewer than expected, given that carboplatin treatment is a mainstay of clinical HGSC therapy, and all cell lines responded to carboplatin *in-vitro*.

A recently published study by Shakfa, et al. assessed the survival benefit of carboplatin treatment in syngeneic mice harbouring IP injected ID8 *Trp53*$^{-/-}$ *Brca1*$^{-/-}$ and ID8 *Trp53*$^{-/-}$ *Pten*$^{-/-}$ tumours[120]. Though different ID8 cell models were used, the treatment regime utilized by Shafka, et al. provides insight into the lack of success found with carboplatin treatment during the present thesis project. Shakfa, et al. treated mice with eight IP doses at 10mg/kg administered bi-weekly for four weeks [120.] In contrast, tumour-bearing mice used for this thesis project were given a less frequent treatment regime consisting of three IP doses of carboplatin at 12.5mg/kg, administered once per week for three weeks. Shakfa et al. found prolonged survival in both models using a more rigorous treatment regime, despite the slightly lower dose.

The success of a lower carboplatin dose used by Shakfa, et al. suggests that longer duration and higher frequency of treatment may be superior in achieving a survival benefit. Additionally,

ID8 cells with *Brca1*$^{-/-}$ and *Brca2*$^{-/-}$ mutations were found to be highly carboplatin-responsive *in-vitro* (**Figure 8**). Thus, it is reasonable to predict that tumours generated using *Brca1/2* mutated cells would be more sensitive to carboplatin treatment *in-vivo*. After submission of this thesis for evaluation, ongoing experiments were completed in the Vanderhyden lab to address these possibilities. The efficacy of carboplatin treatment in three of the previously used *in-vivo* syngeneic models (ID8 *Trp53*$^{-/-}$ F3, MOE *Pten*^{shRNA} *Trp53*^{R273H} and MOE *Pten*^{shRNA} *KRas*^{G12V} tumour-bearing mice) was assessed again using a more rigorous treatment regime and mice bearing tumours derived from ID8 *Trp53*$^{-/-}$ *Brca1*$^{-/-}$ cells were also included. The new dosing strategy consisted of eight doses of carboplatin at 20mg/kg, administered bi-weekly for four weeks. All four models studied exhibited prolonged survival in response to this therapeutic regime (data not shown).

4.2.2 Survival Benefit of VSVΔM51 in Syngeneic Models with Specific Mutations

VSVΔM51 treatment significantly prolonged survival in three of six syngeneic tumour models tested. *Trp53*^{R273} oncomorphic or *KRas*^{G12V} activating mutations led to prolonged survival after VSVΔM51 treatment in MOE *Pten*^{shRNA} tumour models. Similarly, adding a *Brca2*$^{-/-}$ mutation to the ID8 *Trp53*$^{-/-}$ model resulted in a survival benefit after VSVΔM51 treatment *in-vivo*. Possible explanations for the ability of VSVΔM51 to prolong survival of these three models draws attention to mutation-associated differences in viral kinetics and the TME immune landscape.

Activation of KRAS is known to enhance replication of VSV; one mechanism of doing so could be facilitation of faster growth rates which support infection[96,114]. In this study, *in-vitro* experiments did not show statistically enhanced mean confluence in *KRas*^{G12V} mutated cells. However, MOE *Pten*^{shRNA} cells with an additional *KRas*^{G12V} mutation did grow to higher

confluence and exhibited enhanced capacity for VSVΔM51 replication. FVB/N derived tumours also exhibit strong MHC-I surface expression, which has been found in this study as well as previous research and supports tumour immunogenicity *in-vivo*[56]. If retained *in-vivo*, these factors would support rapid virus spread and anti-tumour immune responses after VSVΔM51 treatment. Consistent with this prediction, MOE *Pten*^{shRNA} *KRas*^{G12V} tumours exhibited the shortest survival time compared to all other models tested, and survival was prolonged the most by VSVΔM51 treatment. However, MOE *Pten*^{shRNA} *KRas*^{G12V} cells are non-immunogenic when administered as a cellular vaccine, and *KRas* mutation is associated with Treg conversion[56,67]. These factors must be overcome for adequate anti-tumour immunogenicity in *KRas* mutated tumours.

The VSVΔM51 induced survival benefit conferred by *Brca2*$^{-/-}$ mutation in the ID8 *Trp53*$^{-/-}$ cells is highly relevant since nearly all hereditary cases of HGSC are associated with *Brca1/2* mutation[24]. In contrast to the responsiveness *in-vivo*, *Brca2*$^{-/-}$ mutation in the *in-vitro* models did not significantly impact the replication of VSVΔM51 or immunogenicity induced by infection. Likely, immune factors associated with the TME of ID8 *Trp53*$^{-/-}$ *Brca2*$^{-/-}$ tumours are the primary mediators of this enhanced responsiveness *in-vivo.* We have previously shown that ID8 cells are non-immunogenic *in-vivo*, resulting in poor immune infiltration in the TME[56]. This ID8 model was therefore selected as a second model for TME analysis post-VSVΔM51 treatment (discussed in **section 4.2.3**) to help elucidate mechanisms underlying the response.

Of high importance, VSVΔM51 was able to prolong survival in one murine model that was non-responsive to carboplatin treatment: the MOE *Pten*^{shRNA} *Trp53*$^{R273H-}$ tumour-bearing mice. We have previously reported these cells to be immunogenic *in-vivo*[56]. In the FTE, mutant *Pten* and *Trp53* expression are associated with increased cell migration, suggesting aggressive

HGSC-like phenotypes[18,19]. In the current project, these cells were not typically outliers from the rest of the FVB/N-derived models in the analysis of viral replication and immunogenicity responses post-infection. While the TME response of this model to VSVΔM51 treatment has not yet been studied, the fact that both MOE models tested were responsive to VSV suggests that TME factors that are common to the MOE models may play a crucial role in prolonging the survival of these models.

Worthy of discussion is the common treatment timeline applied to all models. Treatment was commenced at 25% of the expected control mice survival time, which was unique for each model. While providing a standardized point in the tumour development timeline at which to administer VSVΔM51, the obvious result is that the duration of survival post-treatment was different for each model. This window of time could have proved insufficient for short-lived models to mount an ample anti-tumour immune response post-VSVΔM51, an advantage given to models that naturally survived longer without treatment. However, this unavoidable impact seemed to provide little effect since the model with the shortest expected survival time, the MOE *Pten*^{shRNA} *KRas*^{G12V} tumour-bearing mice, exhibited the longest duration of prolonged survival after treatment.

Finally, one interesting change in phenotype was observed in the *ID8 Trp53*$^{-/-}$ *Brca2*$^{-/-}$ tumour-bearing mice. Two cages, one housing PBS-treated mice and the other VSVΔM51-treated mice, developed “grey highlights” in their fur that were evenly dispersed across the entire body of the mice (photo in the appendix, **Figure 36**). This phenotype affected all mice housed in both affected cages but did not impact all mice belonging to either treatment group. The Vanderhyden lab has not previously noted this phenotype in any mouse models, and no literature has been found on this specific occurrence in tumour-bearing mice. However, greying of the hair

can be associated with innate immune responses[121]. The only obvious commonalities among all mice affected are the presence of an IP injected tumour and their living in the same cage; however, since ID8 *Trp53*$^{-/-}$ *Brca2*$^{-/-}$ cells are non-immunogenic[56], it is unclear what specific target is mediating this immune response. The Vanderhyden lab looks forward to seeing if this phenotype is reproduced in future experiments.

Analysis of immune activation upon VSVΔM51 treatment in responsive mice may help provide a mechanism by which tumour suppression is uniquely driven in mutated tumour models. These findings are discussed in the following section for the ID8 *Trp53*$^{-/-}$ *Brca2*$^{-/-}$ and MOE *Pten*^{shRNA} *KRas*^{G12V} mice.

4.2.3 Immune Responses in the TME to Prolong Survival of VSVΔM51 Treated Murine Models

In the peritoneal wash, VSVΔM51 treatment of MOE *Pten*^{shRNA} *KRas*$^{G12V+}$ tumours induced significant CD4+ T cell presence, whereas *ID8* Trp53$^{-/-}$ *Brca2*$^{-/-}$ mice responded with a significantly increased presence of CD8+ T cells (**Figure 22**). A shift to increased CD8+ and CD4+ T cells, respectively, was also seen in each model despite the lack of statistical significance. Treatment with VSV reduced the proportion of NK cells amongst the total lymphocyte populations in both models and NK cells did not appear to become activated. CD8+ T cells and NK cells are the primary effectors of immune-mediated tumour killing and the presence of these two cell types is strongly associated with improved survival outcomes in HGSC patients[41,42,73]. However, both types of T lymphocytes are crucial to achieving strong anti-tumour immune responses. NK cells can be recruited to the TME within hours of an OV infection[122], and as a member of the innate immune system their peak activation has likely already passed at the 5-day post-infection timepoint assessed here.

An increase in T lymphocytes in the peritoneal TME, instead of NK or myeloid cells, is likely a primary mechanism responsible for the prolonged survival in VSVΔM51 responsive mice since it is consistent in both models. The decreased proportion of TAMs and DC-1 cells in the ID8 *Trp53*$^{-/-}$ *Brca2*$^{-/-}$ model is consistent with the preference for these tumour cell types to recruit lymphocytes to the TME[56].

Activation of lymphocyte and myeloid-derived immune populations in the peritoneal wash of VSVΔM51 responsive models was also explored (**Figure 23** and **Figure 24**). Most notably, PD-L1 expression was increased in CD4+ and CD8+ T cells belonging to both MOE *Pten*^{shRNA} *KRas*^{G12V} and ID8 *Trp53*$^{-/-}$ *Brca2*$^{-/-}$ tumour-bearing mice. This status suggests increased activation of immune cells through mechanisms driven by IFN upregulation in VSVΔM51 treated samples[52,116,117].

CD25 is the IL-2 receptor alpha chain; the population of CD4+ CD25+ T lymphocytes predominantly includes immunosuppressive Treg cells. The frequency and intensity of CD25 presentation on CD4+ T cells was generally decreased in both models, suggesting lowered Treg presence. A lack of Tregs, in combination with increased CD8+ T lymphocytes, is an excellent prognostic predictor and consistent with the survival benefit conferred by VSVΔM51 found in these mice[123,124].

LAG3 is a common marker of lymphocyte exhaustion, and its expression was unchanged in all lymphocyte cells studied; a lack of LAG3 co-expression on PD-1+ cells suggests non-exhaustion of the immune cells resulting in less inhibition of anti-tumour immune responses[125]. For instance, Yang, et al, showed that LAG3^{-} PD-1^{+} T lymphocytes derived from the TME of a follicular lymphoma model were functionally active, whereas LAG3^{+} PD-1^{+} T lymphocytes were not [125]. Furthermore, blockade of both LAG3 and PD-1 on intra-tumoural CD8+ T cells resulted

in enhanced IFN-γ and IL-2 production [125]. These results support the above findings that T lymphocytes in the peritoneal TME with increased PD-1 expression had been activated but were not exhausted due to lack of LAG3 induction.[125] NKp46 and NKG2D are both activating receptors on NK cells; the lack of consistent changes in either marker is consistent with the evidence supporting non-NK cell-mediated survival benefits in VSVΔM51 treated mice[126,127].

Regarding the peritoneal-derived myeloid cells, few consistent differences existed to suggest activation after VSVΔM51 treatment. A few notable trends were still found in these populations. MHC-II was consistently downregulated by VSVΔM51 treatment in cDC-1 cells from both MOE *Pten*^{shRNA} *KRas*^{G12V} and ID8 *Trp53*$^{-/-}$ *Brca2*$^{-/-}$ models. This trend is subtle but also present in cDC-2 cells from MOE mice and macrophages in ID8 mice. Loss of MHC-II suggests attenuated antigen presentation capacity, despite the immune-stimulatory treatment with VSVΔM51. In addition, the co-stimulatory ligand, CD86, was largely unaffected by VSVΔM51 treatment in either mode. PD-L1 presentation was upregulated in only a few myeloid cells, notably the macrophages and DC-1 cells from MOE *Pten*^{shRNA} *KRas*^{G12V} mice.

In summary, the enhanced survival seen in MOE *Pten*^{shRNA} *KRas* and ID8 *Trp53*$^{-/-}$ *Brca2*$^{-/-}$ tumours after VSVΔM51 treatment was associated with preferred activation of CD4+ and CD8+ T cells. *KRas* mutation has previously been associated with the presence of immunosuppressive cells in the TME[67]. *Trp53* and *Brca2* mutations are associated with aggressive cancer phenotypes[24,59]. As such, it is promising to see improved immune activation due to VSVΔM51 treatment in murine models carrying these mutations. In both models, consistent activation of CD4+ and CD8+ is favoured to prolong survival after treatment compared to NK or myeloid-derived cells. Both cell types are lacking in many immune-suppressed environments seen in HGSC, which are strongly associated with poor prognosis.[73,128]

4.2.4 Additional Limitations and Future Directions of In-Vivo Studies

The results from *in-vivo* experiments have shed light on the effect of specific tumour mutations on the response to VSVΔM51 immunotherapy. In particular, analyzing the TME in two VSVΔM51 responsive models helped to uncover immune factors that likely prolonged survival in these mice. Notably, the MOE *Pten*^{shRNA} *Trp53*^{R273H} model was one of three models in which VSVΔM51 treatment prolonged survival. However, the TME of this model has yet to be analyzed to enable comparisons of the immune responses to VSVΔM51 treatment. This experiment is necessary to complete the above initial analysis.

Throughout the *in-vivo* studies presented above, the cell lines used to create syngeneic tumours and the VSV strain used for treatment did not express any reporter transgenes. As a result, our ability to monitor tumour burden or *in-vivo* VSV replication, respectively, over time was severely limited. With reporter use, such measurements could help elucidate subtle differences in the rate of tumour progression due to the specific mutations present. However, reporters such as FLuc and GFP are immunogenic [129,130]. This is especially true in the FVB/N mice and the Vanderhyden lab has previously found various reporters to attenuate tumorigenicity of the STOSE cells. In such cases, reporter expression can cause tumour implant rejection and confound immune targeting of the tumours due to transgene-directed immune responses [129,130]. As such, the best course of action for this study was to forgo the use of reporters in all cell lines and VSVΔM51 treatments used for *in-vivo* study, regardless of host mouse strain, despite the potential loss of relevant findings. This ensured consistency of methods between tumour models and eliminated off-target immune responses that may confound results.

All cells in this project were implanted into mice via IP injection. This method has many benefits, including ease of tumour implantation and modelling of the peritoneal ascites TME.

Syngeneic orthotopic tumour models are another option with unique benefits that have yet to be fully explored in the context of HGSC immunotherapy. Orthotopic tumours restrict implanted cells to the ovary (i.e. the primary site of HGSC development) due to the bursa surrounding the ovary in mice[56,71]. Tumours thus grow within the ovarian TME that preferentially gives rise to nascent HGSC tumours. The Vanderhyden lab has already assessed the TME of orthotopic tumours using many of the same cell lines highlighted in this project[56]. Therefore, enhanced clinical relevance could be achieved by using syngeneic orthotopic models to test the impact of specific tumour mutations on the response to VSVΔM51 therapy.

Carboplatin and VSV treatment were used independently for this project. However, many studies are now showing the synergistic action of carboplatin and OV combination therapy regimes[41,81]. A natural next step for *in-vivo* research would be to assess these two treatments together using the same murine models tested above. This treatment regime could further evaluate the impact of specific tumour mutations on therapeutic outcomes in mice and potentially prolong survival in mice found unresponsive to both monotherapy regimes.

Finally, many OVs, including VSVΔM51, have been further developed to include the expression of pro-inflammatory transgenes, such as GM-CSF[75]. The onboarding of transgenes into the OV genome allows for enhanced immunogenicity of the tumour cells after infection through stimulation of the TME[75]. Testing OVs with pro-inflammatory transgenes in the same models utilized for this project has the potential to prolong survival in mice unresponsive to VSVΔM51 or enhance differences in VSV responsiveness due to TME factors associated with tumour mutation status.

4.3 Summary & Concluding Remarks

It was hypothesized that the sensitivity of HGSC models to chemotherapy and OV infection would be influenced by the presence of clinically relevant, specific mutations. The findings of this project report a few mutation-associated differences that support this statement. When tested *in-vitro*, *Brca1*$^{-/-}$ and *Brca2*$^{-/-}$ mutation significantly increased sensitivity to carboplatin. The chemotherapy sensitivity of tumour models created using cells with these mutations has been assessed by others, who report a similar finding.

Three OVs were screened in genetically diverse murine HGSC models *in-vitro*, and VSVΔM51 was selected for use in subsequent experiments. The expression of the VSV entry receptor, *Ldlr*, was equivalent within each cell group. No significant or biologically relevant impact of genetic mutation was found in ID8 *in-vitro* cell models in response to VSV. However, adding *KRas*^{G12V} mutation to the MOE *Pten*^{shRNA} cells enhanced VSVΔM51 production *in-vitro*. Tumour cells responded to VSVΔM51 infection *in-vitro* with increased MHC-I, PD-L1 and IFN-β expression at the gene or protein level; these markers suggest increased immune responses.

Only one of five syngeneic IP tumour models exhibited prolonged survival due to carboplatin treatment. However, survival was prolonged in half of all models treated with VSVΔM51. Notably, in two of the VSVΔM51-responsive models, treatment was associated with CD4+ and CD8+ T cell activation in the peritoneal TME.

This project provides evidence that clinically relevant specific tumour mutations uniquely modify the response to OV therapy due to modification of immune responses or supporting enhanced viral replication. These results warrant further study to elucidate mechanisms behind the significant findings noted above. Understanding the impact these mutations have on OV

efficacy in HGSC models will help guide the development of novel therapies. The future of OV therapy is undoubtedly promising for patients with the genetic heterogeneity of HGSC.

References

1. Sherwood L, Ward C. The Reproductive Cycle. In: *Human Physiology: From Cells to Systems*. 3rd Canadi. Nelson Education Ltd.; 2016:745-756.

2. Mescher AL, ed. The Female Reproductive System. In: *Junqueira's Basic Histology Text and Atlas*. 16th ed. McGraw Hill; 2021.

3. Brenner DR, Poirier A, Woods RR, et al. Projected estimates of cancer in Canada in 2022. *CMAJ*. 2022;194(17):E601-E607. doi:10.1503/CMAJ.212097

4. Society CC. Canadian Cancer Statistics 2021. Published online 2021. https://cancer.ca/en/research/cancer-statistics/canadian-cancer-statistics

5. Stewart C, Ralyea C, Lockwood S. Ovarian Cancer: An Integrated Review. *Semin Oncol Nurs*. 2019;35(2):151-156. doi:10.1016/j.soncn.2019.02.001

6. Koshiyama M, Matsumura N, Konishi I. Recent concepts of ovarian carcinogenesis: Type I and type II. *Biomed Res Int*. 2014;2014. doi:10.1155/2014/934261

7. Koshiyama M, Matsumura N, Konishi I. Subtypes of Ovarian Cancer and Ovarian Cancer Screening. *Diagnostics*. 2017;7(1):12. doi:10.3390/diagnostics7010012

8. Hirst J, Crow J, Godwin A. Ovarian Cancer Genetics : Subtypes and Risk Factors. In: Devaja O, Papadopoulos A, eds. *Ovarian Cancer - From Pathogenesis to Treatment*. IntechOpen; 2018:2-38. doi:10.5772/intechopen.72705

9. Canadian Cancer Society. Stages of Ovarian Cancer. Accessed April 7, 2020. https://www.cancer.ca/en/cancer-information/cancer-type/ovarian/staging/?region=on

10. Tentes AK, Tripsiannis G, Markakidis SK, et al. Peritoneal cancer index : a prognostic indicator of survival in advanced ovarian cancer. *European Journal of Surgical Oncology*. 2003;(29):69-73. doi:10.1053/ejso.2002.1380

11. Salehi F, Dunfield L, Phillips KP, Krewski D, Vanderhyden BC. Risk factors for ovarian cancer: An overview with emphasis on hormonal factors. *J Toxicol Environ Health B Crit Rev*. 2008;11(3-4):301-321. doi:10.1080/10937400701876095

12. Walker JL, Powell CB, Chen LM, et al. Society of Gynecologic Oncology recommendations for the prevention of ovarian cancer. *Cancer*. 2015;121(13):2108-2120. doi:10.1002/cncr.29321

13. McCloskey CW, Goldberg RL, Carter LE, et al. A new spontaneously transformed syngeneic model of high-grade serous ovarian cancer with a tumor-initiating cell population. *Front Oncol*. 2014;4 MAR(March):1-13. doi:10.3389/fonc.2014.00053

14. Roby KF, Taylor CC, Sweetwood JP, et al. Development of a syngeneic mouse model for events related to ovarian cancer. *Carcinogenesis*. 2000;21(4):585-591. doi:10.1093/carcin/21.4.585

15. Kim J, Park EY, Kim O, et al. Cell origins of high-grade serous ovarian cancer. *Cancers (Basel)*. 2018;10(11):1-28. doi:10.3390/cancers10110433

16. Shih IM, Wang Y, Wang TL. The Origin of Ovarian Cancer Species and Precancerous Landscape. *American Journal of Pathology*. 2021;191(1):26-39. doi:10.1016/j.ajpath.2020.09.006

17. Russo A, Czarnecki AA, Dean M, et al. PTEN loss in the fallopian tube induces hyperplasia and ovarian tumor formation. *Oncogene*. 2018;37:1976-1990. doi:10.1038/s41388-017-0097-8

18. Quartuccio SM, Karthikeyan S, Eddie SL, et al. Mutant p53 expression in fallopian tube epithelium drives cell migration. *Int J Cancer*. 2015;137:1528-1538. doi:10.1002/ijc.29528

19. Eddie SL, Quartuccio SM, Eoghainin Ó, et al. Tumorigenesis and peritoneal colonization from fallopian tube epithelium. *Oncotarget*. 2015;6(24).

20. Modi DA, Tagare RD, Karthikeyan S, et al. PAX2 Function, Regulation and Targeting in Fallopian Tube Derived High Grade Serous Ovarian Cancer. *Physiol Behav*. 2017;176(12):139-148. doi:10.1016/j.physbeh.2017.03.040

21. Perets R, Wyant G, Muto K, et al. Transformation of the Fallopian Tube Secretory Epithelium Leads to High-grade Serous Ovarian Cancer in Brca;Tp53;Pten Models. *Cancer Cell*. 2013;24(6):751-765. doi:10.1016/j.ccr.2013.10.013

22. Hanley GE, Pearce CL, Talhouk A, et al. Outcomes from Opportunistic Salpingectomy for Ovarian Cancer Prevention. *JAMA Netw Open*. 2022;5(2):1-10. doi:10.1001/jamanetworkopen.2021.47343

23. Roy R, Chun J, Powell SN. BRCA1 and BRCA2: different roles in a common pathway of genome protection. *Nat Rev Cancer*. 2016;12(1):68-78. doi:10.1038/nrc3181.BRCA1

24. Ramus SJ, Gayther SA. The Contribution of BRCA1 and BRCA2 to Ovarian Cancer. *Mol Oncol*. 2009;3(2):138-150. doi:10.1016/j.molonc.2009.02.001

25. Yoshida R. Hereditary breast and ovarian cancer (HBOC): review of its molecular characteristics, screening, treatment, and prognosis. *Breast Cancer*. 2021;28(6):1167-1180. doi:10.1007/s12282-020-01148-2

26. Robles-dıa L, Goldfrank DJ, Kauff ND, Robson M, Offit K. Hereditary ovarian cancer in Ashkenazi Jews. *Fam Cancer*. 2004;(3):259-264.

27. Herreros-Villanueva M, Chen CC, Tsai EM, Er TK. Endometriosis-associated ovarian cancer: What have we learned so far? *Clinica Chimica Acta*. 2019;493(January):63-72. doi:10.1016/j.cca.2019.02.016

28. Landry DA, Vaishnav HT, Vanderhyden BC. The significance of ovarian fibrosis. *Oncotarget*. 2020;11(47):4366-4370. doi:10.18632/ONCOTARGET.27822

29. Momenimovahed Z, Tiznobaik A, Taheri S, Salehiniya H. Ovarian cancer in the world: Epidemiology and risk factors. *Int J Womens Health*. 2019;11:287-299. doi:10.2147/IJWH.S197604

30. Chohan L, Richardson DL. ACOG Comittee Opinion Number 774: Opportunistic Salpingectomy as a Strategy for Epithelial Ovarian Cancer Prevention. *Obstetrics and Gynecology*. 2019;133(4):E279-E284. doi:10.1097/AOG.0000000000003164

31. Olson S, Mignone L, Nakraseive C, Caputo T, Barakat R, Harlep S. Symptoms of Ovarian Cancer. *Obstetrics & Gynecology*. 2001;98(2):212-217. doi:10.1097/00006250-200112000-00036

32. Given-Wilson R. Ovarian Cancer Screening - Ultrasound; Impact on Ovarian Cancer Mortality. *British Journal of Radiology*. 2018;91(1090). doi:10.1259/bjr.20189003

33. Kobal B, Noventa M, Cvjeticanin B, et al. Primary debulking surgery versus primary neoadjuvant chemotherapy for high grade advanced stage ovarian cancer: Comparison of survivals. *Radiol Oncol*. 2018;52(3):307-319. doi:10.2478/raon-2018-0030

34. Chern JY, Curtin JP. Appropriate Recommendations for Surgical Debulking in Stage IV Ovarian Cancer. *Curr Treat Options Oncol*. 2016;17(1):1-10. doi:10.1007/s11864-015-0380-2

35. Pokhriyal R, Hariprasad R, Kumar L, Hariprasad G. Chemotherapy Resistance in Advanced Ovarian Cancer Patients. *Biomark Cancer*. 2019;11:1-19. doi:10.1177/1179299x19860815

36. Elies A, Rivière S, Pouget N, et al. The role of neoadjuvant chemotherapy in ovarian cancer. *Expert Rev Anticancer Ther*. 2018;18(6):555-566. doi:10.1080/14737140.2018.1458614

37. Glasgow MA, Argenta P, Abrahante JE, et al. Biological insights into chemotherapy resistance in ovarian cancer. *Int J Mol Sci*. 2019;20(9). doi:10.3390/ijms20092131

38. Oun R, Moussa YE, Wheate NJ. The side effects of platinum-based chemotherapy drugs: a review for chemists. *Dalton Transactions*. 2018;47(19):6635-6870. doi:10.1039/C8DT00838H

39. Mateo J, Lord CJ, Serra V, et al. A decade of clinical development of PARP inhibitors in perspective. *Annals of Oncology*. 2019;30(9):1437-1447. doi:10.1093/annonc/mdz192

40. Klotz DM, Wimberger P. Overcoming PARP inhibitor resistance in ovarian cancer: what are the most promising strategies? *Arch Gynecol Obstet*. 2020;302(5):1087-1102. doi:10.1007/s00404-020-05677-1

41. Rodriguez GM, Galpin KJ, McCloskey CW, Vanderhyden BC. The Tumour Microenvironment of Epithelial Ovarian Cancer and Its Influence on Response to Immunotherapy. *Cancers (Basel)*. 2018;10(8):242. https://www.ncbi.nlm.nih.gov/pmc/articles/PMC6116043/

42. Fucikova J, Coosemans A, Orsulic S, et al. Immunological configuration of ovarian carcinoma: Features and impact on disease outcome. *J Immunother Cancer*. 2021;9(10):1-26. doi:10.1136/jitc-2021-002873

43. Dhatchinamoorthy K, Colbert JD, Rock KL. Cancer Immune Evasion Through Loss of MHC Class I Antigen Presentation. *Front Immunol*. 2021;12(March). doi:10.3389/fimmu.2021.636568

44. Yoshihama S, Roszik J, Downs I, et al. NLRC5/MHC class I transactivator is a target for immune evasion in cancer. *Proc Natl Acad Sci U S A*. 2016;113(21):5999-6004. doi:10.1073/pnas.1602069113

45. Wang RF, Wang HY. Immune targets and neoantigens for cancer immunotherapy and precision medicine. *Cell Res*. 2017;27(1):11-37. doi:10.1038/cr.2016.155

46. Gonzalez H, Hagerling C, Werb Z. Roles of the immune system in cancer : from tumor initiation to metastatic progression. *Genes Dev*. 2018;32:1267-1284. doi:10.1101/gad.314617.118.tissue

47. Denton NL, Chen CY, Scott TR, Cripe TP. Tumor-associated macrophages in oncolytic virotherapy: Friend or foe? *Biomedicines*. 2016;4(3). doi:10.3390/biomedicines4030013

48. Böttcher JP, Reis e Sousa C. The Role of Type 1 Conventional Dendritic Cells in Cancer Immunity. *Trends Cancer*. 2018;4(11):784-792. doi:10.1016/j.trecan.2018.09.001

49. Saito Y, Komori S, Kotani T, Murata Y, Matozaki T. The Role of Type-2 Conventional Dendritic Cells in the Regulation of Tumor Immunity. *Cancers (Basel)*. 2022;14(8). doi:10.3390/cancers14081976

50. Rodriguez GM, Bobbala D, Serrano D, et al. NLRC5 elicits antitumor immunity by enhancing processing and presentation of tumor antigens to CD8+ T lymphocytes. *Oncoimmunology*. 2016;5(6):1-12. doi:10.1080/2162402X.2016.1151593

51. Parvathareddy SK, Siraj AK, Al-Badawi IA, Tulbah A, Al-Dayel F, Al-Kuraya KS. Differential expression of PD-L1 between primary and metastatic epithelial ovarian cancer and its clinico-pathological correlation. *Sci Rep*. 2021;11(1):1-9. doi:10.1038/s41598-021-83276-z

52. Han Y, Liu D, Li L. PD-1/PD-L1 pathway: current researches in cancer. *Am J Cancer Res*. 2020;10(3):727-742. http://www.ncbi.nlm.nih.gov/pubmed/32266087

53. Bou-Tayeh B, Miller ML. Ovarian tumors orchestrate distinct cellular compositions. *Immunity*. 2021;54(6):1107-1109. doi:10.1016/j.immuni.2021.05.014

54. Hornburg M, Desbois M, Lu S, et al. Single-cell dissection of cellular components and interactions shaping the tumor immune phenotypes in ovarian cancer. *Cancer Cell*. 2021;39(7):928-944.e6. doi:10.1016/j.ccell.2021.04.004

55. Iyer S, Zhang S, Yucel S, et al. *Genetically Defined Syngeneic Mouse Models of Ovarian Cancer as Tools for the Discovery of Combination Immunotherapy*.; 2020. doi:10.1158/2159-8290.CD-20-0818

56. Rodriguez GM, Galpin KJ, Cook DP, et al. The Tumor Immune Profile of Murine Ovarian Cancer Models: An Essential Tool for Ovarian Cancer Immunotherapy Research. *Cancer Research Communications*. 2022;2(6):417-433. https://aacrjournals.org/cancerrescommun/article/2/6/417/704808/The-Tumor-Immune-Profile-of-Murine-Ovarian-Cancer

57. The Cancer Genome Atlas Research Network. Integrated Genomic Analyses of Ovarian Carcinoma. *Nature*. 2011;474(7353):609-615. doi:10.1038/nature10166.Integrated

58. Brachova P, Thiel KW, Leslie KK. The consequence of oncomorphic TP53 mutations in ovarian cancer. *Int J Mol Sci*. 2013;14(9):19257-19275. doi:10.3390/ijms140919257

59. Buttitta F, Marchetti A, Gadducci A, et al. P53 alterations are predictive of chemoresistance and aggressiveness in ovarian carcinomas: A molecular and immunohistochemical study. *Br J Cancer*. 1997;75(2):230-235. doi:10.1038/bjc.1997.38

60. Ren YA, Mullany LK, Liu Z, Herron AJ, Wong KK, Richards JAS. Mutant p53 promotes epithelial ovarian cancer by regulating tumor differentiation, metastasis, and responsiveness to steroid hormones. *Cancer Res*. 2016;76(8):2206-2218. doi:10.1158/0008-5472.CAN-15-1046

61. Shah CA, Allison KH, Garcia RL, Gray HJ, Goff BA, Swisher EM. Intratumoral T cells, tumor-associated macrophages, and regulatory T cells: Association with p53 mutations, circulating tumor DNA and survival in women with ovarian cancer. *Gynecol Oncol*. 2008;109(2):215-219. doi:10.1016/j.ygyno.2008.01.010

62. Dai Y, Sun C, Feng Y, Jia Q, Zhu B. Potent immunogenicity in BRCA1-mutated patients with high-grade serous ovarian carcinoma. *J Cell Mol Med*. 2018;22(8):3979-3986. doi:10.1111/jcmm.13678

63. Chalhoub N, Baker SJ. PTEN and the PI3-Kinase Pathway in Cancer. *Annual Review of Pathology: Mechanisms of Disease*. 2009;4(1):127-150. doi:10.1146/annurev.pathol.4.110807.092311

64. Nakayama N, Nakayama K, Yeasmin S, et al. KRAS or BRAF mutation status is a useful predictor of sensitivity to MEK inhibition in ovarian cancer. *Br J Cancer*. 2008;(99):2020-2028. doi:10.1038/sj.bjc.6604783

65. Martins FC, Santiago I de, Trinh A, et al. Combined image and genomic analysis of high-grade serous ovarian cancer reveals PTEN loss as a common driver event and prognostic classifier. Published online 2014:1-15.

66. Martins FC, Couturier DL, Paterson A, et al. Clinical and pathological associations of PTEN expression in ovarian cancer: a multicentre study from the Ovarian Tumour Tissue Analysis Consortium. *Br J Cancer*. 2020;123(5):793-802. doi:10.1038/s41416-020-0900-0

67. Zdanov S, Mandapathil M, Eid RA, et al. Mutant KRAS conversion of conventional T cells into regulatory T cells. *Cancer Immunol Res*. 2016;4(4):354-365. doi:10.1158/2326-6066.CIR-15-0241

68. Tao J, Sun D, Dong L, Zhu H, Hou H. Advancement in research and therapy of NF1 mutant malignant tumors. *Cancer Cell Int*. 2020;20(1):1-8. doi:10.1186/s12935-020-01570-8

69. Walton J, Blagih J, Ennis D, et al. CRISPR/Cas9-mediated Trp53 and Brca2 knockout to generate improved murine models of ovarian high-grade serous carcinoma. *Cancer Res*. 2016;76(20):6118-6129. doi:10.1158/0008-5472.CAN-16-1272

70. Walton JB, Farquharson M, Mason S, et al. CRISPR/Cas9-derived models of ovarian high grade serous carcinoma targeting Brca1, Pten and Nf1, and correlation with platinum sensitivity. *Sci Rep*. 2017;7(16827). doi:10.1038/s41598-017-17119-1

71. Karakashev S, Zhang RG. Mouse models of epithelial ovarian cancer for preclinical studies. *Zool Res*. 2021;42(2):153-160. doi:10.24272/J.ISSN.2095-8137.2020.382

72. McCloskey CW, Rodriguez GM, Galpin KJ, Vanderhyden BC. Ovarian Cancer Immunotherapy : Preclinical Models and Emerging Therapeutics. *Cancers (Basel)*. 2018;10:244. doi:10.3390/cancers10080244

73. Sato E, Olson SH, Ahn J, et al. Intraepithelial CD8+ tumor-infiltrating lymphocytes and a high CD8+/regulatory T cell ratio are associated with favorable prognosis in ovarian cancer. *Proc Natl Acad Sci U S A*. 2005;102(51):18538-18543. doi:10.1073/pnas.0509182102

74. Gujar SA, Lee PWK. Oncolytic virus-mediated reversal of impaired tumor antigen presentation. *Front Oncol*. 2014;4 APR(April):1-7. doi:10.3389/fonc.2014.00077

75. Lemos de Matos A, Franco LS, McFadden G. Oncolytic Viruses and the Immune System: The Dynamic Duo. *Mol Ther Methods Clin Dev*. 2020;17(June):349-358. doi:10.1016/j.omtm.2020.01.001

76. Galluzzi L, Buqué A, Kepp O, Zitvogel L, Kroemer G. Immunogenic cell death in cancer and infectious disease. *Nat Rev Immunol*. 2017;17:97-111. doi:10.1038/nri.2016.107

77. Marelli G, Howells A, Lemoine NR, Wang Y. Oncolytic viral therapy and the immune system: A double-edged sword against cancer. *Front Immunol*. 2018;9(APR):1-8. doi:10.3389/fimmu.2018.00866

78. Coukos G, Makrigiannakis A, Kang EH, Rubin SC, Albelda SM, Molnar-Kimber KL. Oncolytic herpes simplex virus-1 lacking ICP34.5 induces p53-independent death and is efficacious against chemotherapy-resistant ovarian cancer. *Clinical Cancer Research*. 2000;6(8):3342-3353.

79. Vankerckhoven A, Baert T, Riva M, et al. Type of chemotherapy has substantial effects on the immune system in ovarian cancer. *Transl Oncol*. 2021;14(6):101076. doi:10.1016/j.tranon.2021.101076

80. Kodumudi KN, Woan K, Gilvary DL, Sahakian E, Wei S, Djeu JY. A Novel Chemoimmunomodulating Property of Docetaxel: Supression of Myeloid-Derived Supressors Cells in Tumour Bearers. *Clinical Cancer Research*. 2010;16(18). doi:10.1158/1078-0432.CCR-10-0733

81. Nguyen A, Ho L, Wan Y. Chemotherapy and oncolytic virotherapy: Advanced tactics in the war against cancer. *Front Oncol*. 2014;4 JUN(June):1-10. doi:10.3389/fonc.2014.00145

82. Macedo N, Miller DM, Haq R, Kaufman HL. Clinical landscape of oncolytic virus research in 2020. *J Immunother Cancer*. 2020;8(2). doi:10.1136/jitc-2020-001486

83. Ma W, He H, Wang H. Oncolytic herpes simplex virus and immunotherapy. *BMC Immunol*. 2018;19(1):1-11. doi:10.1186/s12865-018-0281-9

84. Li Y, Zhang C, Chen X, et al. ICP34.5 protein of herpes simplex virus facilitates the initiation of protein translation by bridging eukaryotic initiation factor 2α (eIF2α) and protein phosphatase 1. *Journal of Biological Chemistry*. 2011;286(28):24785-24792. doi:10.1074/jbc.M111.232439

85. Wilcox DR, Longnecker R. The Herpes Simplex Virus Neurovirulence Factor γ34.5: Revealing Virus–Host Interactions. *PLoS Pathog*. 2016;12(3). doi:10.1371/journal.ppat.1005449

86. Yang X, Huang B, Deng L, Hu Z. Progress in gene therapy using oncolytic vaccinia virus as vectors. *J Cancer Res Clin Oncol*. 2018;144(12):2433-2440. doi:10.1007/s00432-018-2762-x

87. Hung C f, Tsai Y c, He L, et al. Vaccinia virus preferentially infects and controls human and murine ovarian tumors in mice. *Gene Ther*. 2007;14:20-29. doi:10.1038/sj.gt.3302840

88. McCart JA, Ward JM, Lee J, et al. Systemic cancer therapy with a tumor-selective vaccinia virus mutant lacking thymidine kinase and vaccinia growth factor genes. *Cancer Res*. 2001;61(24):8751-8757.

89. Buller RM, Chakrabarti S, Cooper JA, Twardzik DR, Moss B. Deletion of the vaccinia virus growth factor gene reduces virus virulence. *J Virol*. 1988;62(3):866-874. doi:10.1128/jvi.62.3.866-874.1988

90. Parato KA, Breitbach CJ, le Boeuf F, et al. The oncolytic poxvirus JX-594 selectively replicates in and destroys cancer cells driven by genetic pathways commonly activated in cancers. *Molecular Therapy*. 2012;20(4):749-758. doi:10.1038/mt.2011.276

91. Zeh HJ, Downs-Canner S, McCart JA, et al. First-in-man study of western reserve strain oncolytic vaccinia virus: Safety, systemic spread, and antitumor activity. *Molecular Therapy*. 2015;23(1):202-214. doi:10.1038/mt.2014.194

92. Felt SA, Grdzelishvili VZ. Ecent advances in vesicular stomatitis virus-based oncolytic virotherapy: A 5-year update. *Journal of General Virology*. 2017;98(12):2895-2911. doi:10.1099/jgv.0.000980

93. Bishnoi S, Tiwari R, Gupta S, Byrareddy SN, Nayak D. Oncotargeting by Vesicular Stomatitis Virus (VSV): Advances in cancer therapy. *Viruses*. 2018;10(2):1-20. doi:10.3390/v10020090

94. Orzechowska BU, Jedryka M, Zwolinska K, Matkowski R. VSV based virotherapy in ovarian cancer: The past, the present and future? *J Cancer*. 2017;8(12):2369-2383. doi:10.7150/jca.19473

95. Finkelshtein D, Werman A, Novick D, Barak S, Rubinstein M. LDL receptor and its family members serve as the cellular receptors for vesicular stomatitis virus. *Proc Natl Acad Sci U S A*. 2013;110(18):7306-7311. doi:10.1073/pnas.1214441110

96. Balachandran S, Porosnicu M, Barber GN. Oncolytic Activity of Vesicular Stomatitis Virus Is Effective against Tumors Exhibiting Aberrant p53, Ras, or Myc Function and Involves the Induction of Apoptosis. *J Virol*. 2001;75(7):3474-3479. doi:10.1128/jvi.75.7.3474-3479.2001

97. Rajani KR, Pettit Kneller EL, McKenzie MO, Horita DA, Chou JW, Lyles DS. Complexes of Vesicular Stomatitis Virus Matrix Protein with Host Rae1 and Nup98 Involved in Inhibition of Host Transcription. *PLoS Pathog*. 2012;8(9). doi:10.1371/journal.ppat.1002929

98. Quan B, Seo HS, Blobel G, Ren Y. Vesiculoviral matrix (M) protein occupies nucleic acid binding site at nucleoporin pair (Rae1•Nup98). *Proc Natl Acad Sci U S A*. 2014;111(25):9127-9132. doi:10.1073/pnas.1409076111

99. Black BL, Rhodes RB, McKenzie M, Lyles DS. The role of vesicular stomatitis virus matrix protein in inhibition of host-directed gene expression is genetically separable from its function in virus assembly. *J Virol*. 1993;67(8):4814-4821. doi:10.1128/jvi.67.8.4814-4821.1993

100. Gaddy DF, Lyles DS. Vesicular Stomatitis Viruses Expressing Wild-Type or Mutant M Proteins Activate Apoptosis through Distinct Pathways. *J Virol*. 2005;79(7):4170-4179. doi:10.1128/jvi.79.7.4170-4179.2005

101. Hastie E, Grdzelishvili VZ. Vesicular stomatitis virus as a flexible platform for oncolytic virotherapy against cancer. *Journal of General Virology*. 2012;93(PART 12):2529-2545. doi:10.1099/vir.0.046672-0

102. Publicover J, Ramsburg E, Robek M, Rose JK. Rapid Pathogenesis Induced by a Vesicular Stomatitis Virus Matrix Protein Mutant: Viral Pathogenesis Is Linked to Induction of Tumor Necrosis Factor Alpha. *J Virol*. 2006;80(14):7028-7036. doi:10.1128/jvi.00478-06

103. Macfarlane D, Sommerville R. VERO Cells (Cercopithecus Aethiops Kidney): Growth Characteristics and Viral Susceptibility for Use in Diagnostic Virology. *Arch Gesamte Virusforsch*. 1969;27:379-385.

104. Diallo JS, Vähä-Koskela M, le Boeuf F, Bell J. Propagation, Purification, and In Vivo Testing of Oncolytic Vesicular Somatitis Virus Strains. In: Kirn DH, Liu TC, Thorne SH, eds. *Oncolytic Viruses: Methods and Protocols*. 1st ed. Humanna Press; 2012:127-140. https://link-springer-com.proxy.bib.uottawa.ca/book/10.1007/978-1-61779-340-0#about-this-book

105. Garcia V, Krishnan R, Davis C, et al. High-throughput Titration of Luciferase-expressing Recombinant Viruses. *Journal of Visualized Experiments*. 2014;(September):1-8. doi:10.3791/51890

106. Reles A, Wen WH, Gee C, et al. Correlation of p53 mutations with resistance to platinum-based chemotherapy and shortened survival in ovarian cancer. *Clinical Cancer Research*. 2001;7(10):2984-2997.

107. Brachova P, Mueting SR, Carlson MJ, et al. TP53 oncomorphic mutations predict resistance to platinum- and taxane-based standard chemotherapy in patients diagnosed with advanced serous ovarian carcinoma. *Int J Oncol*. 2015;46(2):607-618. doi:10.3892/ijo.2014.2747

108. Alvarado-Ortiz E, de la Cruz-López KG, Becerril-Rico J, Sarabia-Sánchez MA, Ortiz-Sánchez E, García-Carrancá A. Mutant p53 Gain-of-Function: Role in Cancer Development, Progression, and Therapeutic Approaches. *Front Cell Dev Biol*. 2021;8(February):1-24. doi:10.3389/fcell.2020.607670

109. El-Deiry WS. The role of p53 in chemosensitivity and radiosensitivity. *Oncogene*. 2003;22(47 REV. ISS. 6):7486-7495. doi:10.1038/sj.onc.1206949

110. Pestell KE, Hobbs SM, Titley JC, Kelland LR, Walton MI. Effect of p53 status on sensitivity to platinum complexes in a human ovarian cancer cell line. *Mol Pharmacol*. 2000;57(3):503-511. doi:10.1124/mol.57.3.503

111. Hudson CD, Savadelis A, Nagaraj AB, et al. Altered glutamine metabolism in platinum resistant ovarian cancer. *Oncotarget*. 2016;7(27):41637-41649. doi:10.18632/oncotarget.9317

112. Desbats MA, Giacomini I, Prayer-Galetti T, Montopoli M. Metabolic Plasticity in Chemotherapy Resistance. *Front Oncol*. 2020;10(281). doi:10.3389/fonc.2020.00281

113. Foulkes WD. BRCA1 and BRCA2: Chemosensitivity, treatment outcomes and prognosis. *Fam Cancer*. 2006;5(2):135-142. doi:10.1007/s10689-005-2832-5

114. Noser JA, Mael AA, Sakuma R, et al. The RAS/Raf1/MEK/ERK signaling pathway facilitates VSV-mediated oncolysis: Implication for the defective interferon response in cancer cells. *Molecular Therapy*. 2007;15(8):1531-1536. doi:10.1038/sj.mt.6300193

115. Clark-Knowles K v., Garson K, Jonkers J, Vanderhyden BC. Conditional inactivation of Brca1 in the mouse ovarian surface epithelium results in an increase in preneoplastic changes. *Exp Cell Res*. 2007;313(1):133-145. doi:10.1016/j.yexcr.2006.09.026

116. Farrukh H, El-Sayes N, Mossman K. Mechanisms of PD-L1 regulation in malignant and virus-infected cells. *Int J Mol Sci*. 2021;22(9):1-19. doi:10.3390/ijms22094893

117. Chen CY, Hutzen B, Wedekind MF, Cripe TP. Oncolytic virus and PD-1/PD-L1 blockade combination therapy. *Oncolytic Virother*. 2018;Volume 7:65-77. doi:10.2147/ov.s145532

118. Tong JG, Valdes YR, Barrett JW, et al. Evidence for differential viral oncolytic efficacy in an in vitro model of epithelial ovarian cancer metastasis. *Mol Ther Oncolytics*. 2015;2(July):15013. doi:10.1038/mto.2015.13

119. Pinto B, Henriques AC, Silva PMA, Bousbaa H. Three-dimensional spheroids as in vitro preclinical models for cancer research. *Pharmaceutics*. 2020;12(12):1-38. doi:10.3390/pharmaceutics12121186

120. Shakfa N, Li D, Conseil G, et al. PTEN and BRCA1 tumor suppressor loss associated tumor immune microenvironment exhibits differential response to therapeutic STING pathway activation in a murine model of ovarian cancer. Published online 2022.

121. Harris ML, Fufa TD, Palmer JW, et al. A direct link between MITF, innate immunity, and hair graying. *PLoS Biol*. 2018;16(5). doi:10.1371/journal.pbio.2003648

122. Alvarez-Breckenridge CA, Yu J, Price R, et al. NK cells impede glioblastoma virotherapy via NKp30 and NKp46 natural cytotoxicity receptors. *National Medicine*. 2013;18(12):1827-1834. doi:10.1038/nm.3013.NK

123. Zhang L, Conejo-Garcia JR, Katsaros D, et al. Intratumoral T cells, Recurrence, and Survival in Epithelial Ovarian Cancer. *N Engl J Med*. 2003;348(3):203-213.

124. Facciabene A, Motz GT, Coukos G. T-Regulatory cells: Key players in tumor immune escape and angiogenesis. *Cancer Res*. 2012;72(9):2162-2171. doi:10.1158/0008-5472.CAN-11-3687

125. Yang Z, Kim H, Villasboas JC, et al. Expression of Lag-3 Defines Exhaustion of Intratumoral Pd-1 + T Cells and Correlates With Poor Outcome in Follicular Lymphoma . *Hematol Oncol*. 2017;35(37):260-261. doi:10.1002/hon.2438_128

126. Hadad U, Thauland TJ, Martinez OM, Butte MJ, Porgador A, Krams SM. NKp46 clusters at the immune synapse and regulates NK cell polarization. *Front Immunol*. 2015;6(SEP):1-11. doi:10.3389/fimmu.2015.00495

127. Wensveen FM, Jelenčić V, Polić B. NKG2D: A master regulator of immune cell responsiveness. *Front Immunol*. 2018;9(MAR). doi:10.3389/fimmu.2018.00441

128. Rodriguez GM, Galpin KJC, McCloskey CW, Vanderhyden BC. The Tumor Microenvironment of Epithelial Ovarian Cancer and Its Influence on Response to Immunotherapy. *Cancers (Basel)*. 2018;10(8):242. doi:10.3390/cancers10080242

129. Ansari AM, Ahmed AK, Matsangos AE, et al. Cellular GFP Toxicity and Immunogenicity: Potential Confounders in in Vivo Cell Tracking Experiments. *Stem Cell Rev Rep*. 2016;12(5):553-559. doi:10.1007/s12015-016-9670-8

130. Limberis MP, Bell CL, Wilson JM. Identification of the murine firefly luciferase-specific CD8 T-cell epitopes. *Gene Ther*. 2009;16(3):441-447. doi:10.1038/gt.2008.177

Appendix

5.1 Flow Cytometry Gating Strategies

5.1.1 In-Vitro Gating for Murine HGSC Cell Immunogenicity Post-VSVΔM51 Infection

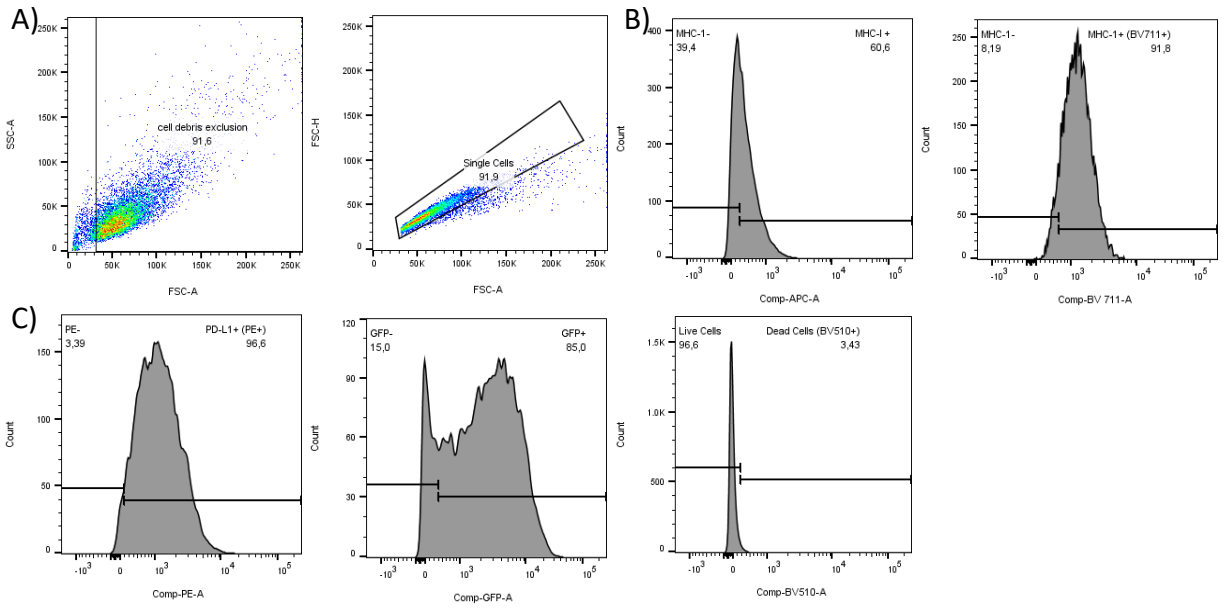

Figure 25: Flow cytometry gating for ID8, STOSE and MOE cells infected with VSVΔM51. *All acquisition was performed using the BD LRSFortessa™. A) All events were gated to exclude cell debris and identify single cells. B) ID8 cells were gated based on fluorescence minus one controls to identify MHC-I positive subtypes, using H2K/Db or H2D/Lq stain for the ID8 and STOSE/MOE samples, respectively. C) All cells were gated identically based on fluorescence minus one controls for PD-L1 expression, GFP expression, and viability.*

5.1.2 In-Vivo Panel 1 Lymphocyte Gating Strategy for Murine TME Analysis .

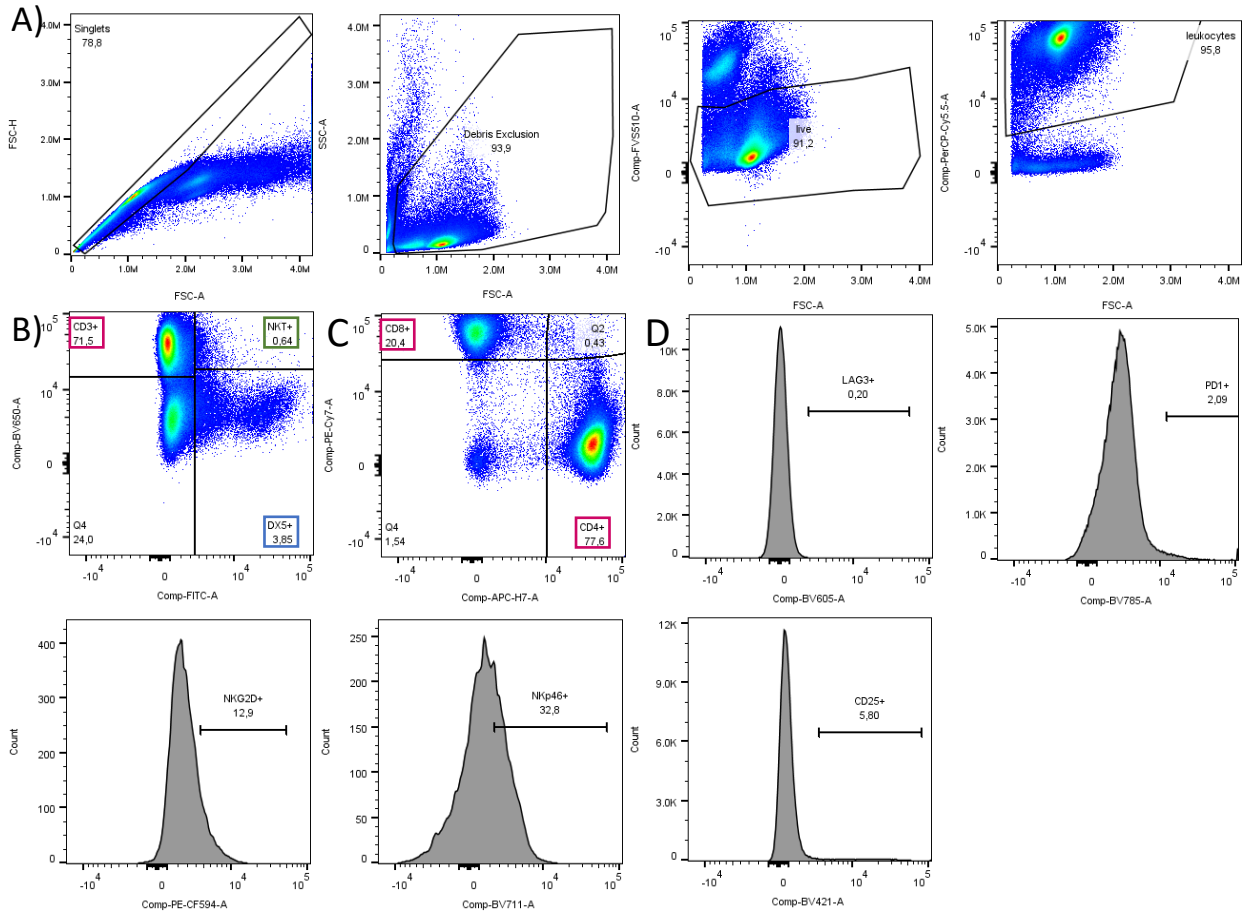

Figure 26: Flow cytometry gating strategy for lymphocytes collected from the murine TME. *All in-vivo samples were acquired using the Cytek® Aurora. Gating strategy was identical for all spleen, mLN and peritoneal wash samples collected from mice bearing syngeneic tumours treated with PBS or VSVΔM51. A) From all events the following gates were made to select for CD45+ leukocyte populations: singlets; debris exclusion, live cells ($BV510^{High}$) , CD45+ leukocytes (PerCP-Cy5+). B) Within the $CD45^{+}$ leukocytes, multiple cell types were distinguished including $CD3^{+}$ T cells (BV650+; FITC-), CD3+ and NK1.1+ NK-T cells (BV650+; FITC+), and NK1.1+ NK cells (BV650-; FITC+). C) Within the CD3+ T cells, CD4+ T cells (APC-H7+; PE-Cy7-) and CD8+ T cells (APC-H7-; PE-Cy7+) were distinguished. D) For each immune cell selected, the % positive of the parent population (i.e. current population minus the last applied gate) was gated using fluorescence-minus-one controls. Marker include LAG3, PD-1, NKG2D, NKp46 and CD25. MFI of each cell population was also calculated using geometric mean.*

5.1.3 In-Vivo Panel 2 Myeloid Cell Gating Strategy for Murine TME Analysis .

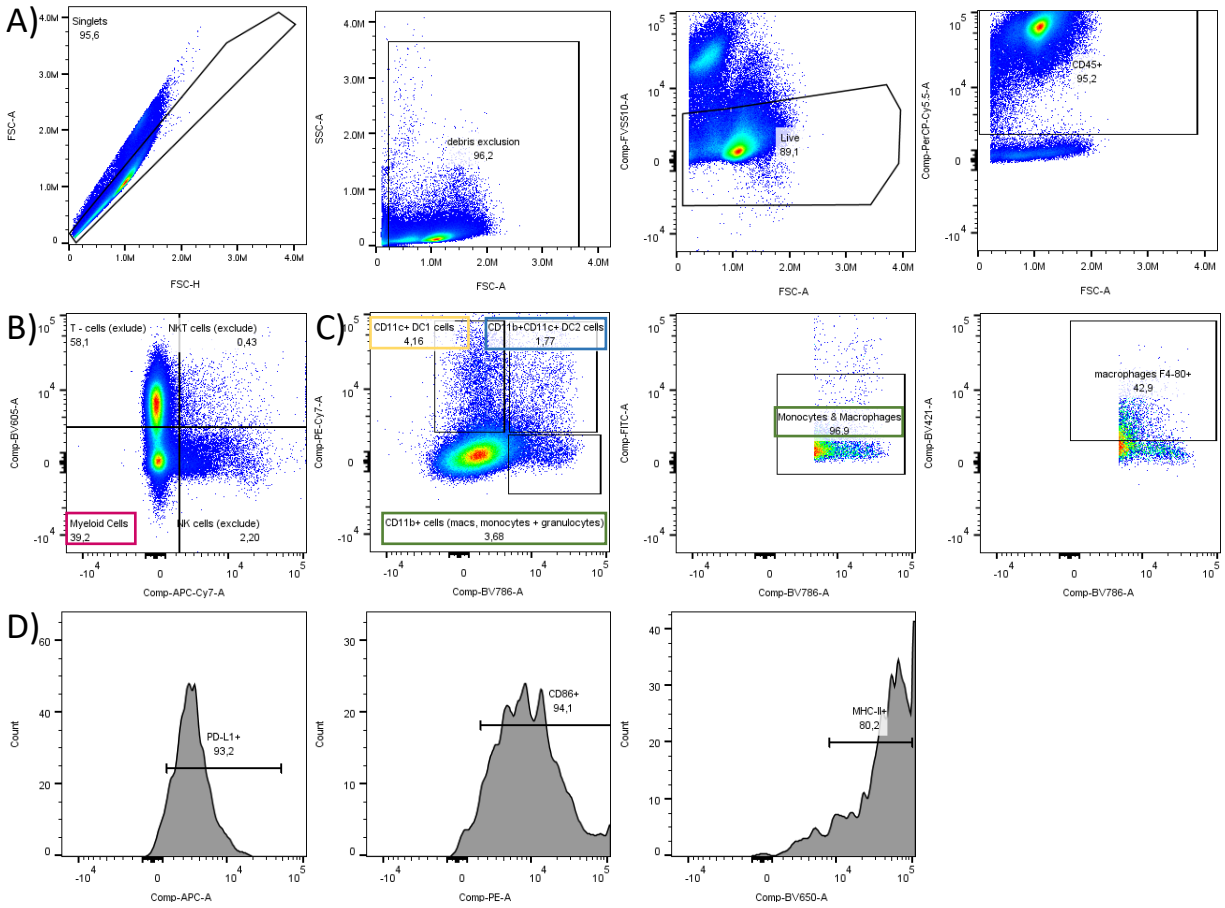

Figure 27: Flow cytometry gating strategy for myeloid cells collected from the murine TME. *All in-vivo samples were acquired using the Cytek® Aurora. Gating strategy was identical for all spleen, mLN and peritoneal wash samples collected from mice bearing syngeneic tumours treated with PBS or VSVΔM51. A) From all events the following gates were made to select for CD45+ leukocyte populations: singlets; debris exclusion, live cells ($BV510^{High}$) , CD45+ leukocytes (PerCP-Cy5+). B) Within the $CD45^{+}$ leukocytes, myeloid cell types were selected for based on absence of CD3e (BB605-) and NK1.1 (APC-Cy7-). C) Within the myeloid population, DC1 (CD11c+; CD11b-) and DC2 (CD11c+; CD11b+) cells were gated directly from the myeloid population. Macrophages were selected for based on CD11c-, CD11b+, GR1 low (FITC low) and F4/80 high (BV421 high) staining. D) For each immune cell selected, the % positive of the parent population (i.e. current population minus the last applied gate) was gated using fluorescence-minus-one controls. Marker include PD-L1, CD86 and MHC-II. MFI of each cell population was also calculated using geometric mean.*

5.2 Necropsy Statistics of Syngeneic Tumour Bearing Mice Treated with Carboplatin or VSVΔM51.

Below are the necropsy findings from experiments outlined in Section 3.4. In both studies, assessing efficacy of carboplatin or VSVΔM51 efficacy *in-vivo*, three necropsy measurements were collected: spleen weight, tumour weight, and ascites volume.

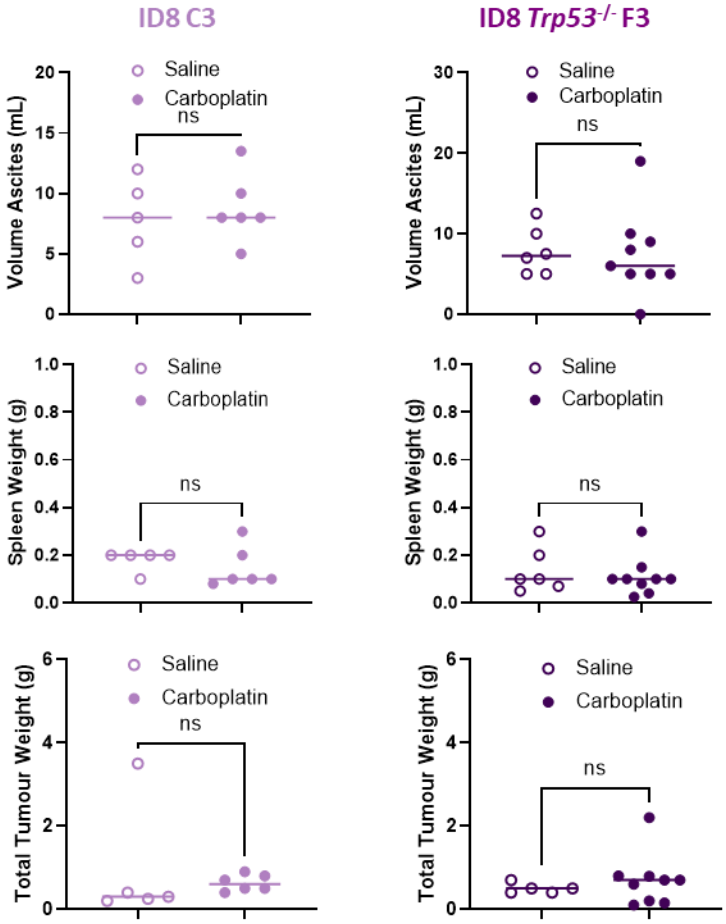

Figure 28: Necropsy findings of ID8 syngeneic tumour bearing mice treated with carboplatin. *C57BL/6 mice bearing syngeneic, intraperitoneal tumours were treated at 25% of expected survival with three doses of carboplatin (12.5mg/kg). After euthanasia at ethical endpoint, A) ascites volume, B) spleen weight, C) and total tumour weight were measured. Analysis was done via T-test with Welch's correction.*

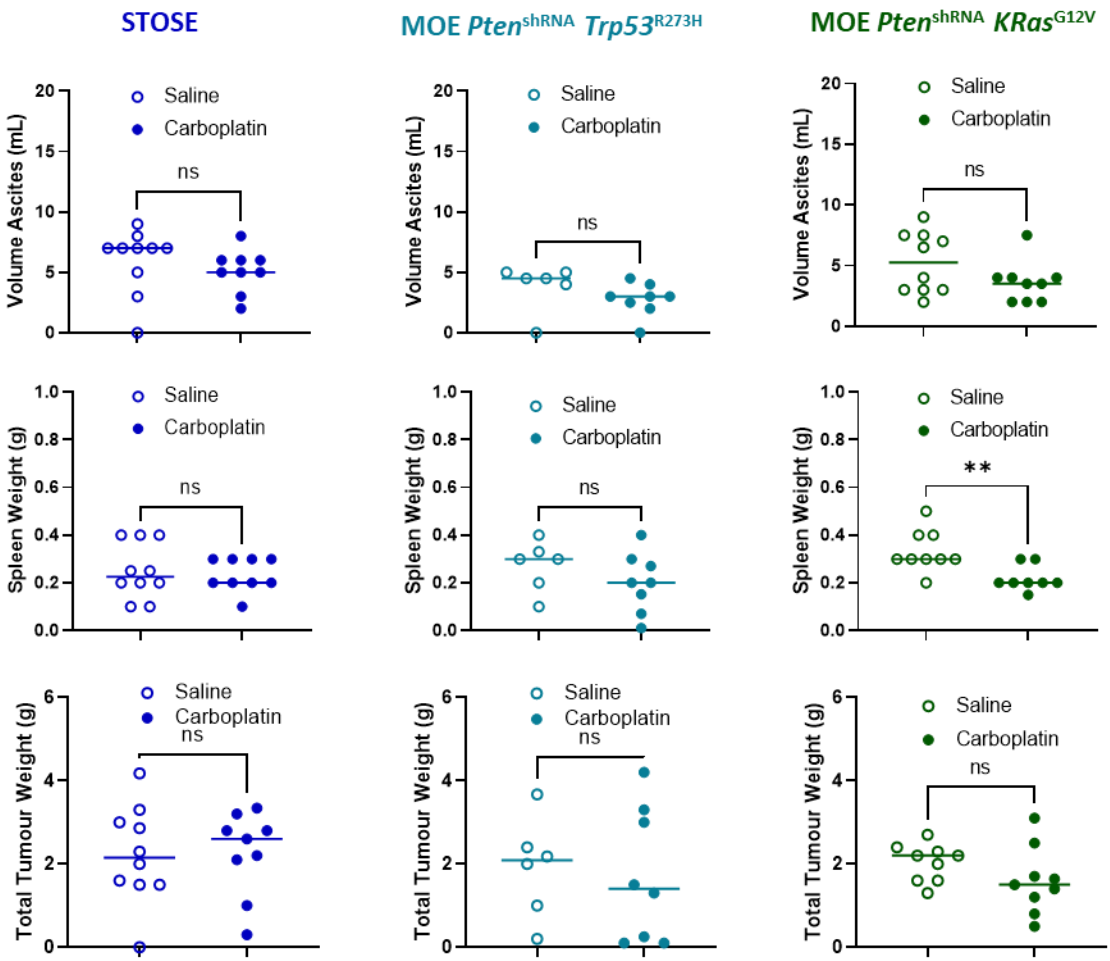

Figure 29: Necropsy findings of STOSE and MOE syngeneic tumour bearing mice treated with carboplatin. *FVB/N mice bearing syngeneic, intraperitoneal tumours were treated at 25% of expected survival with three doses of carboplatin (12.5mg/kg). After euthanasia at ethical endpoint, A) ascites volume, B) spleen weight, C) and total tumour weight were measured. Analysis was done via T-test with Welch's correction.**$p<0.001$.*

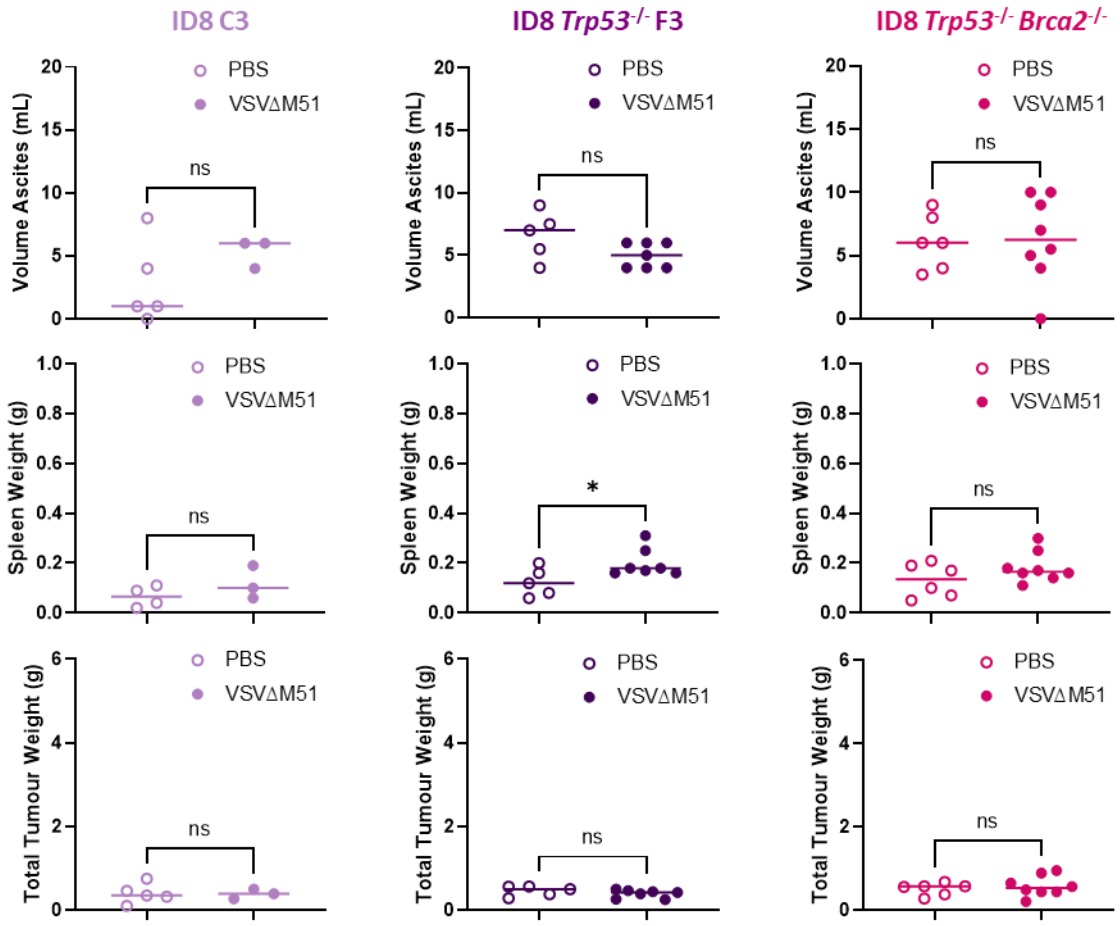

Figure 30: Necropsy findings of ID8 syngeneic tumour bearing mice treated with VSVΔM51. *C57BL/6 mice bearing syngeneic, intraperitoneal tumours were treated at 25% of expected survival with three doses of VSVΔM51 ($3e^8$ PFU/dose). After euthanasia at ethical endpoint, A) ascites volume, B) spleen weight, C) and total tumour weight were measured. Analysis was done via T-test with Welch's correction.*p<0.01.*

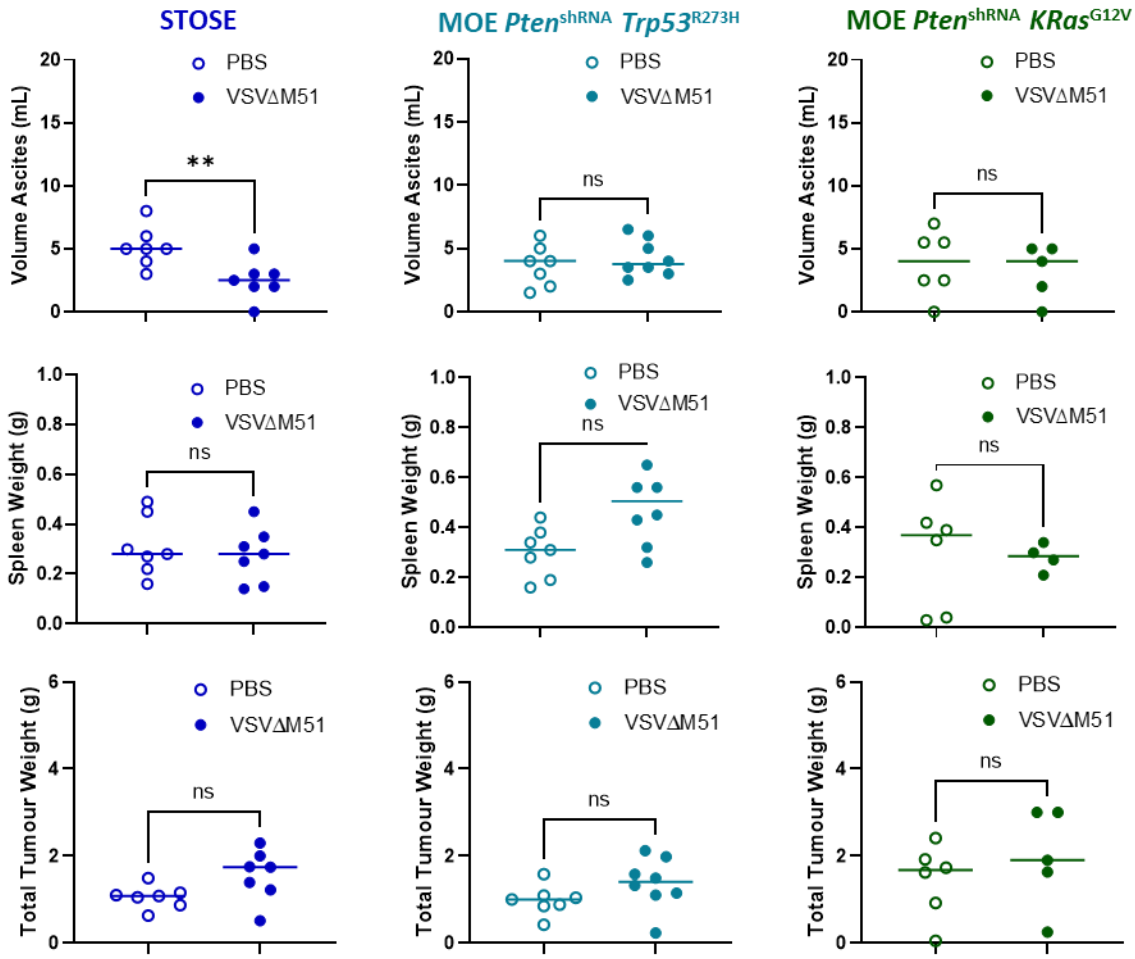

Figure 31: Necropsy findings of STOSE and MOE syngeneic tumour bearing mice treated with VSVΔM51. *FVB/N mice bearing syngeneic, intraperitoneal tumours were treated at 25% of expected survival with three doses of VSVΔM51 ($3e^8$ PFU/dose). After euthanasia at ethical endpoint, A) ascites volume, B) spleen weight, C) and total tumour weight were measured. Analysis was done via T-test with Welch's correction.**p<0.001.*

5.3 Immune Activation at Distant Immune Hubs of VSVΔM51 Treated Tumour Bearing Mice

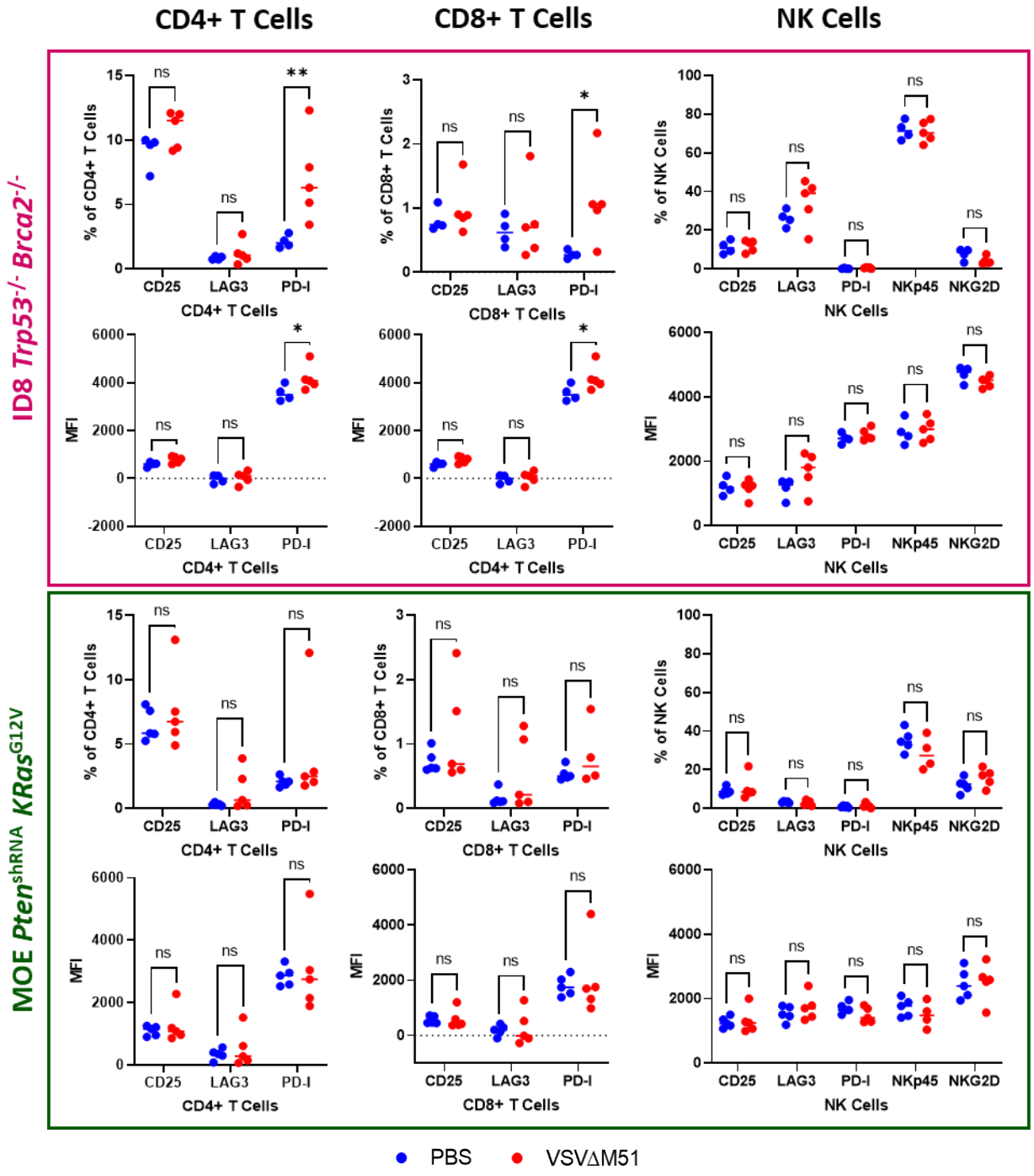

Figure 32: Activation markers of lymphocyte immune cells collected from mesenteric lymph nodes of tumour bearing mice treated with VSVΔM51. *CD4+ T cells, CD8+ T cells and NK cells were collected from the peritoneal wash of ID8 Trp53$^{-/-}$ Brca2$^{-/-}$ and MOE PTEN^{shRNA} KRas^{G12V} mice, previously treated with PBS control or VSVΔM51. Flow cytometry analysis of activation markers CD25, LAG3 and PD-1 was performed. *p<0.05, **p<0.01, ****p<0.0001.*

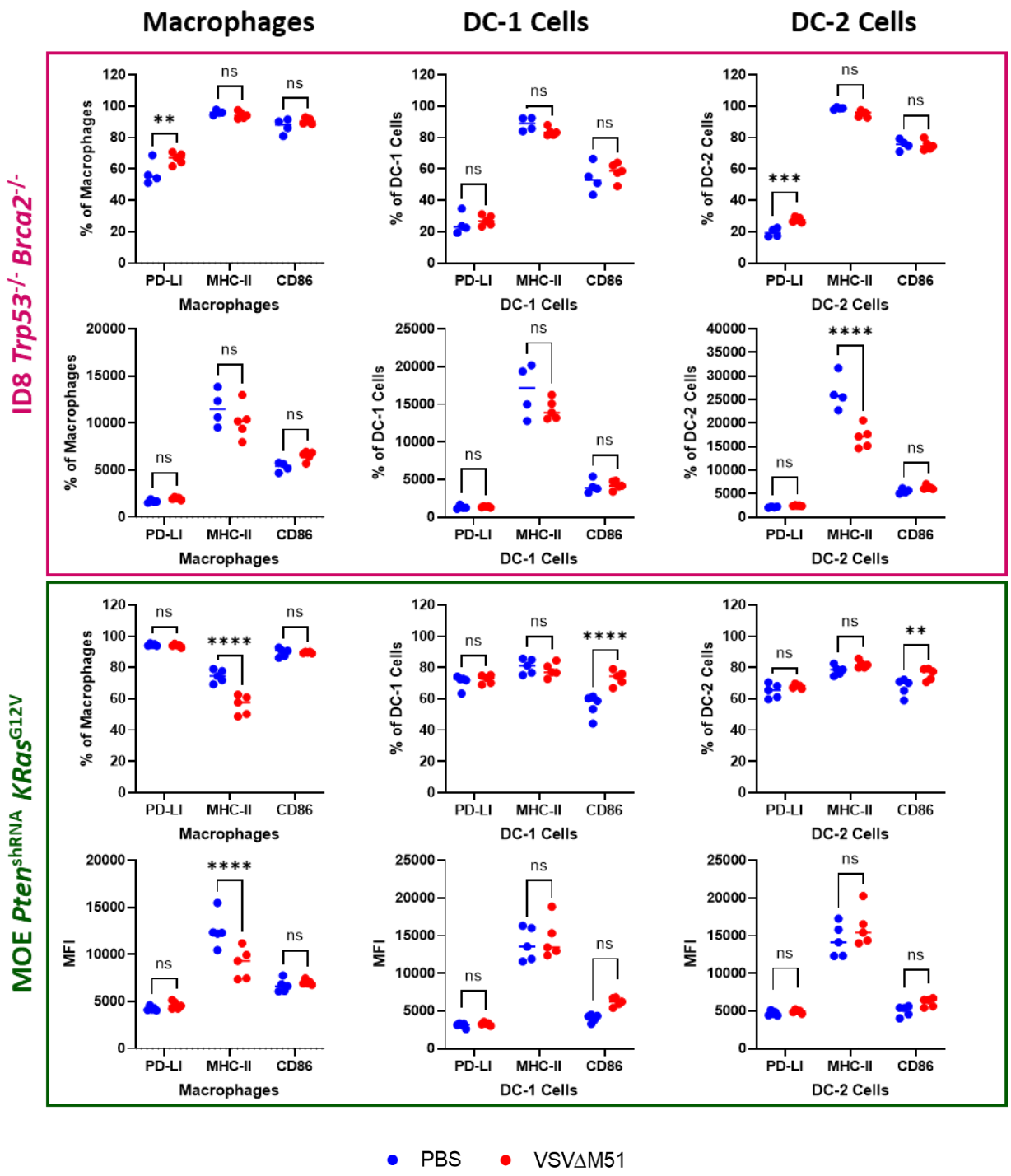

Figure 33: Activation markers of myeloid immune cells collected from mesenteric lymph nodes of tumour bearing mice treated with VSVΔM51. *Macrophages, DC-1 cells, and CD-2 cells were collected from the peritoneal wash of ID8 Trp53$^{-/-}$ Brca2$^{-/-}$ and MOE PTEN^{shRNA} KRas^{G12V} mice, previously treated with PBS control or VSVΔM51. Flow cytometry analysis of activation markers CD25, LAG3 and PD-1 was performed. *p<0.05, ****p<0.0001.*

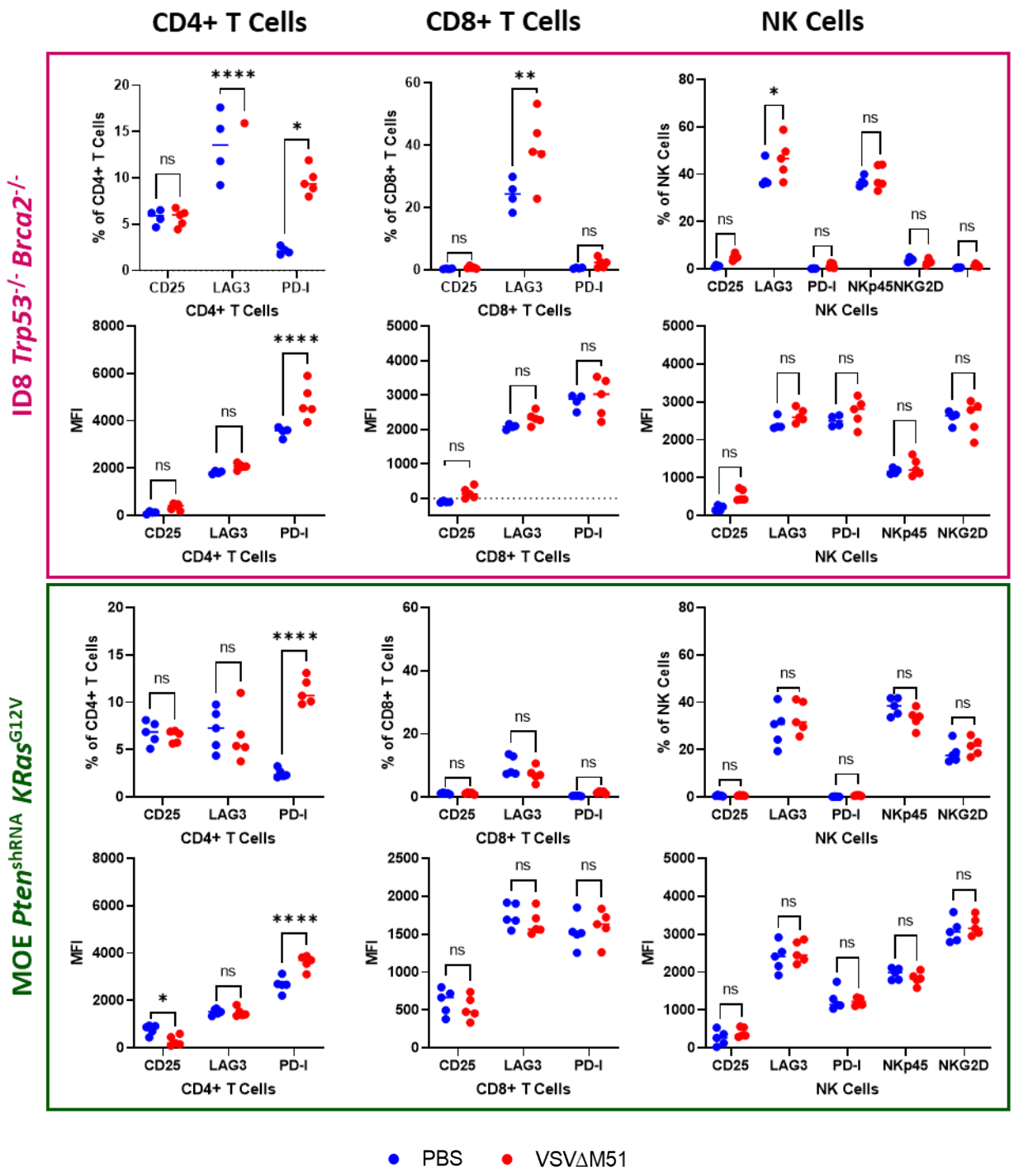

Figure 34: Activation markers of lymphocyte immune cells collected from spleens of tumour bearing mice treated with VSVΔM51. *CD4+ T cells, CD8+ T cells and NK cells were collected from the peritoneal wash of ID8 Trp53$^{-/-}$ Brca2$^{-/-}$ and MOE PTEN^{shRNA} KRas^{G12V} mice, previously treated with PBS control or VSVΔM51. Flow cytometry analysis of activation markers CD25, LAG3 and PD-1 was performed. *p<0.05, **p<0.01, ****p<0.0001.*

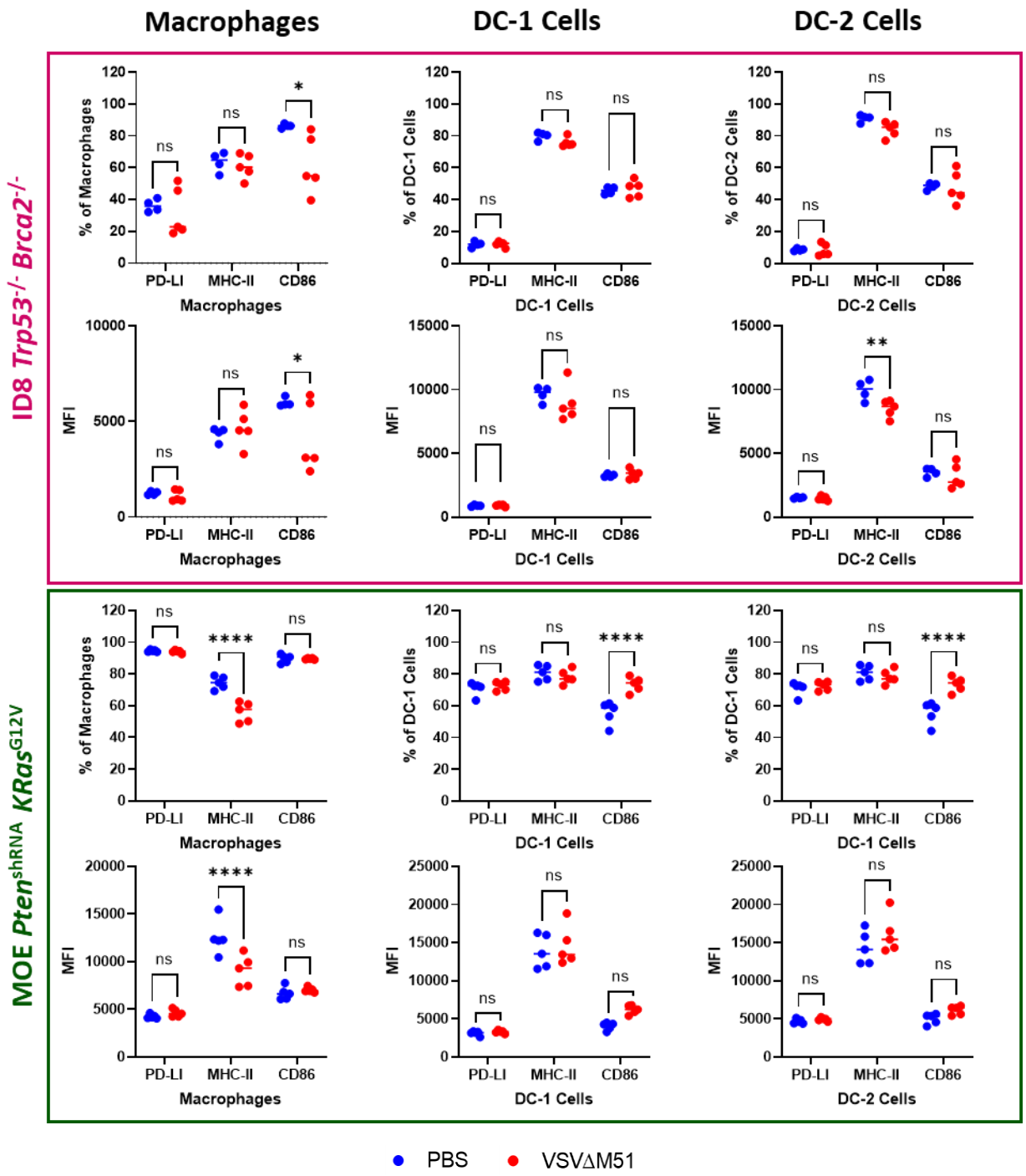

Figure 35: Activation markers of myeloid immune cells collected from spleens of tumour bearing mice treated with VSVΔM51. *Macrophages, DC-1 cells, and CD-2 cells were collected from the peritoneal wash of ID8 Trp53$^{-/-}$ Brca2$^{-/-}$ and MOE PTEN^{shRNA} KRas^{G12V} mice, previously treated with PBS control or VSVΔM51. Flow cytometry analysis of activation markers CD25, LAG3 and PD-1 was performed. *p<0.05, ****p<0.0001.*

5.4 Grey "Highlight" Fur Phenotype in ID8 Trp53$^{-/-}$ Brca2$^{-/-}$ Tumour Bearing Mice

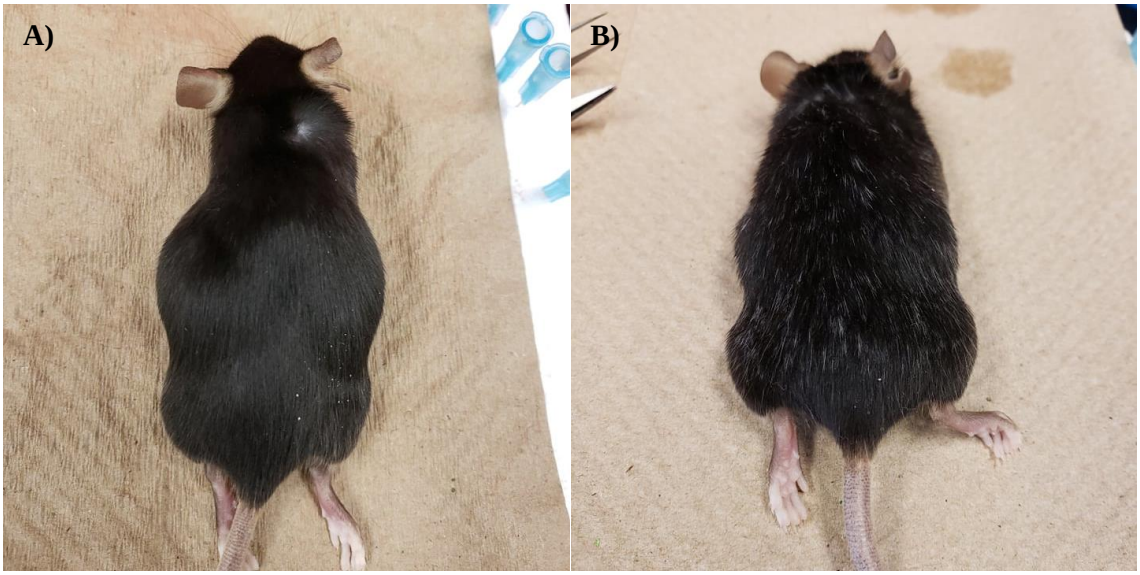

Figure 36: Grey highlight phenotype in ID8 Trp53$^{-/-}$ Brca2$^{-/-}$ tumour bearing mice. *A) Unaffected C57BL/6 tumour hosts showed normal and uniform fur colour throughout duration of study. B) An unusual change in fur colour was noticed in ID8 Trp53$^{-/-}$ Brca2$^{-/-}$ tumour bearing mice, some treated with PBS and some with VSVΔ51. This phenotype only affected mice within the same cage, and was not present in all mice within the same treatment group.*